Development of carbon nanotube-reinforced nickel matrix composites: processing, microstructure and physical properties

Dissertation

zur Erlangung des Grades

des Doktors der Ingenieurwissenschaften

der Naturwissenschaftlich-Technischen Fakultät III

Chemie, Pharmazie, Bio- und Werkstoffwissenschaften

der Universität des Saarlandes.

von

SEBASTIÁN SUÁREZ VALLEJO

Saarbrücken

2014

Tag des Kolloquiums: 14.05.2014

Dekan: Prof. Dr. Volkhard Helms

Berichterstatter: Prof. Dr. Frank Mücklich

Jun.-Prof. Dr. Volker Presser

Vorsitz: Prof. Dr. Guido Kickelbick

Akad. Mitarbeiter: Dr. Frank Aubertin

"These nanotubes are so beautiful that they must be useful for something. . ."

Richard E. Smalley

Contents

Abstract

The present thesis is focused on the design of a processing route which would deliver a microstructurally tailored metal matrix composite. By controlling the final microstructure, the resulting physical properties can be predicted and therefore optimized for a certain application. Process parameters were optimized considering the CNT defect state after dispersion. Additionally, the microstructural evolution is analysed during sintering, considering the potential chemical interactions. It was observed that the CNTs act as microstructural controller due to boundary pinning, resulting in finer final microstructures for higher CNT concentrations up to 3.0 wt.% CNTs, concentration beyond which no further refinement is detected. This stagnation is a consequence of the CNT agglomeration due to the mass transport during sintering. The mechanical, thermomechanical, tribological and electrical characterization of the composites was performed with complementary techniques. The improvement of the mechanical properties is associated to a Hall-Petch effect. Thermomechanical behaviour shows a decrease in the coefficient of thermal expansion. The anchoring effect of the CNTs is the responsible for this reduction and three model mechanisms for the behaviour are proposed. Tribological behaviour showed reduced friction and wear loss in the composites. Finally, the influence of the CNT concentration and distribution are correlated to the improvement in the electrical conductivity.

Zusammenfassung

Die vorliegende Arbeit beschäftigt sich mit der Entwicklung einer Herstellungsroute, welche die Synthese mikrostrukturell maßgeschneiderter Metallmatrixkomposite erlaubt. Dies ermöglicht eine Vorhersage und Optimierung der sich einstellenden physikalischen Eigenschaften für bestimmte Anwendungsfälle. So wurden die Prozessparameter hinsichtlich des Defektzustandes von CNTs optimiert und die während des Sintervorganges potentiell möglichen chemischen Wechselwirkungen analysiert. CNTs fungieren durch Behinderung der Korngrenzbewegung als Steuerungselement für die Mikrostruktur. Mit steigender CNT-Konzentration (bis zu 3 Gew.-%) nimmt die Korngröße ab. Höhere CNT-Konzentrationen führen zu Agglomerationen aufgrund des Massentransportes während des Sintervorganges und tragen nicht mehr zum Kornfeinungseffekt bei. Eine mechanische, thermomechanische, tribologische und elektrische Charakterisierung der Komposite wurde mit komplementären Methoden durchgeführt. Die Verbesserung der mechanischen Eigenschaften kann mit dem Hall-Petch Effekt korreliert werden. Gleichzeitig wird eine Abnahme des Wärmeausdehnungskoeffizienten festgestellt, welche mit dem Verankerungseffekt der CNTs zusammenhängt und durch drei Modellansätze beschrieben wird. Die tribologischen Untersuchungen zeigen eine Verringerung des Reibkoeffizienten und des Verschleißes. Abschließend wird eine Verbesserung der elektrischen Leitfähigkeit auf den Einfluss von CNT-Konzentration und -Verteilung zurückgeführt.

Acknowledgements

Every large endeavour is always composed of the work and influence of several people and institutions. With these paragraphs I want to acknowledge the help and support from those that directly or indirectly participated in the work.

First of all, I would like to specially thank Prof. Frank Mücklich for giving me the opportunity to develop myself in a strongly cooperative and scientific atmosphere at his institute. Moreover, I am very grateful to him for the chance to investigate in a very interesting topic and his support throughout my whole time at the institute.

I would also like to thank my second reviewer Prof. Volker Presser for accepting the revision of this work and his insightful comments and suggestions. Particularly, I would like to thank his group for the fruitful discussions that we shared in the last year.

Many thanks go to the German Academic Exchange Service (DAAD) for financially supporting the research work for the first three and a half years.

A special mention goes to those colleagues that somehow collaborated and discussed the experiments and results, helping me to achieve the outcomes that are presented in this thesis. These colleagues were: Prof. Carlos González Oliver (CNEA/Argentina), Dr. Diego Acevedo (UNRC/Argentina) and Dr. José García (Sandvik Coromant/Sweden). Within the institute, I gratefully acknowledge the help from Dr. Carsten Gachot, Dr. Peter Leibenguth, Andreas Rosenkranz, Leander Reinert and Björn Lechthaler. In the *AG Advanced Composites and Structures*, I wholeheartedly thank Dr. Flavio Soldera and Federico Miguel for their friendship and support.

The *room 2.11 society;* Federico Lasserre, Nicolas Souza, Dr. Orlando Prat and Dr. Esteban Ramos-Moore, who influenced my work and personality (in a good way!) and were the inspiration for most of the progress in this work.

Last but not least, I would like to thank my parents, brother and of course my wife Agustina, whose unconditional support and love throughout this entire process has helped me immeasurably. None of this would have been possible without them.

S. Suárez

Saarbrücken, January 2014

I. Introduction and objectives

I.1. Introduction

Reliability and property tailoring of new materials in high performance and heavy duty tasks are constant goals to achieve in materials engineering. In the past years, composite materials have been introduced in diverse applications such as aerospace, ground transportation, electronics and home goods. Among the different advantages, the exploitation of the matrix-reinforcement synergy is most notable. However, reinforcements can additionally bring along adverse effects depending on the application. Particularly in electrical contacts, duty life is established by resistance to strong degradation mechanisms such as inter-welding between electrodes and arcing erosion.

This was first achieved by the use of Ag-based composites reinforced with metal oxide particles (CdO). In this case, the function of the reinforcement is to avoid electrode inter-welding and to absorb the energy input by sublimating.

Several years ago, the European Commission restricted the utilisation of Cd in component manufacturing, due to its hazardous nature for human health. The search for a suitable replacement began, directing all efforts to find another metal oxide that would act similarly. The first generation of replacements was based mainly on the reinforcement of Ag matrices with SnO_2 particles. The results were promising with regard to weldability and arc duration, yet the performance of the composites was compromised. It was observed that after a single break operation (circuit interruption under load), the oxide particles formed non-conductive (semiconductive, at best) layers in the immediate subsurface. These layers are strong barriers for the electrical current flow, generating significant energy losses and increasing the overall electrical resistance of the component. Moreover, the oxides have been hypothesised to release oxygen during arcing, which would increase the amount of porosity in the material.

Metal matrix composites are widely used in different applications. Due to their electric and magnetic properties, Ni composites are used in commercial rechargeable battery electrodes [1,2], reactor electromagnets [3] and as a constituent in electrical contact materials [4], among others. The latter usually contain either high amounts of costly noble metals or ceramic elements that are intrinsically electrically insulating or at best, semiconductive, thereby reducing the global thermal and electrical conductance. We propose an alternative that

circumvents both drawbacks by using conductive, high performance reinforcements: multiwall carbon nanotubes (MWCNT). Since their discovery [5–7], carbon nanotubes (CNTs) have shown outstanding physical properties and are the benchmark for thermally conductive materials to date [8,9], presenting tailored semiconductor behaviour [10] as well. Multiwall carbon nanotubes (MWCNT) have the particularity of always being metallic (zero band gap conductors) due to the fact that they possess at least one metallic layer [11].

I.2. Objective of this work

The main objective of this work is to develop a Ni-based composite which would serve as a Ag replacement in electrical contacts. For that, the use of carbon nanotubes (CNTs) as reinforcement is proposed on the basis that they possess outstanding mechanical, thermal and electrical properties. These properties would improve several features of the Ni, approaching the optimal properties required for electrical contact performance. Among the requirements, contact materials are expected to present:

- Good electrical conductivity: in order to reduce the energy loss from Joule heating.
- Good thermal conductivity: in order to rapidly and efficiently dissipate the energy input provided by the electric arc.
- Good mechanical properties: to avoid surface topography modification due to plastic deformation during closing operations. This would be detrimental to the arcing behaviour by reducing the effective contact area between electrodes.
- Good tribological resistance: due to heating, electrical contacts suffer from fretting wear on the surface as a result of the thermal expansion mismatch with other components.
- Thermal stability: for both, the reinforcement and the matrix microstructure due to large thermal stresses that components are usually subjected to.

Moreover, a Ni matrix is a stepping stone towards other well established applications e.g. solid oxide fuel cells (SOFC) anodes, improving upon the current Ni/YSZ (Yttria Stabilised Zirconia) composites. This requires low thermal expansion and good mechanical, electrical and thermal properties. High-tech applications such as electronic packaging materials or static electromagnetic shielding (commonly known as MuMetals) are also in reach.

I.3. Organization of the work

The present work was organised in the following items:

State of the art and theoretical background: the aim of this section is to introduce the reader to the concepts necessary to interpret further results and analyses made in the work. It contains a brief summary of the latest published work related to the topic of this study.

Materials and methods: In this section, the starting materials as well as the selected processing and manufacturing methods are introduced. Furthermore, the characterisation methods are briefly described.

Precursor processing and MWCNT degradation analysis: the structural stability and inter-reaction between the MWCNTs and Ni are analysed by several complementary techniques. The thermodynamic feasibility of the chemical reactions between the components was simulated so as to predict the interaction.

The role of MWCNT in the grain growth – Microstructural analysis: the influence of different partial amounts of MWCNTs in the grain growth and the final microstructure are studied. A correlation with two-phase material models is made so as to find the refinement mechanisms acting during grain growth.

Thermomechanical behaviour: bulk dilatometry and lattice behaviour: the thermal expansion behaviour of bulk composites processed by different routes is investigated. In order to understand the improvement in the thermomechanical properties, response and interaction modes are proposed.

Mechanical properties: grain boundary strengthening: in this chapter, the influence of the MWCNTs on the microstructure and thus on the mechanical properties is analysed and discussed.

Tribological properties: friction and wear behaviour: the improvements in the friction and wear behaviour in low-concentration (1.0 wt %) MWCNT-reinforced composites are scrutinised. A correlation between the response, the microstructure and its oxidation kinetics is presented.

Electrical properties: transport and coupling: the electrical resistivity of the composites is evaluated and discussed considering the partial amounts of MWCNTs in the sample. Theoretical modelling is performed to correlate and interpret the experimental results.

I.4. Dissemination of the work

The contents of this study were partially or fully published in peer-reviewed journals or presented in scientific conferences. The articles and contributions are listed below.

Peer-reviewed journals

S. Suárez, F. Soldera, C. González Oliver, D. Acevedo & F. Mücklich – Thermomechanical behaviour of bulk Ni/MWNT composites produced via powder metallurgy. Advanced Engineering Materials 14(7): 2012; 499-502.

S. Suárez, E. Ramos-Moore & F. Mücklich – A high temperature X-ray diffraction study of the influence of MWCNTs on the thermal expansion of MWCNT/Ni composites. Carbon 51(1): 2013; 404-409.

S. Suárez, F. Lasserre & F. Mücklich – Mechanical properties of MWNT/Ni bulk composites: Influence of the microstructural refinement on the hardness. Materials Science and Engineering A. 587: 2013; 381-386.

S. Suárez, A. Rosenkranz, C. Gachot & F. Mücklich – Enhanced tribological properties of MWCNT/Ni bulk composites – Influence of processing on friction and wear behaviour. Carbon 66: 2014; 164-171.

S. Suárez, E. Ramos-Moore, B. Lechthaler & F. Mücklich – Grain growth analysis of multiwalled carbon nanotube-reinforced bulk Ni composites. Carbon 70:2014;173-178.

S. Suárez, F. Lasserre, O. Prat & F. Mücklich – Processing and interfacial reaction evaluation in MWNT/Ni bulk composites. Physica Status Solidi A. 2014. *Accepted*.

S. Suárez, N. Souza, F. Lasserre & F. Mücklich – Influence of the reinforcement distribution on the electronic transport properties of MWNT/Ni bulk composites. Carbon. 2014 *Submitted*.

Conferences

S. Suárez, F. Soldera, J. García & F. Mücklich – Comparative electrical studies of Ni/MWNT bulk composites. International conference on the science and application of nanotubes NT11. University of Cambridge, Cambridge (UK). 10-16 July 2011.

S. Suárez, F. Lasserre, F. Soldera, C. Gonzalez Oliver & F. Mücklich – Thermomechanical behaviour of Ni/MWNT composites produced via powder metallurgy. International meeting on the chemistry of nanotubes and graphene ChemOnTubes 2012. Arcachon (FR). 1-5 April 2012.

F. Lasserre, F. Soldera, S. Suárez & F. Mücklich – Mechanical properties of Ni/MWNTAu composites. International meeting on the chemistry of nanotubes and graphene ChemOnTubes 2012. Arcachon (FR). 1-5 April 2012.

S. Suárez, F. Lasserre & F. Mücklich – Microstructural refinement and mechanical properties improvement in MWNT/Ni bulk composites. European congress and exhibition on advanced materials and processes EUROMAT 2013. Sevilla (ES). 8-13 September 2013.

II. Theoretical background and state of the art

II.1. Metal Matrix Composite (MMC) materials

A composite material is defined as a combination of two or more materials, which differ from each other in form and/or composition. The constituents must retain their identities; that is, they do not dissolve or merge completely into one another although they act synergistically. Normally, the components can be physically identified and exhibit an interface. Composite materials are created to obtain properties that cannot be achieved by any of the components acting alone [12]. This result is frequently referred to as the composite effect.

The matrix is the major constituent and is essentially, the material in which the reinforcing phase is embedded, providing ductility and formability to the composite. Matrix materials can include: aluminium (the most widespread), titanium, magnesium, copper, nickel, and ordered intermetallic compounds (NiAl and Ti_3Al) among other materials [12]. The reinforcement is basically the load-bearing phase which may constitute from 10 to 60 vol.% of the composite. They are classified according to type and distribution, the most common being: continuous fibres, whiskers/short fibres, particulate and laminate reinforcements (Figure II-1).

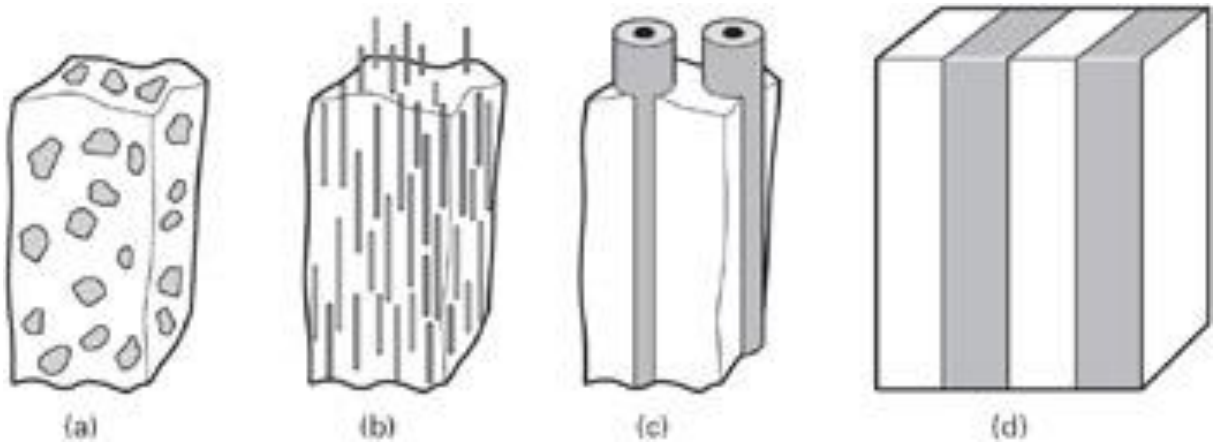

Figure II-1 - Different reinforcement types for composites: (a) particle reinforcement; (b) short fibre reinforcement; (c) continuous fibre reinforcement; (d) laminate reinforcement [13].

Continuous fibre or filament reinforcements traditionally include graphite, silicon carbide, alumina, and refractory metals [12,14]. Short fibres, either organised or randomly distributed, are usually silicon carbide, alumina, and more recently carbon nanotubes and graphene [12].

In the late years, major improvements have been achieved in the field of composites regarding the systematisation and reproducibility in the manufacturing as well as a reduction in the production costs by efficiently modifying the processes to fit them to industrial scales. These improvements have opened a wide span of applications for composites in several different fields such as: aerospace, automotive, domestic appliances and sporting goods among others. For example, in recent years, the aerospace industry has focused its efforts in reducing the total weight of aircrafts in order to reduce fuel consumption and gas emissions. The adopted solution was the use of high amounts of light metal composites such as Al and Ti matrices. Figure II-2 shows the partial amounts of materials in a commercial aircraft.

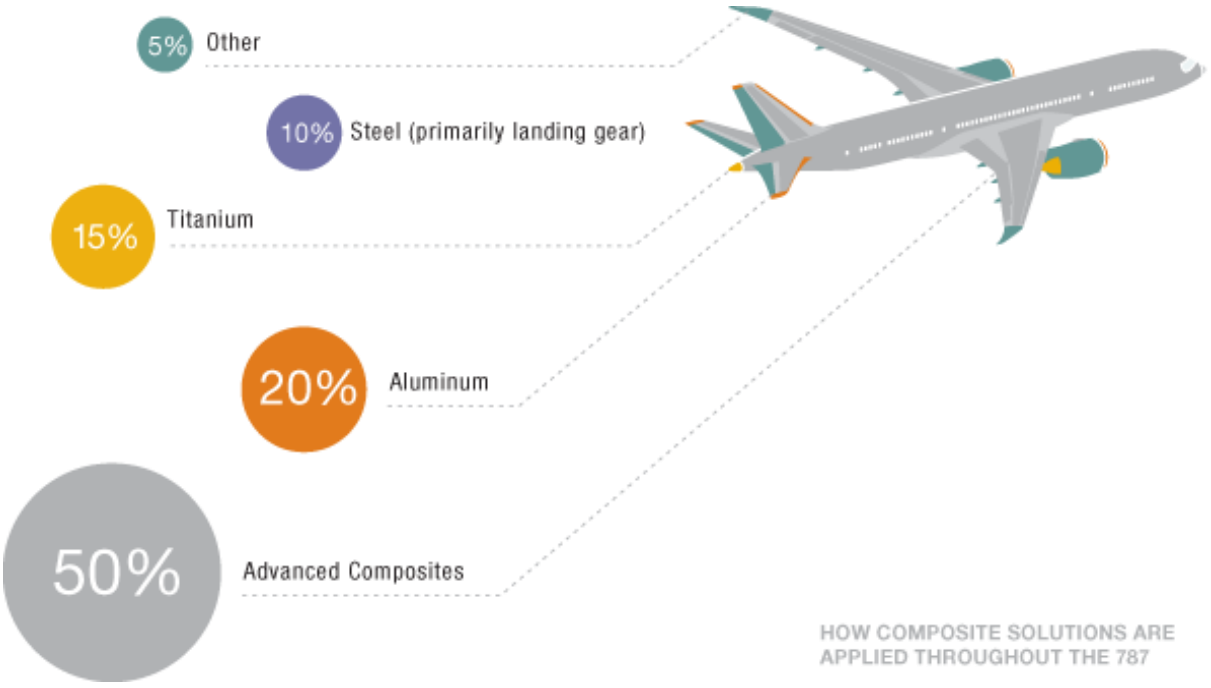

Figure II-2 - Materials usage in weight percent for a commercial aircraft (credit: Boeing.com [15]*)*

Moreover, the introduction of MMCs for the airframe of commercial aircrafts is expected to reduce maintenance due to risk reduction in component corrosion and fatigue.

Another example of application is in low-voltage electrical contact materials. The main problem affecting the duty life of a contact material is the erosion produced by the sparking during circuit breaking. This is a result of contact welding, which generates a metallic bridge during the break operation. To overcome this obstacle, a first generation of Ag-based composite

contacts was developed. These composites were reinforced with metal oxide particles (mainly CdO) so as to reduce the weldability of the contacts. The CdO would evaporate during arcing diminishing the arc duration. After some years in use, the European Commission determined that certain hazardous metals were to be replaced in industrial applications, one of which is Cd. Industrial developers took on the replacement of CdO by other ceramic particles presenting lower health risks. SnO_2, WO_3 and In_2O_3 were proposed, among others, the main drawback of which is a strong oxide platelet formation after arcing. This significantly increases the electrical resistance of the composite, therefore increasing Joule energy losses [16,17].

II.2. Processing of MMC

II.2.1. Liquid-state processing (LSP)

LSP methods are mainly focused on low-melting point metals such as aluminium or magnesium. Because this process involves the melting of the matrix material, one must overcome the cumbersome obstacle of energy management. Moreover, the processing atmosphere is critical due to the increased chemical reactivity of the molten metal (enhanced oxidation and reaction with the reinforcement). The main advantage of this processing method, however, is the improvement of the interfacial contact compared to solid-state processing routes (section II.2.2).

Casting

Casting consists in manufacturing bulk components from molten metal. These are poured into moulds, solidified and ejected from the mould or the container is broken. It is a very useful technique when the required components present a complex shape. The main drawback is the non-uniformly distributed reinforcement, which can lead to undesired effects on the physical properties.

Liquid metal infiltration

This case is similar to the previous method. However, the main difference is the application of an external pressure so as to inject the molten metal into the mould. The same drawbacks as described before are observed in this technique such as: fibre reagglomeration, directionality in the fibre distribution, etc.

Spray deposition

The spray deposition method is mainly used in composite coatings. The process consists in spraying a molten mixture onto a surface that is to be protected. By regulating the temperature and rheological parameters, it is possible to tailor the roughness and compactness of the coating. It is usually utilised with low-melting point metals, to reduce the energy input.

II.2.2. Solid-state processing (SSP) - Powder metallurgy methods

Powder metallurgy routes basically densify a porous body applying temperature (and eventually pressure) to achieve a desired final density. These packed metallic powders bond together (mainly by diffusion) when heated over temperatures approximately half of their melting point. This phenomenon is called *Sintering*. The main advantages of this processing route in comparison to liquid state processes are: lower processing temperatures, better control of the reinforcement distribution within the matrix, better microstructural control. The tailoring of the microstructure is referred to the final grain size, final density and reinforcement distribution and interface with the reinforcements. Solid state sintering is divided into three main stages, namely: initial, intermediate and final (see Figure II-3). The initial stage is characterised by the formation of so-called "sintering necks", which form a material path for the different material transport mechanisms that will act during sintering. The second stage is where the most significant densification is achieved, and isolating the interconnected porosity and reaching final relative densities up to 93%. The last stage involves the densification from an isolated porosity state to the final densification.

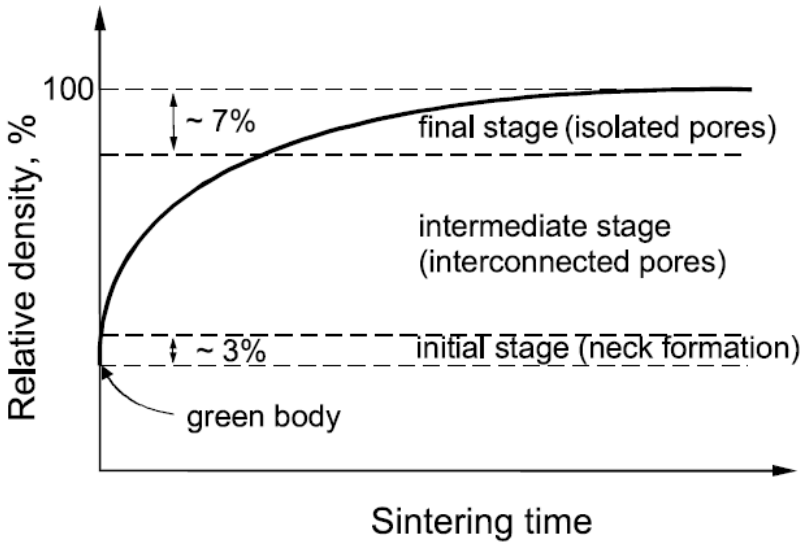

Figure II-3 - Densification curve of a powder compact, identifying the three sintering stages [18].

The driving force of sintering is the reduction of the total interfacial energy [18]. In a powder compact, the total interfacial energy can be expressed as follows:

$$\Delta(\gamma.A) = \Delta\gamma.A + \gamma.\Delta A \qquad \textit{(Equation II.1)}$$

where γ is the specific interfacial energy and A the total interfacial area of the compact. The change in interfacial energy (Δγ) is related to the replacement of solid/vapour interfaces by solid/solid interfaces; whereas the change in interfacial area (ΔA) is due to grain coarsening. These aspects are schematically represented in Figure II-4.

As mentioned before, the sintering variables or parameters play a fundamental role in the process. They are usually divided into two main categories: material-related and process-related variables. The former includes the powder size, shape, size distribution and chemistry, whereas the latter includes all the variables inherent to the sintering process such as: temperature, time, pressure, atmosphere, heating and cooling rates among others. In accordance with these parameters, the sintering processes can be divided into pressureless and pressure-assisted sintering. The following briefly describes the most widespread techniques.

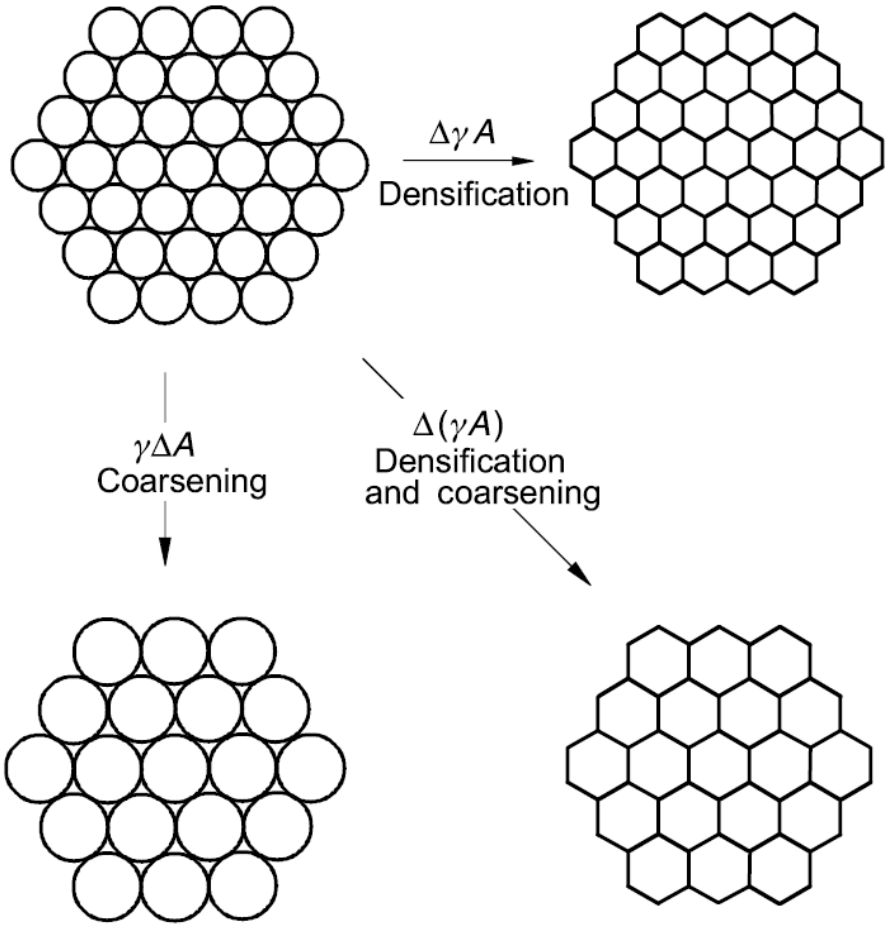

Figure II-4 - Basic phenomena occurring during sintering [18].

Cold pressing plus sintering (CPS)

Also known as "pressureless sintering", CPS is the most straightforward sintering technique. It consists of a pre-consolidation of a powder mixture into a porous body and its subsequent densification by the application of temperature without external pressure. Usually, the main densification mechanisms consist of lattice and grain boundary diffusion of the metals or ceramics [18].

Hot uniaxial pressing (HUP)

Another possibility in sintering is the application of an external pressure on the sample during the heating slope and the isothermal treatment. Since the densification driving force is directly influenced by the application of this external pressure, the densification kinetics are modified. However, this external force would not affect the grain growth, since this is only affected by the temperature of the sample. Because the densification rate is increased by the application of external pressure, the temperature and time of sintering can be reduced, obtaining full density samples in shorter times. Also, the external pressure will help to close porosity during the final stage of sintering.

Hot isostatic pressing (HIP)

HIP is used for the densification of porous compacts, as well as in the correction of sintering flaws present in the aforementioned methods. The process consists in the encapsulation of the porous compact within a container and the application of heat and isostatic pressure in an inert gas medium with pressures of about 300 MPa. In this case, a two-stage sintering is usually applied: low-pressure for porosity isolation followed by high-pressure densification [18,19]. It has been demonstrated that before the second stage, all the porosity must be isolated (no porosity interconnectivity) in order to achieve high final densities. This is due to the increased probability of a pore/boundary separation [18].

Spark plasma sintering (SPS)

Spark plasma sintering is a newly developed technique which consists in the rapid powder sintering applying pressure and heat produced by a short electric pulse. It achieves very good final densities with minimal grain growth in very short times. The enhanced sinterability is mainly linked to a particle surface activation and increased diffusion rates on the contact zones caused by the applied current pulse [20]. It is mainly used for the consolidation and sintering of metals and ceramics, although polymer consolidation has been reported [21].

II.3. Carbon Nanotubes (CNTs)

Carbon nanotubes have had a deep impact in the scientific community since their first identification by Iijima in 1991 [5]. From that point on, the amount of research has increased exponentially covering very diverse topics such as: development of fundamental knowledge on CNTs, theoretical and empirical studies on the physical properties of CNTs, and potential applications in very dissimilar fields such as micro and nano-electronics, structural composites, multifunctional composites, energy transfer and storage etc. Figure II-5 depicts the increment in the amount of published papers dealing with CNTs.

Despite the huge amount of research reported in scientific publications and conferences, the CNTs show such a high versatility that still enable a growing research community to further develop innovations in this field.

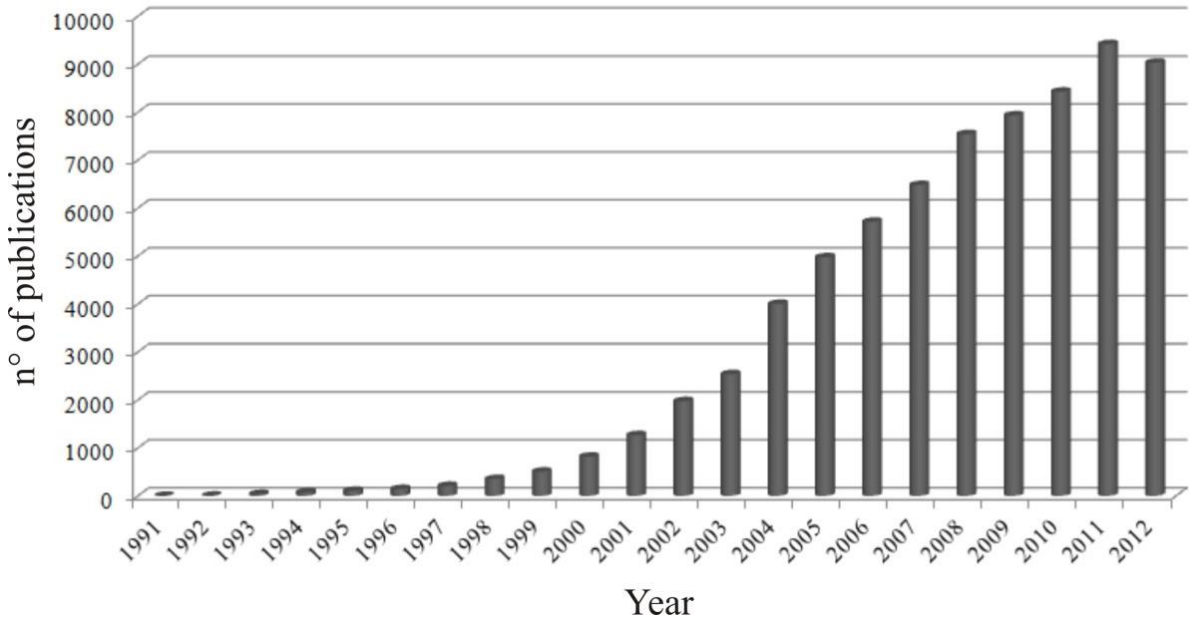

Figure II-5 - Amount of publications per year dealing with CNTs (source: Scopus)

II.3.1. Carbon hybridisation

Covalent sp^3 and sp^2 bonding of carbon [22]

Carbon is a versatile element which can show different types of hybridisation. The ground state phase of carbon under ambient conditions is the sp^2 graphite, whereas at higher temperatures and pressures, sp^3 cubic diamond is stable [23]. The sp^3 hybridisation presents a C-C bond energy of 370 KJ/mol, while sp^2 has a C=C bonding energy of 680 KJ/mol. Moreover, the bond

length is 15% shorter in sp^2. This translates into better mechanical strength in the basal plane direction for sp^2 bonded carbons.

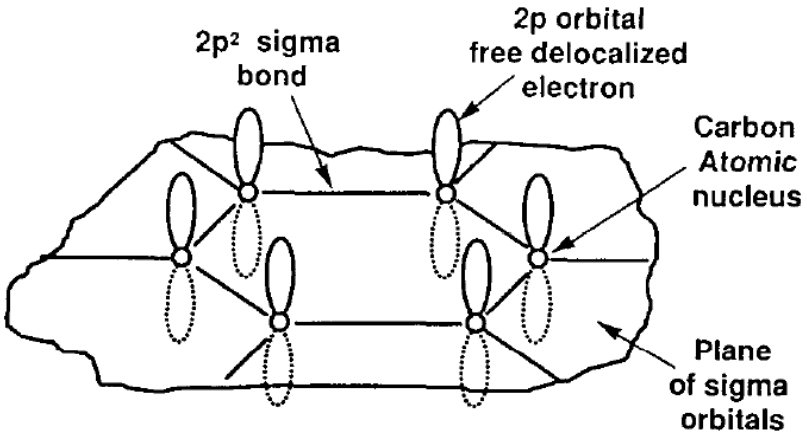

Figure II-6 - Electron distribution in sp^2-hybridised carbon atoms [22].

In graphene, each sp^2 carbon atom is combined with three other sp^2 carbon atoms, resulting in a series of hexagonal lattices resembling a honeycomb shape (Figure II-6). The fourth delocalised electron is located in an orbital perpendicular to this basal plane and forms π-bonds. Unlike the sigma bonds, they are weak due to significantly lower orbital overlapping between the component p-orbitals due to their parallel orientation. These electrons are the main responsible for the electronic and thermal conduction in graphitic structures.

II.3.2. Definition of carbon nanotubes

In a general manner, carbon nanotubes can be defined as hollow cylinders of sp^2 carbon sheets with a thickness of one atom. They can be studied as single molecules due to their small size (nanometric diameter and micrometric length), or even as quasi one-dimensional crystals with translational periodicity along the tube axis [24]. Since there are infinite ways of rolling this mono-atomic carbon sheet, a set of defining parameters must be utilised to characterise them. For that, we must base the definition on the chemical stereoisomerism [25], which provides a set of parameters under the term chirality. The atomic structure of a CNT is thus described by the chiral vector C_h and the chiral angle θ (Figure II-7), represented with the following equations:

$$\vec{C}_h = n\vec{a}_1 + m\vec{a}_2 \qquad \textit{(Equation II.2)}$$

$$\tan\theta = \frac{\sqrt{3}m}{2n+m} \qquad \textit{(Equation II.3)}$$

Where n and m are integers and a_1 and a_2 are the unit vectors of the carbon lattice. Moreover, the diameter of a CNT can be determined from the previously described parameters by using the following equation:

$$d = \frac{a\sqrt{m^2+n^2+nm}}{\pi} \quad \textit{(Equation II.4)}$$

According to their chiral index, they are classified in three different types, namely: armchair ($n = m$), zig-zag ($n = 0$) and chiral ($n \neq m$).

They can also be classified by the number of walls stacked on a tube. Nanotubes exist either as singlewall carbon nanotubes (SWCNT) or multiwall carbon nanotubes (MWCNT).

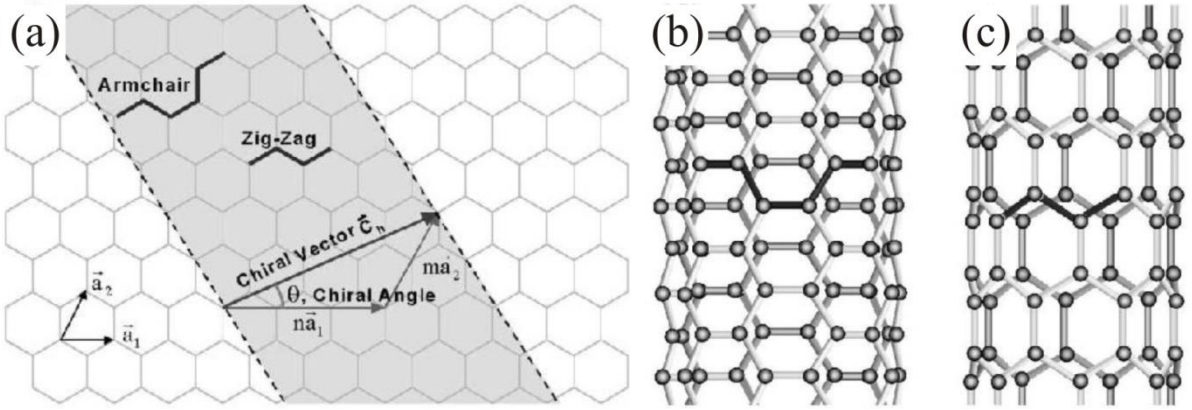

Figure II-7 - (a) Schematic representation of an infinite graphene sheet, describing the rolling possibilities and their subsequent chiral identification. (b) Armchair configuration. (c) Zig-zag configuration [26].

MWCNTs were first identified by Iijima [5] and consist of a set of concentrically nested SWCNTs, separated by a distance analogue to that of consecutive graphene layers in graphite (3.35 Å) [27]. They can reach lengths similar to those of SWCNT and outer diameters ranging from 5 to 100 nm corresponding to approximately 30 walls. Due to the large curvature of the outer wall, confinement effects are significantly lower than in SWCNTs, making some properties quite close to those of graphite [24].

II.3.3. Physical properties of carbon nanotubes

Electrical and electronic properties

SWCNTs are extraordinary since they can be either metallic or semiconducting in accordance with the following rules: $n = m$ tubes behave like metals; (n, m) tubes with $n-m = 3j$, where j is a nonzero integer, are very small-gap semiconductors; and all SWCNTs with $n-m = 3j\pm1$ are large-gap (~1.0 eV for tube diameters of approx. 0.7 nm) semiconductors. Strictly, the $n -$

$m = 3j$ tubes would theoretically be all metallic, but because of tube curvature effects, a tiny band gap opens up when $j \neq 0$ (Figure II-8). Thus, carbon nanotubes can be large, small, or zero-gap systems. The armchair tubes are always metallic within the single-electron representation due to their symmetry, independent of their curvature (Figure II-8).

As the tube diameter (d_t) increases, large and small band gap types decrease with a $1/d_t$ and $1/d^2_t$ dependency, respectively. Thus, for most experimentally observed carbon nanotubes, the small-gap would be so narrow that it is practically assumed that all the $n - m = 3j$ tubes can be considered metallic at room temperature because their thermal energy is sufficient to excite electrons from the valence to the conduction band [28]. Considering that the CNTs possess 2 conduction channels, the resistance of a ballistic nanotube is expected to be 6.45 kΩ [29]. The electron (transport) interactions are believed to be governed by the Tomonaga-Luttinger-liquid model [30–32].

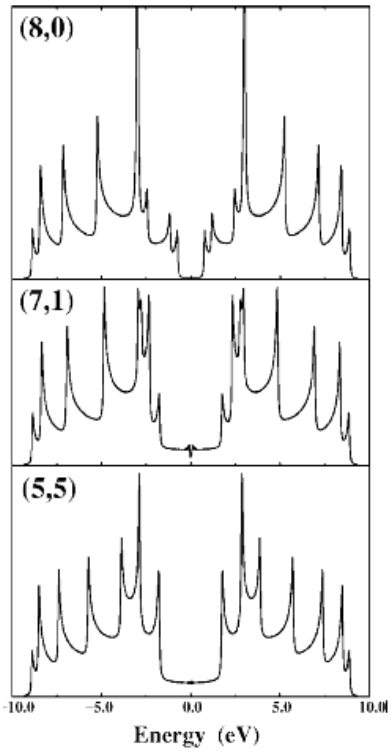

Figure II-8 - Electronic density of states for a zig-zag (8,0), chiral (7,1) and armchair (5,5) carbon nanotubes [28].

Because of statistical probability and restrictions on the relative diameters of the individual tubes, one of the shells, and thus the whole MWCNT, behaves as a zero-gap metal. Moreover, MWCNTs have also been theoretically predicted to show quantised conductance [33,34]. Experimentally, the quantum conductance of CNTs was demonstrated with a very creative test

[35]. The researchers attached arc-grown MWCNTs to a gold electrode and gradually lowered the probe towards a Hg-filled Cu crucible, consequently closing a highly sensitive electrical circuit. Interestingly, they found that after the first MWCNT contacted the Hg droplet and by continuing the movement towards the centre of the contact, the conductivity did not change until a second nanotube contacted the Hg droplet. By observing the conductance versus depth graphic (Figure II-9), the quantised steps of the electrical behaviour are clearly noticed. Each step is an integer multiple of the fundamental quantum conductance.

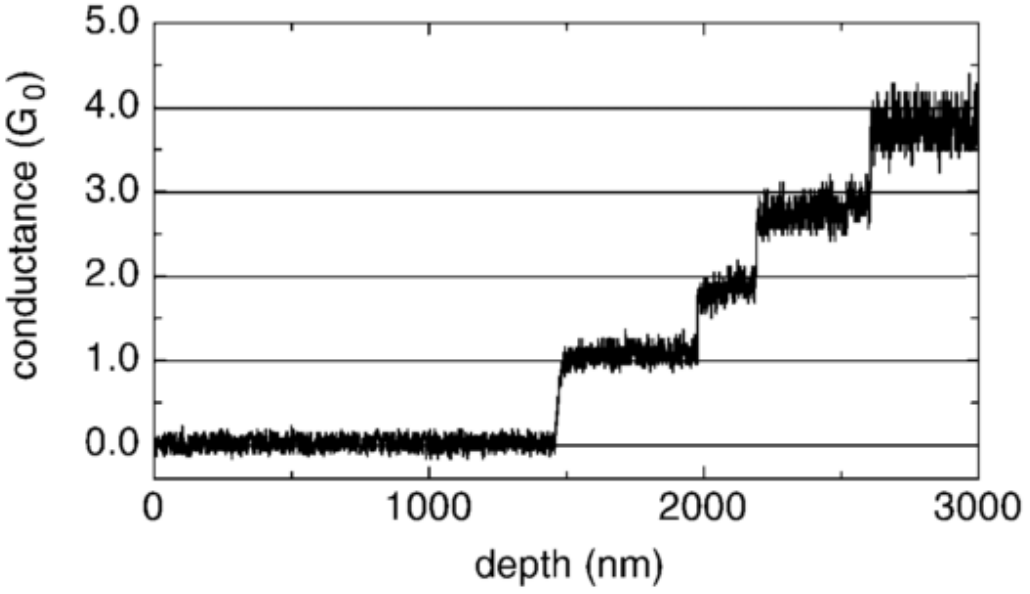

Figure II-9 - Conductance change of a CNT-bundle submerged into an Hg droplet. The quantum nature of the electrical conductance in CNTs is depicted by the step-like increment [35].

This experimental demonstration, coupled with the outstanding current carrying capacity of CNTs (approximately 10^9 A/cm^2) [36], opens a great amount of possibilities for the utilisation of CNTs in electricity management applications. From this result, realistic calculations and modelling can be carried out in order to study the feasibility of the manufacturing of CNT-containing components. Additionally, for a proper design of components which consist of several CNTs, it is important to consider all the possible interactions between CNTs and matrices or even the inter-tube interactions. For example, in CNT-based electronic devices, the formation and control of a Schottky barrier is very important [37]. A Schottky barrier is formed by joining a conductive (e.g. metal) with a semi-conductive material (e.g. chiral CNT). In the metal-semiconductor junction a potential barrier is formed showing rectifying capabilities. It has been theoretically proven, that a potential barrier is formed by connecting a ring of Pt atoms to a (8,0) SWCNT [37]. The calculations showed that the Schottky barrier had a p-type nature

with an energy gap of approximately 0.4 eV. However, the barrier has only a width of a few nanometres, which can be tunnelled by electrons [38]. Regarding the inter-tube interactions, there is yet to be a unified definition of what happens between two crossed CNTs. A summary of the probable interactions will be thoroughly discussed in chapter IX.

Mechanical properties of CNTs

Due to their sp^2 hybridisation, the CNTs possess outstanding mechanical properties. Particularly, when related to their density, the CNT rank among the best reinforcing phases available in the market (Figure II-10).

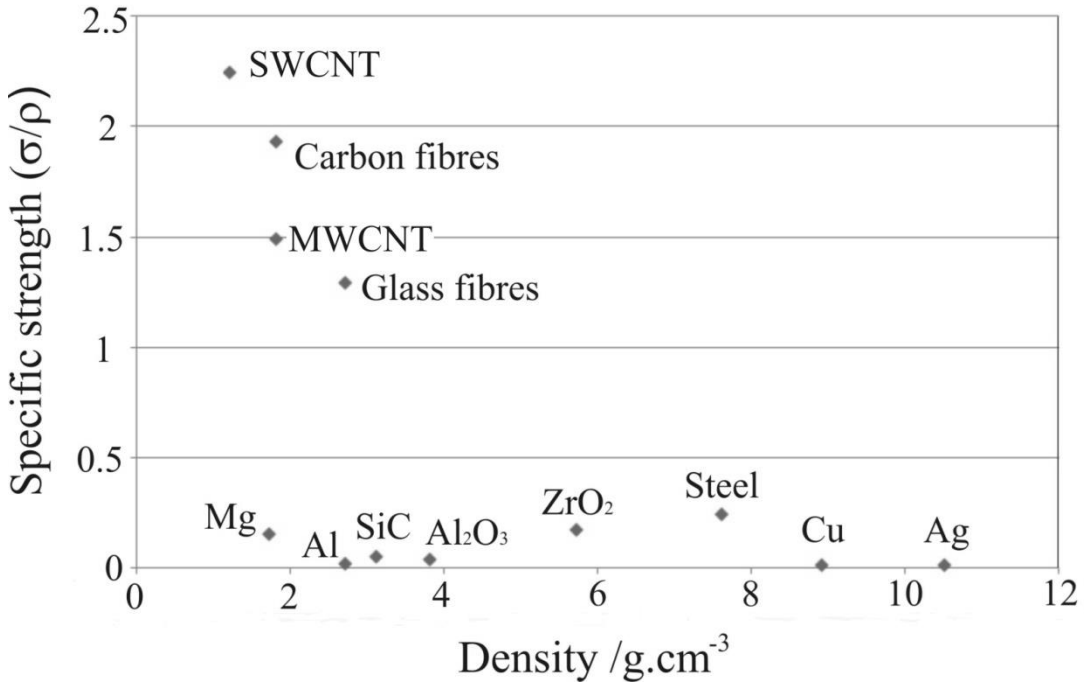

Figure II-10 -Plot of specific strength (divided by the density) versus density for several reinforcing and structural materials.

The exceptional in-axis mechanical properties are due to the strong sigma bonding between carbon atoms, which is the strongest chemical bond known in nature [39]. The Young modulus ranges from a few GPa up to 600 GPa for the strongest materials such as diamond and SiC. It has been reported that the Young modulus of CNTs can reach values in the TPa range [40–42], largely surpassing previously known materials. The tensile strength is another property that has been demonstrated to be noteworthy in these materials. Particularly, it reaches values ranging from 20-30 GPa (for SWCNTs [43,44]) to 150 GPa for MWCNTs [42]. Another distinctiveness of CNTs is their high resilience. It has been observed that when a load is axially applied to a CNT, it bends without breaking significantly changing their shape developing a rippled

structure. When this load is released, the CNTs are restored to their original shape without atomic rearrangement [23].

Thermal properties of CNTs

Prior to the discovery of CNTs, carbon-based materials were already known to be the best thermal conductors available (Table II-1). For example, diamond and in-plane graphite displayed the highest thermal conductivity of any known material. The first approaches to determine the axial thermal conductivity of CNTs were made by computer simulations for both, single and multiwall carbon nanotubes. Berber et al. [9] predicted an extremely high conductivity for SWCNT, largely surpassing that of diamond. Their calculations were based on the assumption of a defect-free state of the CNT, resulting in approximately 6600 W/m.K for a (10,10) armchair tube. In the case of MWCNTs [8], the thermal properties were measured experimentally, and found a linear dependence with the temperature and values as high as 3000 W/m.K. As bundles, simulations for (10,10) SWCNT presented a very strong anisotropy, resulting in an axial conductivity of 950 W/m.K and 5.6 W/m.K transversally [45]. Experimentally, the measured thermal conductivities present a wide range of values. Hone and co-workers determined conductivities at room temperature between 1750-5800 W/m.K for SWCNT samples. Moreover, they determined the phonon mean free path to be 0.5-1.5 μm [8,46]. The most relevant conclusion of their work is that they could show that the thermal resistance is mainly due to boundary scattering within the CNT [46].

Table II-1 - Thermal conductivity of known materials in comparison to carbon nanotubes (adapted from [22])

Material	Thermal conductivity @25°C [W/m.K]
Pyrolytic graphite (ab direction)	390
Pyrolytic graphite (c direction)	2
Graphite fibre	1180
Diamond	2000-2100
Silver	420
Copper	385
Beryllium oxide	260
Aluminium nitride	200
Alumina	25
MWCNT (experimental)	3000
SWCNT (theoretical)	6600

In both SWCNT and MWCNT, the heat transport is predominantly made by phonons. Ballistic thermal conduction has been predicted for SWCNT at low temperatures, whereas for MWCNT,

due to interlayer interactions resulting in complex transport phenomena, the heat conduction mechanism cannot be analyzed as one-dimensional [6].

Aliev found that the thermal conduction is limited by two main factors, namely: inhomogeneities in the sheet structure and the intrinsic defects of the individual nanotubes that generate a phonon boundary scattering [47]. Due to their morphology, CNTs show a strong anisotropy as is the case with their electrical properties. The transversal thermal conductivity showed a 25 fold difference in the parallel and perpendicular conduction in MWCNT sheets [47].

II.3.4. Processing of carbon nanotubes

Functionalisation

Functionalisation refers to the modification of the tube surface in order to tailor it to your needs, such as: stable dispersion, proper integration to a matrix, etc. Functionalisation can be either covalent (dissociation of a C=C bond into a C-C bond and the further attachment of a molecule, monomer or functional group), or non-covalent (preservation of the structural integrity of the tube by coating it with surfactants or polymers). The main drawback of the first is the structural modification of the tube's surface, resulting in a detriment to its intrinsic physical properties (e.g. electrical and thermal properties). It is usually used for the improvement of already low conductive matrices such as polymers and ceramics, where the matrix properties still have much to gain from a proper integration. Regarding the non-covalent functionalisation, despite the fact that it retains the structure of the tube and subsequently its properties, it sometimes generates an undesired interface that may interfere in the transfer of thermal and electrical load.

Dispersion

Due to their great specific surface and high surface energy, CNTs tend to form agglomerates generated by van der Waals interactions. Commercially available CNTs (both SWCNT and MWCNT) are usually delivered as aggregates in powders, rendering their dispersion essential for a proper use. Moreover, because of the tube-tube interactions, CNT agglomerates show reduced physical properties compared to those in dispersed state [24].

In order to profit from the outstanding physical properties of CNTs, several strategies for the dispersion of agglomerates have been studied. The most widespread is the ultrasound-assisted colloidal dispersion in several different media. The dispersion media may include: surfactants,

solvents and/or macromolecules. This approach, however, becomes non trivial due to the hydrophobic nature of the carbon nanotubes.

The idea behind this method is to use the strong mechanical interaction with ultrasound waves and the steric effect of certain compounds (i.e. surfactants) to achieve a stable colloidal solution. Once the nanotubes interact with the mechanical stimulus, two simultaneous consequences are observed. The first is the exposure of the free surface of the tube, and the second is the shortening of its length. The former is useful for either covalent or non-covalent functionalisation, whereas the latter improves the dispersability [48,49].

Another approach exists named of solvent-assisted dispersion. Bergin et al. published a seminal investigation on this regard, where a thermodynamic analysis is applied in order to determine the maximal solubility of CNTs in different organic solvents [50]. Additionally, they estimated the Hansen solubility parameters of CNTs, which represents a significant contribution in the pursuit of new tailor-made solvents that achieve stable dispersions.

In contrast to the large amount of research performed on the dispersability of CNTs in different media, only one work has dealt with the characterisation of the dispersion within a composite [51]. The study presents a mathematical approach to the characterisation and quantification of the dispersion in matrices, with the drawback that it only works for agglomerates. Since the available analysis equipment fails to resolve individual CNTs in a representative way, the only feature that could be identified and classified is the clustering. Hence, complementary techniques and methodologies are still needed in this field for a proper characterisation of the CNTs distribution in composites.

Coating/Decoration (Exohedral functionalization)

Coating must not be confused with decoration. The first one is related to the full coverage of the CNT surface and can be achieved by several different methods (electrochemical deposition, physical vapour deposition, chemical reduction, etc), whereas the latter is defined as the partial coverage of the surface by in-situ reduction or nanoparticle deposition.

The two techniques have been studied as tools to improve the interfacial bonding between the CNTs and the matrix.

It has been reported that the melting point of metals drops with is related to their net size, in the nanometre scale [52]. This reduction plays a significant role in the interfacial improvement, since a proper integration can be achieved with lower applied energies. This reduction in

thermal energy also reduces the risk of chemical reaction of dangling bonds of the tubes with the atmosphere.

II.4. Metal matrix composites reinforced with carbon nanotubes

The use of CNTs as the reinforcing phase in composite materials has been studied by several different approaches in the recent years. The main focus was made on polymer matrices, since an improvement in some areas (i.e. electrical and thermal conductivity) can be still achieved even after covalently functionalizing the CNTs. This trend can be observed in Figure II-11.

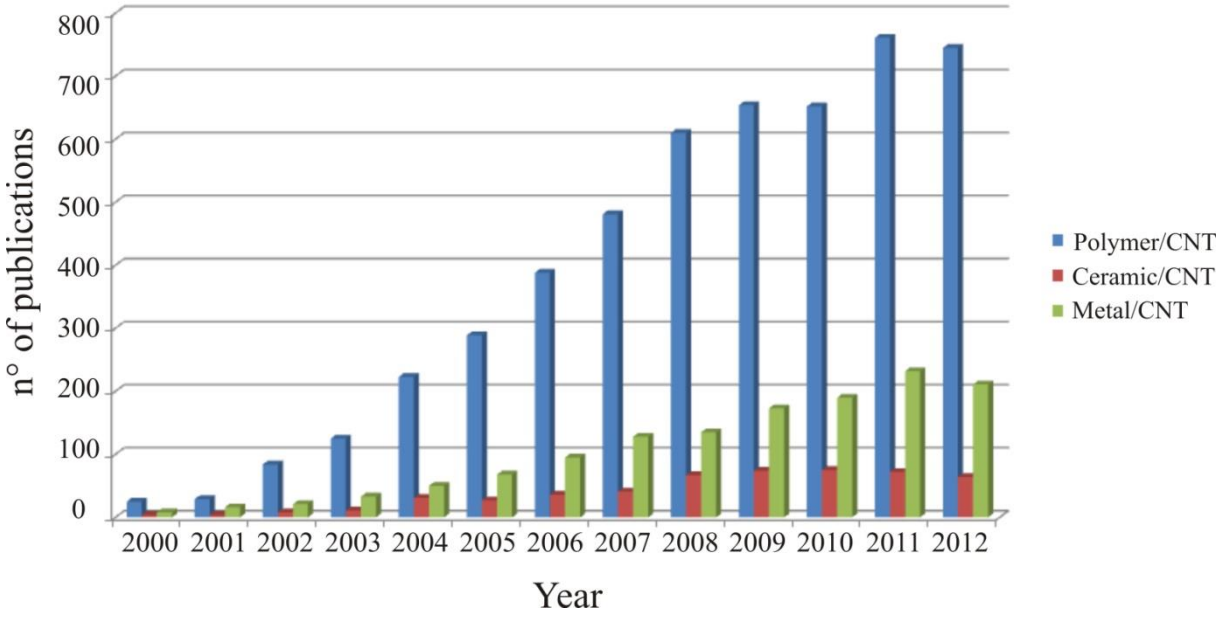

Figure II-11 - Number of journal articles published on CNT-reinforced composites, differentiated by the matrix material. (source: Scopus).

However, when the matrix is a metal, difficulties arise. The deteriorated intrinsic tube properties, as a consequence of covalent functionalization, would reduce the probability of a proper synergetic effect between the matrix and the reinforcement.

An important amount of research can be found in the literature regarding CNT-MMC. Cu-matrices are the most studied with Ni in second place, followed by Al, Mg and Ti, among others [53].

II.4.1. Fabrication techniques of Me-CNT composites

Several techniques have been tested for the production of Me-CNT composites. These techniques comprise both, liquid and solid state processing (related to the state of the matrix material) and the main focus is made on the proper dispersion and distribution of the CNTs throughout the matrices with the lowest possible amount of induced defects.

Particularly, liquid state processing routes provide the possibility of in-situ dispersion and blending of the precursors, prior to the final conformation. However, these processes increase the reactivity of the molten metal with the carbon nanotubes, rendering them prone to degradation.

In the case of solid state processing, the most widespread preparation is mechanical powder mixing by energetic processes such as ball milling [54–58]. This technique is efficient in the CNT dispersion and their subsequent embedding into the metallic particles. It is used for several different metals with dissimilar properties. The main disadvantage of this process is that it unavoidably affects the CNT structure and dimensions, reducing their properties. Furthermore, it has been reported that it could modify some of the metal original characteristics [59].

Another possibility to pre-process Me-CNT composites is wet routes. There are several approaches in this direction, and can present either covalent or non-covalent functionalisation of the CNT surface. The most widespread is the so-called molecular level mixing (MLM) [60]. MLM consists in attaching functional groups to the CNT surface where Cu ions are reduced. As a continuous process, these Cu seeds are grown further on the CNT surface until the nanotube is embedded into a Cu matrix. With this, an optimal integration in the metallic powder is achieved, which afterwards will be consolidated as a porous body. This porous compact is then densified by regular powder metallurgy routes. Since it was first reported, it has been successfully applied to different metallic and ceramic matrices such as: aluminium [61], nickel [62], copper [63], alumina [64], etc.

Another wet chemical route is the heteroaggregation of powders. It is a well known process in the ceramic-materials field and consists in the formation of aggregates by the cohesion of particles of different materials [65]. In the case of Me-CNT composites, it would consist in blending the metallic powder with a stable dispersion of CNTs (functionalised or not), and the subsequent drying of the mixture to obtain composite powders. The mechanisms governing the interaction between the metal and the CNTs in this type of aggregation are still unclear. The

most accepted model is based on the DLVO (Derjaguin, Landau, Verwey and Overbeek) theory of interaction in colloidal suspensions [66].

II.4.2. Interfacial phenomena in Me-CNT composites

An important aspect to consider during solid state processing of metal-CNT composites is the interfacial reactions which could lead to structural decomposition of the nanotube [38]. These interfacial interactions are of critical importance, they are preponderant in the generation of a synergetic effect between matrix and reinforcement. In particular, the strength of a composite material strongly depends on the stress transfer from the matrix to the reinforcement at the interface [14]. Carbon nanotubes are known for their chemical stability throughout a wide range of temperatures, but in a defect-free state. In practice, this is extremely uncommon, since a great amount of defects can be induced in many stages of the processing (i.e. dispersion, mixing, etc.). sp^3 sites can also be found which may induce the formation of side-contact carbides. A typical type of crystallographic defects in sp^2 hybridised carbons are the Stone-Wales defects [67,68].

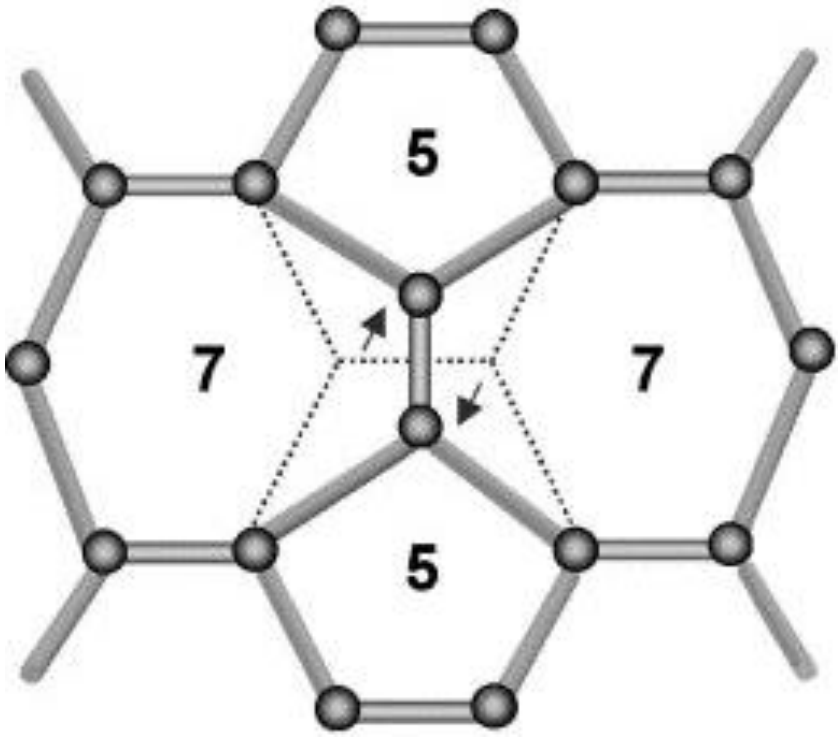

Figure II-12 - Stone-Wales defects in sp^2 carbons [26].

These are produced by the rotation of the C-C bonds reshaping the electronic configuration and the morphology of the graphitic structure (Figure II-12). This reconfiguration provides new reactive sites for chemical interaction.

The most significant effect that can appear is the formation of carbides according to the following chemical reaction:

$$\frac{x}{y}M + C \rightarrow \frac{1}{y}M_xC_y \qquad \textit{(Equation II.5)}$$

The formation of carbides implies a chemical dissociation that may be detrimental to the intrinsic physical properties of the CNTs. By decomposing an sp^2 bond into an sp^3, the scattering probability of an electron or a phonon within the conduction path is significantly increased, leading to a change in the conduction mechanism from ballistic (scatter-free) to quasi-ballistic. On the other hand, the beneficial side of this particularity is that the interfacial strength is increased and therefore the load transfer could eventually be promoted [69]. The most studied example of Me-CNT composites is the Al/CNT system. A stable carbide (Al_4C_3) is formed by direct reaction at locations where an amorphous carbon coating, defect sites and open ends of the CNTs are present [55–57,70–73].

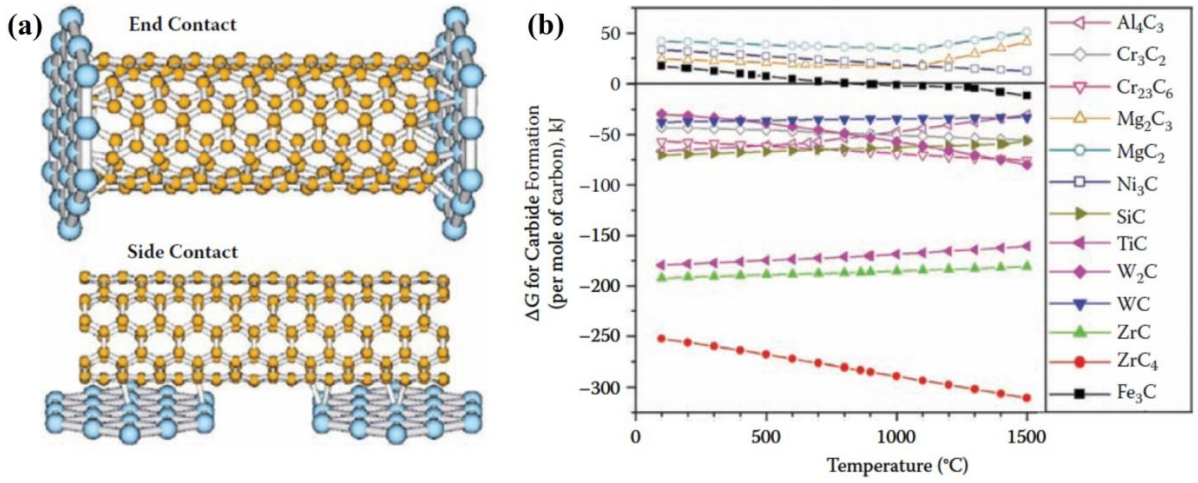

Figure II-13 - (a) Probable reaction sites between metals and CNTs. (b) Gibbs free energy of formation for several metal carbides in a wide temperature range [53].

When working with metals that would form stable carbides (i.e. Al, Cr, Mg) (Figure II-13b), it is recommendable to analyse the thermodynamics of the carbide reaction in advance so as to tailor the amount and influence of these phases in the performance of the composite. Furthermore, depending on the processing method, the reactivity between CNTs and metals can be enhanced and generate either end or side-contacts (Figure II-13a).

The compromise between the improvement of the interfacial interaction and the degradation of the CNT structure should be settled based on the implications on the remaining physical properties.

II.4.3. Synergetic effects in Me-CNT composites

Once a basic understanding of the physical properties and characteristics of CNTs was developed, the aim of the scientific research was shifted towards the improvement of the physical behaviour in composites. Among the studies which could be found in the literature, the focus was made on the enhancement of the mechanical, thermal and/or electrical properties in particular. In the following, a brief summary of some of the reports is showed.

Mechanical properties

The enhancement of the mechanical properties is the most studied phenomenon in Me-CNT composites. Probably, this is due to the straightforward interpretation of the phenomena based on the analysis of results, by the correlation to a well-developed stack of previous studies with other reinforcing phases. Within the reported improvements, the most studied property is the tensile strength. Several different metallic matrices have been reported to exhibit grain boundary strengthening due to microstructural refinement [74–76]. This particularity will be thoroughly explained and discussed in chapter VII of the present work. Another reported strengthening mechanism is the Orowan looping [58], which hinders the dislocation mobility by adding obstacles to their path. In general, improvements in hardness and yield strength are observed, generated by the presence of second phase entities (i. e. CNTs).

As mentioned before, in all cases dispersion plays a fundamental role. It is only possible to exploit the reinforcing effect of the CNTs to its maximum by effectively dispersing them within the metallic matrix. This would not only take advantage of the outstanding intrinsic physical properties of the CNTs, but would help to improve the interfacial contact with the matrix.

Thermal properties

Metals hinder the improvement of their thermal properties. It is well known that metals have high thermal properties (although not as high as the CNTs). However, with the aid of a proper dispersion, the CNTs would be able to enhance the thermal conductivity of metals up to one order of magnitude.

The most studied CNT/metal system regarding its thermal properties is that with Cu matrix due to its potential application in electronics. The overall thermal conductivity was generally decreased due to a variety of problems such as porosity, poor interfacial contact, CNT agglomeration, etc. Edtmaier et al. reported a fivefold decrease in the thermal conductivity of CNT/Cu compared to that of sintered Cu [77]. The given explanation for this decrease is the

poor interfacial connection between reinforcement and matrix. However, as expected, they mention that by improving the dispersion, the thermal conductivity would be expected to significantly improve. Chu also reports a decrease in the thermal properties of CNT/Cu bulk composites [63]. However, in this case the decrease is significantly lower as that reported in reference [77]. From the presented SEM and TEM figures, it is clearly noticeable that the dispersion of CNTs within the matrix is more homogeneous than the one of Edtmaier. The only report showing an improvement of the thermal conductivity in CNT/Cu composites, to date, was published by Cho et al [78]. They measured an improvement in the thermal properties for low CNT volume fractions (up to 3 vol.%). Already at 5 vol.% the conductivity of the composite is below that of pure Cu. Furthermore, they expanded their studies to functionalized MWCNTs in order to improve the dispersion and distribution in the Cu matrix, finding in this case, that a 4-5 nm interfacial amorphous layer hindered the expected improvement of the thermal properties [79]. In a previous work by Kim et al., the thermal conductance of a MWCNT/metal junction was approximately 0.5 W/m.K [8]. In comparison to the conductivities of Cu and CNTs, it becomes clear why they have a detrimental effect.

Electrodeposited MWCNT/Ni thin layers produced by a Watts bath showed a maximum value of 109 W/m.K at 0.7 wt.% CNTs, a very promising result. This value was 80% higher than that of a pure Ni film deposited under the same conditions (60 W/m.K), and even 20% higher than the theoretical value for Ni (90.9 W/m.K). They report that beyond this concentration, the conductivity was lowered due to void formation and discontinuous interfaces [80].

Laser near-net shape melting processing of MWCNT/Ni composites showed a thermal conductivity decrease of more than 50% compared to pure Ni, mainly due to the presence of a large amount of porosity and CNT degradation into carbides [81]. Bulk composites produced by spark plasma sintering presented an anisotropic increase in the thermal conductivity in two different directions up to 3 and 4 vol.% [82]. After these concentrations, the conductivity is constantly decreased, with values always below pure Ni. The authors state agglomeration, CNT winding and interfacial reactions as the greatest causes. In all cases, the researchers tried to predict the thermal behaviour of the composites, to no avail, because the different tested models (Eshelby equivalent model, rule of mixtures, etc.) do not consider the interfacial features as well as the very low probability of having optimally dispersed CNTs (individual tubes) throughout the matrix. These are very promising results that encourage further research in this direction.

Electrical properties

The improvement of the electrical conductivity in a CNT-reinforced metal matrix composite is a non-trivial goal to achieve. Some years ago, an envisioning paper from Hjortstam et al. [83] explored the possibility of achieving an ultra-low resistivity composite material by integrating CNTs as reinforcements. The theoretical analysis shows promising results, but certain conditions must be satisfied to obtain the predicted results. They state that in order to produce a highly conductive Cu/CNT composite three main challenges are to be overcome, namely: (i) high quality CNTs must be produced in industrial quantities, (ii) a method for producing the composites with well integrated and finely dispersed CNTs must be developed, and finally (iii) the manufacturing costs should be reduced so as to allow the CNT usage in mainstream applications. The challenges (i) and (iii) have been at least partially overcome in the years following the publication of the paper, whereas regarding the item (ii), despite progress in the past years, several problems are yet to be solved. The predicted improvement is based on the fact that defect-free CNTs present ballistic conduction and the integration to the matrix is seamless. In the practice, this has not yet been achieved, observing an increased amount of defects in the dispersion stage and a low interfacial integration of the CNTs in the matrix. Moreover, there is still a wide discrepancy regarding the interaction between tubes in the electric conduction. For example, among the proposed mechanisms, some authors report that there is a Fano resonance effect between the tubes [84,85]. Another hypothesis is the resonant tunnelling coupling between tubes for electrical charge transfer [86,87]. All these effects are sources of energy loss and were not considered in the aforementioned theoretical preview published by Hjortstam.

II.4.4. CNT-reinforced composites: *issues to be considered*

As a general rule, the experience gathered from the extensive literature published on this topic defines certain important issues to be addressed in order to obtain an optimal functional composite, namely:

- Dispersion and distribution of the CNTs within the matrix.
- Functionalisation (covalent or non-covalent) as an efficient route towards optimal reinforcement.
- Powder blending depends strongly on the final densification route.
- CNT/Metal interfaces define the transfer properties.

III. Materials and methods

III.1. Materials

III.1.1. Matrix material

The selected matrix material for this work was Nickel (Ni) dendritic powder, provided by Alfa Aeasar GmbH & Co KG (Figure III-1). The powder purity is 99.8% and the mean particle size is 44 μm (mesh -325). Table III-1 summarises the physical properties of Ni.

Table III-1 – Physical properties of Nickel.

Property	Density	Melt. temp.	Enth. of fusion	Spec. heat cap.	Thermal cond.	Electrical cond.	Coeff. of therm. exp.
Symbol	ρ	T_m	ΔH_f	C_p	λ	σ	CTE
Units	g/cm^3	°C	kJ/mol	kJ/kg.K	W/m.K	10^6 S/m	10^{-6}/°C
Value	8.9	1453	17.48	0.4186	90.9	14.4	16.3

The concept behind using a dendritic-type metallic powder for this study is to take advantage of the larger specific area for the improvement of the deposition of the MWCNTs on its surface and a better sinterability.

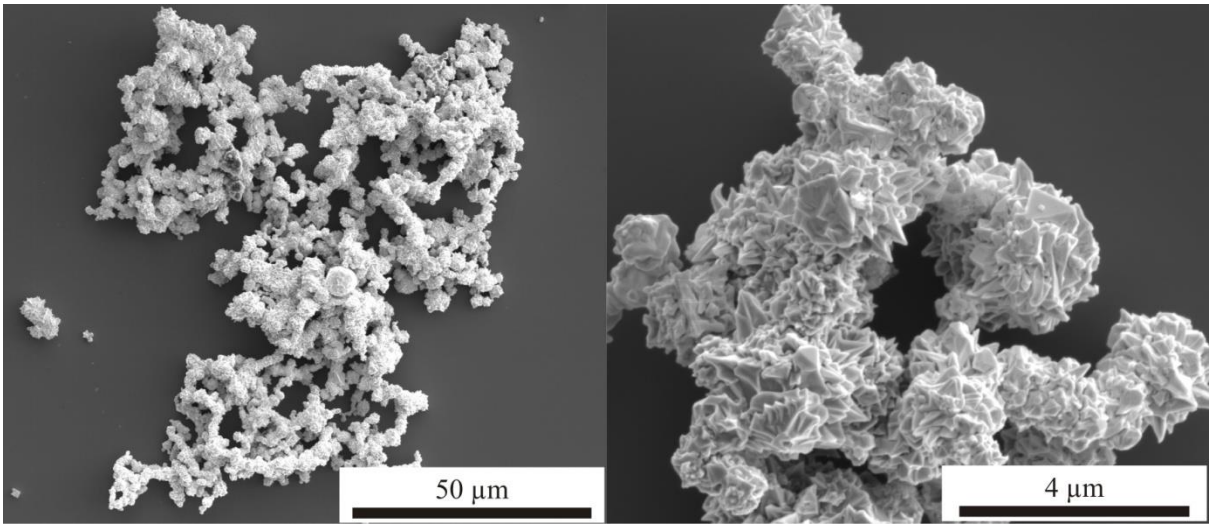

Figure III-1 – SEM pictures of the Ni dendritic powder.

The Ni powder was initially studied by X-ray diffraction so as to assess whether the powder showed significant native oxidation. The only observed diffraction reflections were those typical of pure Ni (see Figure III-2).

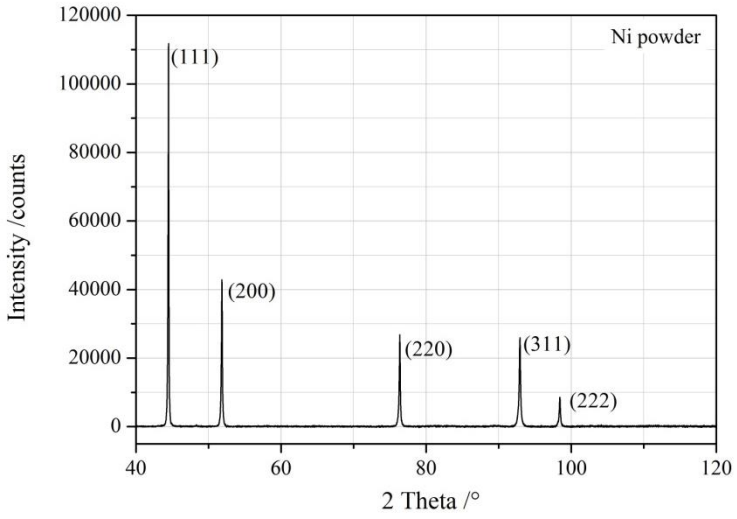

Figure III-2 – XRD spectrum of the starting Ni powder.

III.1.2. Reinforcing material

Multiwall carbon nanotubes produced via catalytic chemical vapour deposition (CCVD) were used as reinforcements (Baytubes C150P, Bayer Materials Science). The as-received powder is in the form of agglomerates of several MWCNTs, making their handling easier as compared to colloidal solutions. The characteristics of the MWCNTs are summarised in Table III-2.

Table III-2 – Characteristics of the used MWCNT (Baytubes C150P).

Property	Unit	Value
C-Purity	%	> 95
Free amorphous carbon	%	undetectable
Number of walls	-	3−15
Outer mean diameter	nm	13−16
Outer diameter distribution	nm	5−20
Inner mean diameter	nm	4
Inner diameter distribution	nm	2−6
Length	µm	1−10(+)
Loose agglomerate size	mm	0.1−1
Bulk density	g/cm^3	0.14−0.16
MWCNT density	g/cm^3	1.3

Electron microscopy analysis revealed that the agglomerates are about 500 µm in average and tightly packed (Figure III-3a). Further TEM analysis revealed that the agglomerates consist of a mixture of morphologies, the nested-tube type being the most predominant, followed by the herringbone type (Figure III-3b).

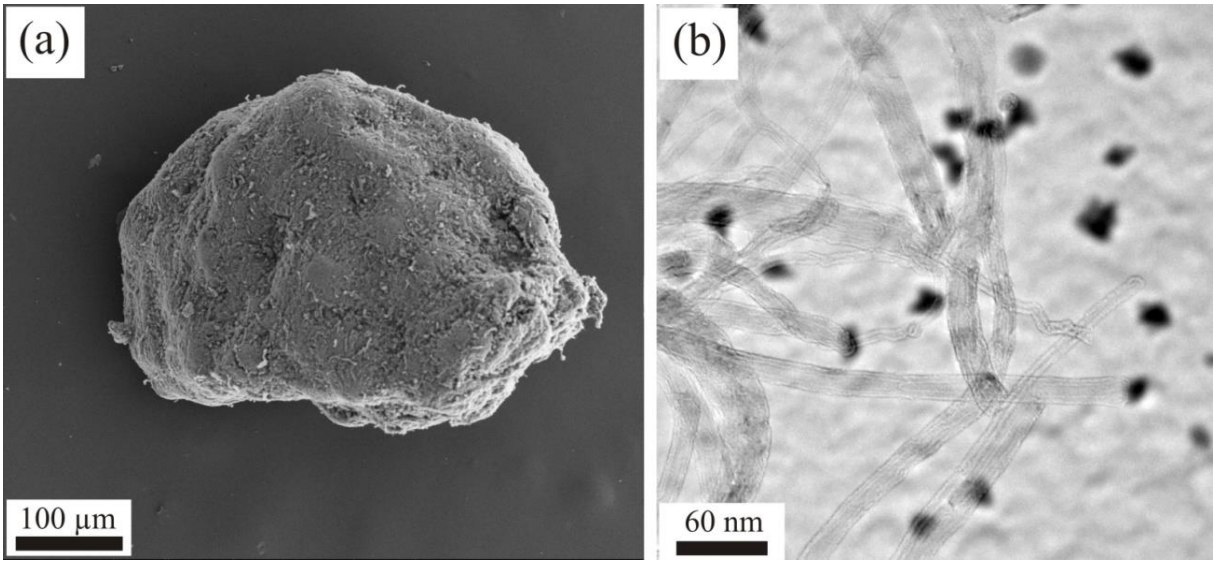

Figure III-3 – (a) scanning electron micrograph of an as-received MWCNT bundle, (b) transmission electron micrograph of the Baytubes C150P used in this work.

The XRD spectrum of the MWCNT powder showed the typical graphitic reflections (Figure III-4a). The reflections of higher intensity correspond to the basal plane family {001}.

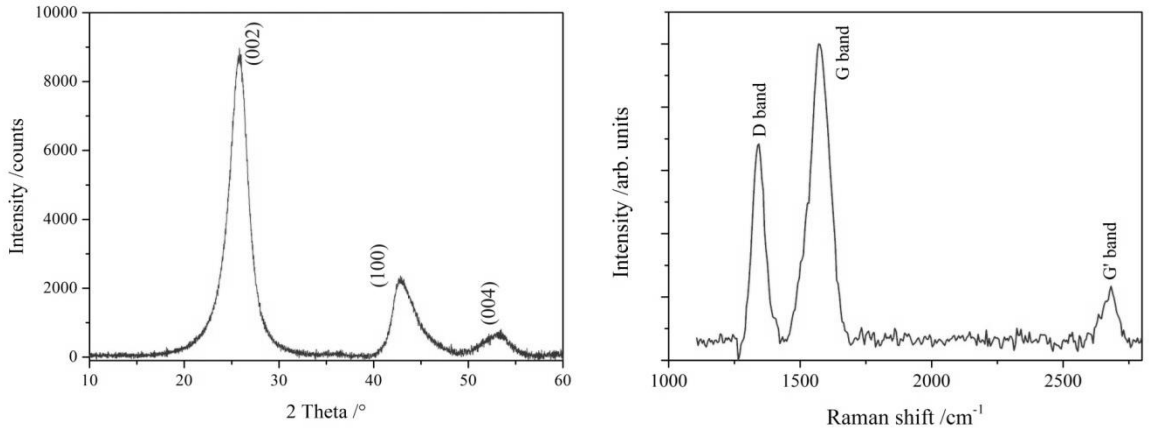

Figure III-4 – XRD and Raman spectra of the starting MWCNTs.

The Raman spectrum of the initial MWCNT agglomerates shows the three characteristic bands of CNTs (Figure III-4b). The Raman signal is quite noisy and with broad peaks, depicting low-crystallinity bundles. The initial ratios that indicate the defect and purity state are the I_D/I_G (quality-related) and $I_{G'}/I_D$ (purity-related) respectively. Initial measurements gave 0.683 and 0.343, respectively.

III.2. Precursors processing methods

III.2.1. Carbon nanotubes processing: Dispersion, characterisation, powder blending

As already mentioned in the theoretical part, one of the fundamental aspects to be considered when working with CNTs as reinforcing phases is their dispersion throughout the matrix. For that, a proper dispersion and blending method must be either chosen from the literature or developed. In the case of this work, the utilised method is an adaptation of a well established blending method called colloidal processing [88]. This method consists of a series of steps to ensure the proper integration of the CNTs in the metallic powder.

The first step consists in the dispersion in an ultrasound bath of a determined quantity of CNT agglomerates in an organic solvent. The first selected organic solvent was N,N−dimethylformamide (DMF) based on a previous study performed by Inam et al. [89] for ceramic composites. Since DMF is considered hazardous for the health, several other solvents were tested within this work in order to find a replacement [90]. After experimental investigations, it was determined that ethylene glycol (EG) would be a suitable replacement for DMF and the CNT concentration was fixed in both, EG and DMF, at 0.2mg/mL [90].

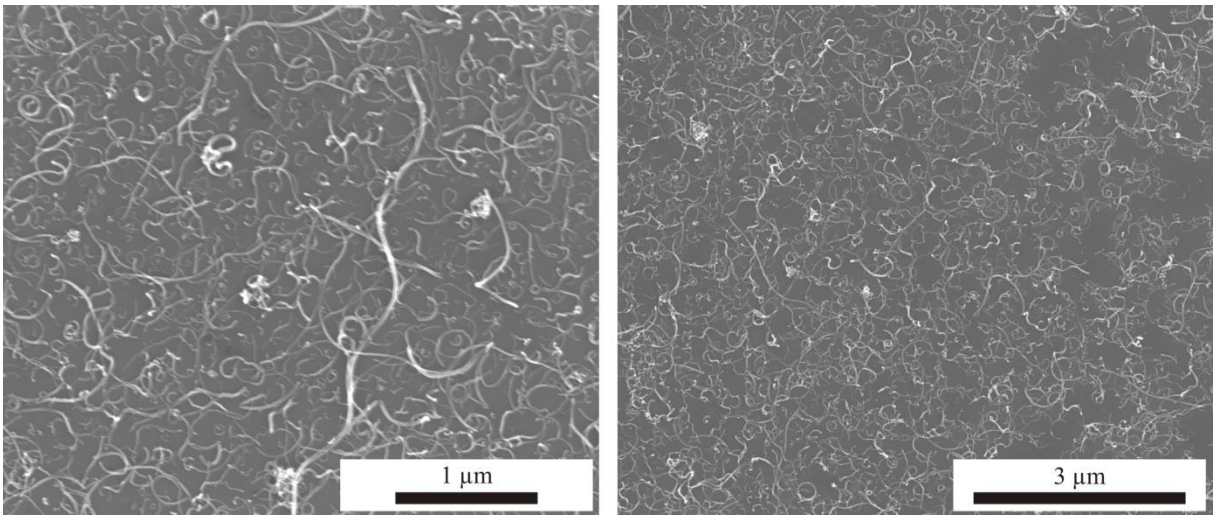

Figure III-5 – Electron images of the MWCNTs dispersed in EG and dried onto Si substrates.

Figure III-5 shows results of the dispersion of MWCNTs in EG. Small volumes were taken from the suspension and were subsequently dried on top of a Si substrate, achieving outstanding dispersion without significantly shortening the CNTs. This is important since their reinforcing effect depends strongly on their length. Moreover, very good dispersion stability was achieved with EG, reaching up to few days without observable coagulation. It is believed that this

extended dispersion stability is due to a chemical solvation by the solvent molecules [90]. The dispersion time was fixed at 10 minutes. An extended discussion on the selection of the time is provided in chapter IV.

The second step is the addition of the metallic powder to the stable MWCNT dispersion and the successive ultrasonic mixing. The different MWCNT/Ni weight ratios were 1.0, 2.0, 3.0 and 5.0 wt.% (6.5, 12.3, 17.5 and 26.5 vol.%, respectively) and are indicated in Table III-3. The blending time was set to 5 minutes [90].

Table III-3 – Partial fractions of CNTs and Ni for the manufactured samples.

CNT weight fraction [%]	CNT volume fraction [%]	CNT weight [mg]	Ni weight [mg]
1.0	6.47	8	792
2.0	12.26	16	784
3.0	17.47	24	776
5.0	26.48	40	760

The last step is the drying and grinding of the powder. The reagent glasses with the colloidal suspensions are placed in a ventilated furnace at 150 °C and are evaporated for a period of 4-5 hours. After the blend is dry, the powders are scrapped out of the glasses and lightly grounded in an agate mortar. The resulting product consists of CNTs coating the surface of the metallic powder as shown in Figure III-6.

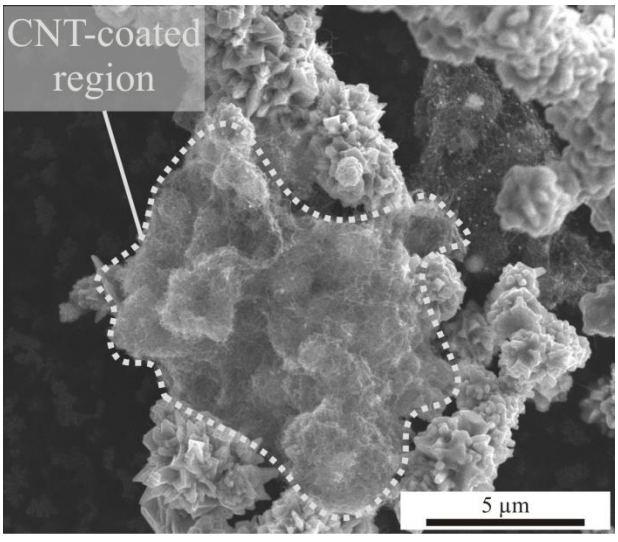

Figure III-6 – Ni dendritic particle coated with dispersed MWCNTs. This is the typically obtained product of the colloidal mixing process.

III.2.2. Consolidation and Sintering

The selected manufacturing methods for this work were two: pressureless sintering (CPS) and hot uniaxial pressing (HUP). For both processes, the powder mixtures were previously consolidated into green pellets with a diameter of 8 mm and variable height ranging from 1 to 5 mm. The consolidation of the powders was performed in a hydraulic press at room temperature. The applied pressure was 990 MPa for 5 minutes. The relative densities of the green pellets were about 68-70 %.

Pressureless sintering was done in a tube furnace under following conditions.

- Working vacuum: 10^{-5} mbar
- Temperature: 950 °C
- Dwell time: 2.5 h
- Heating rate: 1 °C/min

The heating rate was limited by the thermal expansion/contraction rate of the Al_2O_3 furnace tube that could induce stress cracking leading to vacuum leakage.

The other densification process was hot uniaxial pressing (HUP), which consists in placing the green pellet within a graphite sleeve, between two alumina pistons. An axial pressure is applied and induction heating is generated by eddy currents circulating in the external heat-resistant steel mould. During the process, the chamber is under vacuum (10^{-6} mbar) to avoid oxidation of the metallic components. The experimental parameters for HUP were:

- Working vacuum: 10^{-6} mbar
- Temperature: 750 °C
- Dwell time: 2.5 h
- Heating rate: 15 °C/min

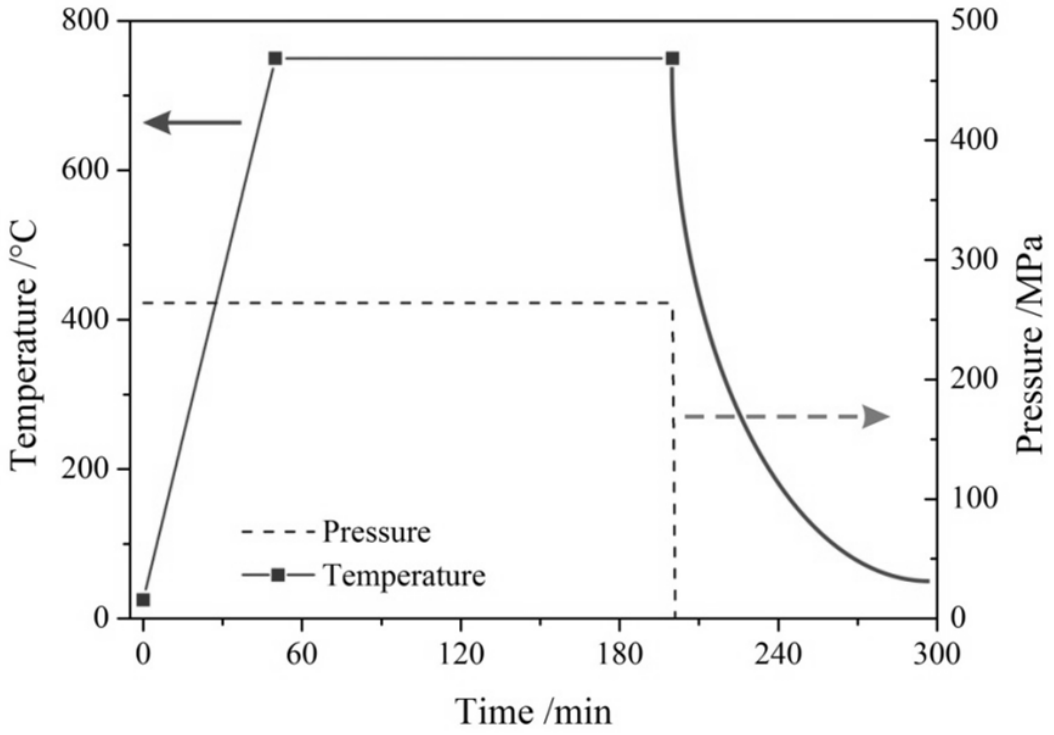

Figure III-7 – Temperature and sample pressure evolution through the sintering process.

The maximum treatment temperature is limited by the heating circuit capabilities After the heating and isothermal steps are finished, the cooling stage is limited up to temperatures about 120-150 °C, mainly due to difficulties in the heat dissipation under vacuum. The temperature and pressure evolution are schematically depicted in Figure III-7.

III.2.3. Post-processing characterisation

Due to the difficulties in the preparation of the MWCNTs for their characterisation, the sample preparation protocols suggested by Decker and co-workers were adopted in this work, particularly for electron microscopy [91].

Scanning electron microscopy/ Focused ion beam

The electron microscopy characterisation was performed in two different dual beam systems (Helios NanoLab 600 and Strata DB 235) from FEI. The electron column was operated in both cases at 5 kV. Both microscopes are equipped with secondary electrons, through-the-lens (TLD), backscattered electrons and energy dispersive X-ray spectroscopy (EDS) detectors.

Electron Backscattered Diffraction (EBSD)

Grain size distributions of the composites were studied by means of electron backscattered diffraction (EBSD) (EDAX TSL®) within the Helios NanoLab 600. The analysis consists in an automatic scan of a determined surface recorded by means of a DigiView camera system. The

resulting Kikuchi patterns are compared in real time to known phases (in this case, nickel) and indexed (see Figure III-8).

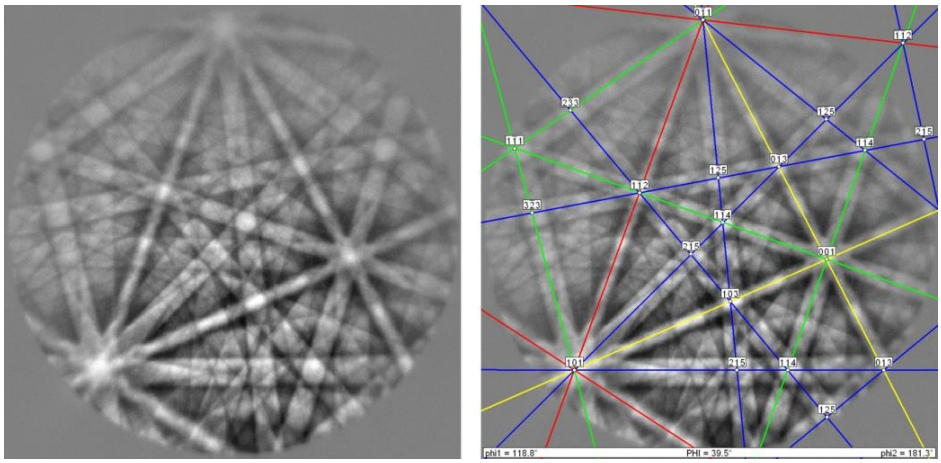

Figure III-8 – Kikuchi diffraction patterns for an FCC metal and the indexed planes.

Finally, a crystallographic orientation map is produced, from which several studies could be performed, namely: orientation distribution, grain boundary reconstruction, neighbouring grains misorientation, phase recognition, etc. Additionally, it is possible to perform a quantitative analysis of the scanned area by determining the grain size distribution, misorientation distribution, etc. The acquisition as well as the post-processing of the data is made using the OIM Software (TSL). The results are presented either in the form of inverse pole figure maps (IPF), with the corresponding pole figures (PF), as single-grain colour maps or as image quality (IQ) grey scale maps.

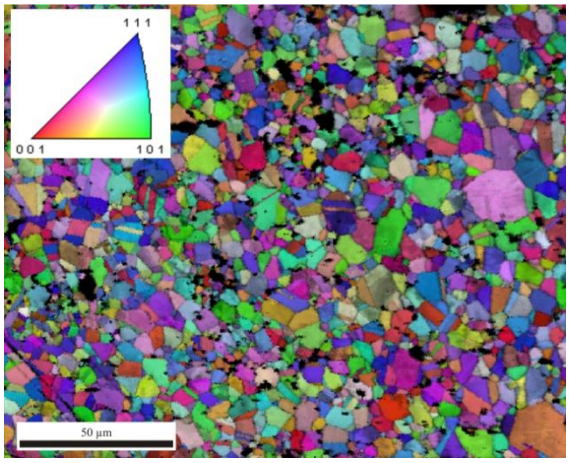

Figure III-9 – IPF + IQ map of a MWCNT/Ni composite. Each colour represents a different crystallographic orientation.

EBSD was performed using a voltage of 20 kV, a current of 22 nA, and a step size of 500 nm. A grain was defined as at least two adjacent points with maximum 5° misorientation. The raw

data was cleaned using confidence index standardisation within each grain. Points with a confidence index smaller than 0.1 were dismissed. An example of a processed image for a MWCNT/Ni 1.0 wt.% sample is shown in Figure III-9.

Transmission Electron Microscopy (TEM)

The interface between the Ni matrix and MWCNTs as well as the morphology of the MWCNTs was evaluated by high resolution transmission electron microscopy (HRTEM) on a Philips CM 200 at 200 kV acceleration and a point resolution of 0.19 nm. Further analyses were carried out on a JEOL JEM2011 also at 200 kV and a point resolution of 0.18 nm. Both TEMs have a LaB_6 electron source and are equipped with EDS detectors. The TEM samples were prepared in the Helios Nanolab 600 dual beam microscope, using a lift-out technique. The prepared TEM foils were transferred to Cu semicircular grids 3 mm in diameter.

Raman spectroscopy

Raman spectra were acquired with an inViaTM Raman microscope (Renishaw), working with a Nd:YAG laser with excitation wavelength 532 nm and a 2400 l/mm grid. Reported spectra are averaged from three in same spot. A cosmic rays removal filter was also applied to the measurements.

For random distributions of nanotubes, the intensity of the characteristic G, D and G' bands is proportional to the amount of nanotubes within the measured volume. Provided that their intensities are sensitive to the beam focalisation, it is usual and accepted in Raman experiments to normalise the measured intensities to an internal reference, such as the most intense band [92]. Then by normalizing the spectra, the comparisons between samples are made by comparing relative intensity ratios and not individual band intensities.

X-Ray Diffraction (XRD)

XRD was used for the crystallographic analysis and the grain growth evolution study of the composites. All the XRD measurements in this work were performed in a X'Pert MPD X-ray diffractometer in a θ-θ geometry configuration (Figure III-10). The samples were irradiated by a Cu source with a CuKα wavelength of 0.15406 nm. The Bragg angle range was determined specifically for each study.

The diffractometer has the possibility to attach a high temperature chamber (Anton Paar HTK 1200 HT) to perform heat treatments or sintering processes and analyse the phase and grain size evolution in-situ. The chamber has the capability to work under vacuum and heating up to 1100

°C with heating rates up to 20 °C/min. Grain growth evolution during sintering and the lattice thermal expansion of the composites were measured in vacuum (10^{-6} mbar).

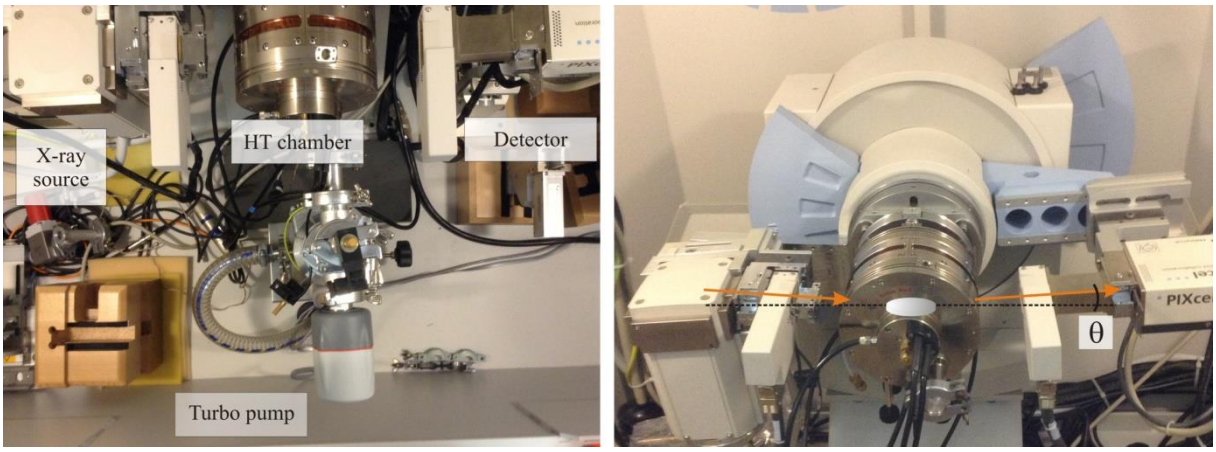

Figure III-10 – Schematic distribution of the high temperature chamber configuration within the X-ray diffractometer. The depicted configuration is for a Bragg-Brentano measurement type.

The incident and diffracted optical geometries were parallel and the diffraction angle (2θ) was varied from 40º to 130° with a step size of 0.0131° and a 0.5 s/step rate and the irradiated area ranged from 11.7 mm^2 for the (220) reflection to 19.2 mm^2 for the (111) reflection.

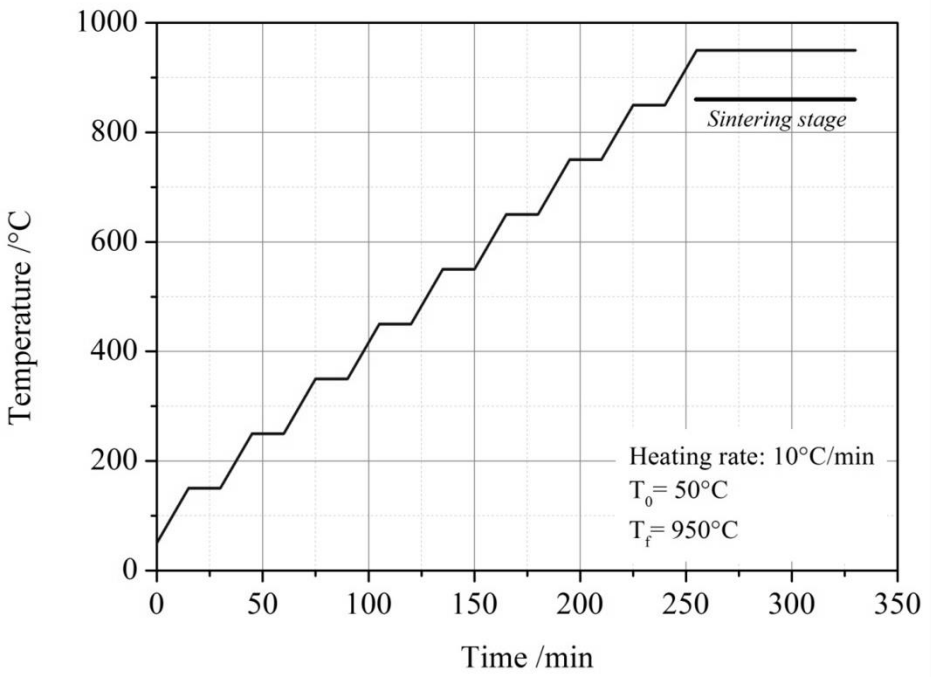

Figure III-11 – Temperature evolution through the HT-XRD process.

The applied voltage and current were 40 kV and 40 mA, respectively. For the HT-XRD measurements, the samples were heated from 50º to 950° C at 10 °C/min and the diffractograms were obtained every 25 °C after 15 minutes of thermal stabilisation (Figure III-11). The

temperature distribution in the sample was thus homogenised and errors due to temperature gradients were reduced.

Mechanical properties: micro indentation

The mechanical properties were tested in a Vickers microhardness indenter (Struers DuraScan 50/70/80). The measurement principle consists in a pyramidal diamond indenter penetrating with a certain applied load for a defined period of time and is based on the international norm ASTM E-384. After the indentation, the indentation diagonals are measured and the hardness is determined by $HV = 0.1891F/d^2$, with d the mean value of the two measured diagonals. The indentation column has a Z-axis resolution of 5 nm. The post-processing is made with the ecos Workflow software.

The selected indentation force was 980.7 mN (0.1 Kgf) and the indentation time was 15 seconds. The results are expressed as HV0.1, which represents the hardness values for a testing load of 0.1 Kgf. The main advantage of this test is that very accurate readings can be made, using only one type of indenter for all types of metals and surface treatments. Moreover, it is possible to directly correlate the yield strength of materials to their Vickers hardness.

Thermomechanical properties

The thermal expansion data were collected in a Dilatronics II differential and vertical Theta industries Inc high resolution dilatometer (Figure III-12) at a constant heating rate of 5 °C/min under Ar(4.6) flow. The device has an accuracy of 0.5% in the expansion measurement and can work from room temperature up to 1700 °C. It has a dual push-rod for the differential sensing of the dimensional changes during the thermal cycling. The apparatus is linked to a data logger were the expansion data is plotted in real time. The measurements were previously calibrated with silica glasses of the same thicknesses as the tested samples.

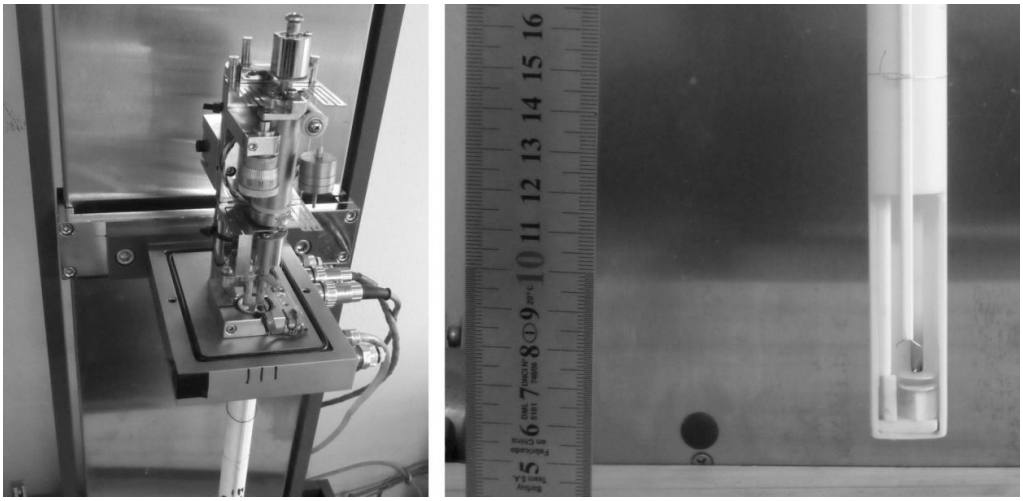

Figure III-12 – Linear differential dilatometer.

Tribological behaviour

The tribological tests were performed with a nanotribometer using a ball on disc configuration in a linear reciprocating sliding mode (CSM Instruments, *Figure III-13*) with a stroke length of 0.6 mm and a total sliding length of 60 mm. The normal force was set to four different loads, namely, 50, 100, 200 and 300 mN and the linear sliding speed to 1 mm/s. The counterbody consisted of an Al_2O_3 ball with a diameter of 3 mm. Temperature and relative humidity were kept constant at 20 ± 2 °C and 4 ± 1%. Subsequently, the wear volume was determined by means of white light interferometry (WLI).

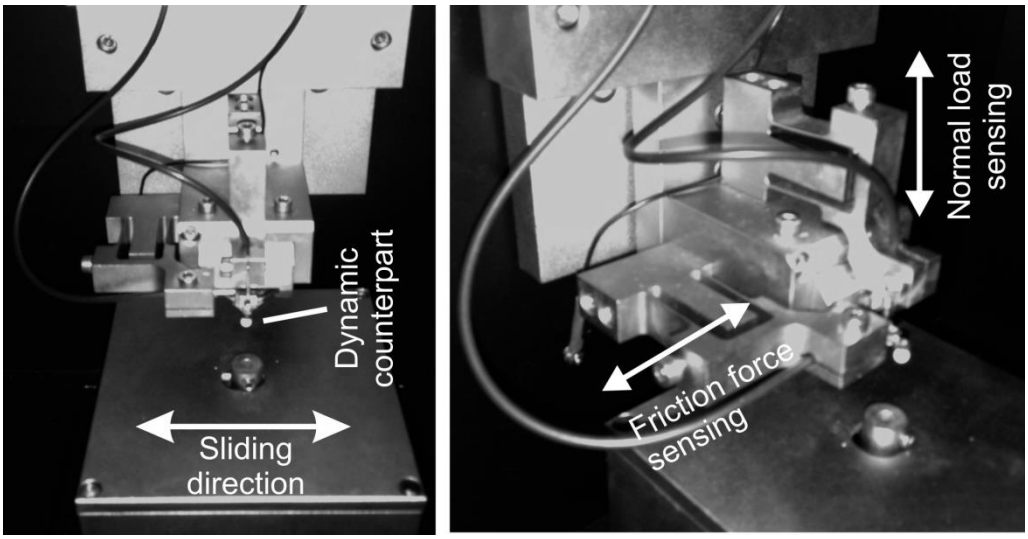

Figure III-13 – Overview of the tribometer constituents.

Electrical properties: electrical conductivity (4 point probe method).

The electrical properties were measured with a standard 4-point probe method (*Figure III-14*). The sample is placed and fixed from opposite sides with bronze screws. Under the samples are placed two parallel high-purity Ag wires separated by a fixed distance, which will probe the voltage drop in this section. The electrical resistance (R) of the sample region is measured by taking a set of points and fitting a linear function to the experimental data. The specific resistivity is obtained by $\rho = R.A/l$; A is the cross-sectional area and l is the distance between the Ag wires.

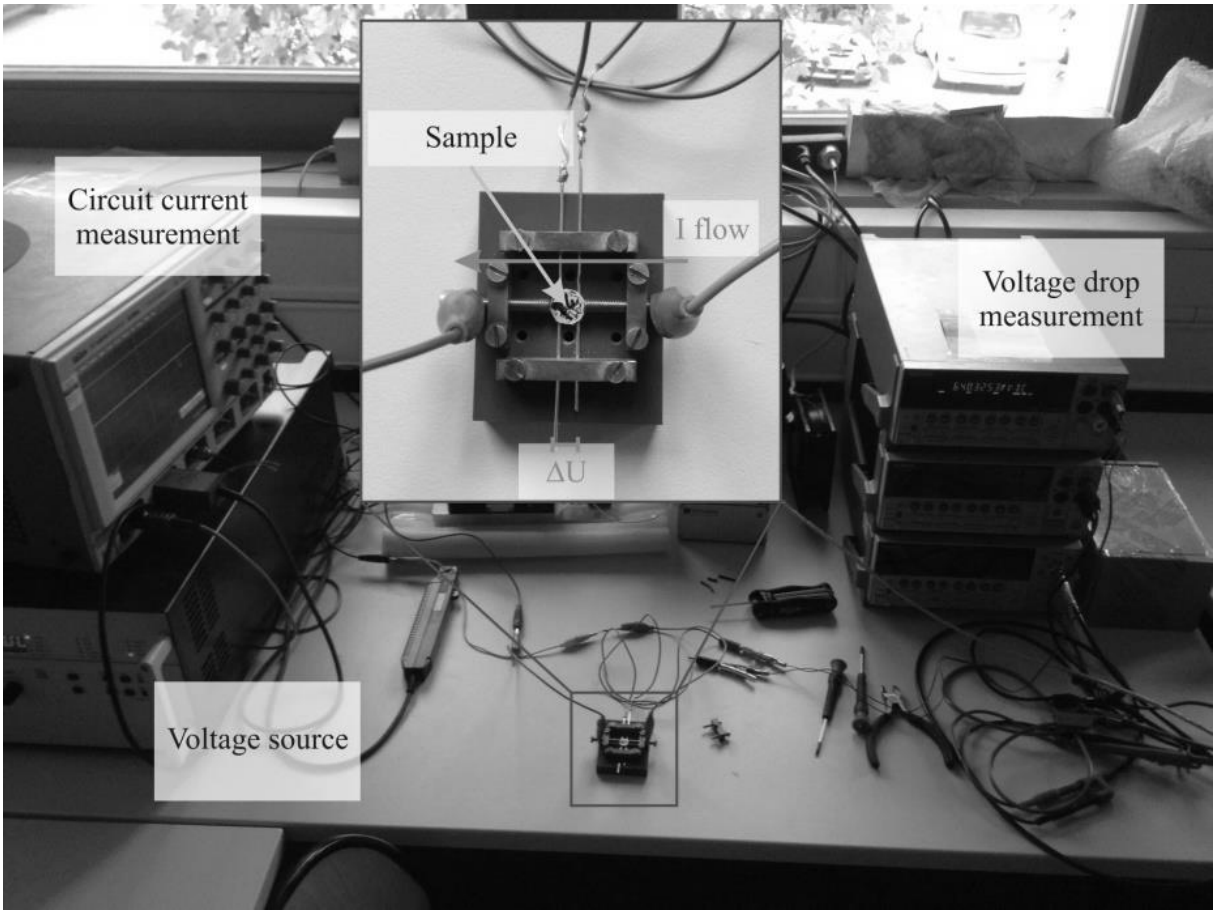

Figure III-14 – Schematic representation of the 4 point probe measurement device. In the inset, the current flow and the voltage drop are highlighted.

IV. Precursor processing and MWCNT degradation analysis

IV.1. Introduction

CNTs might be suitable candidates as reinforcing phases in composites due to their remarkable set of physical properties. However, there are several issues to address regarding their processing [53,93]. The main drawback of these reinforcements is their strong agglomeration due to van der Waals interactions which may hinder an adequate distribution and a consequent property enhancement [89]. A great amount of research has been devoted to this topic, mainly focusing on achieving stable CNT dispersions by covalent functionalisation of the tube surface [94]. However, this presents an important concern regarding the loss or decay of intrinsic properties [95]. When the reinforced material is a metal with already acceptable physical properties, this loss becomes of unavoidable importance, since the lowered reinforcing effect of the CNTs might be rendered marginal or even detrimental to the composite. Therefore, an approach without CNT modification is crucial for a proper enhancement of the composite properties.

Another issue is the matrix/reinforcement interfaces. It has been observed that the CNTs can chemically react with the metallic matrix through side contacts or open ends with dangling carbon bonds [53,96]. This would further translate into CNT degradation, with subsequent property decrease. CNTs tend to interact in different ways with the metallic matrices. The most representative case is observed in CNT/Al, in which an interfacial Al_4C_3 layer is created by the application of pressure and temperature [71]. This carbide layer improves the adhesion but decomposes the tube, being detrimental to e.g. the thermal properties. Differing reports regarding the formed interfaces in CNT/Ni systems can be found. Yamanaka et al. [82] reported a sharp interface with no byproducts obtained by spark plasma sintered MWCNT/Ni blends. On the other hand, Hwang and co-workers [96] were able to synthesise and stabilise Ni_3C nanocrystals by using the CNTs as feedstock. They have recently found that this phase is observed on the interface in CNT/Ni composites produced by spark plasma sintering [62], contradicting the report of Yamanaka. Other reported routes to produce this carbide are based on non-equilibrium highly energetic procedures such as mechanical alloying [97].

The purpose of this chapter is to report a straightforward blending process based on the colloidal mixing of the CNTs with a metallic powder. The condition of the CNTs after the colloidal processing and throughout the consolidation and sintering process of the metal matrix composites by powder metallurgy is spectroscopically analysed. Moreover, the phase evolution and reaction within the sintering process was analysed with the aid of high temperature X-ray diffraction and thermodynamic simulation.

IV.2. Results and discussion

IV.2.1. Dispersion and blending

Throughout the processing and subsequent sintering, the CNTs are subjected to strong thermal and thermomechanical loads that may modify their structure. During dispersion, a strong load is exerted by the ultrasound on the agglomerates with the aim of breaking them up. This interaction is well identified and also shortens the tubes improving the dispersability [95]. However, this change in the aspect ratio might as well represent a decrease in the load transfer efficiency of the composite [98,99].

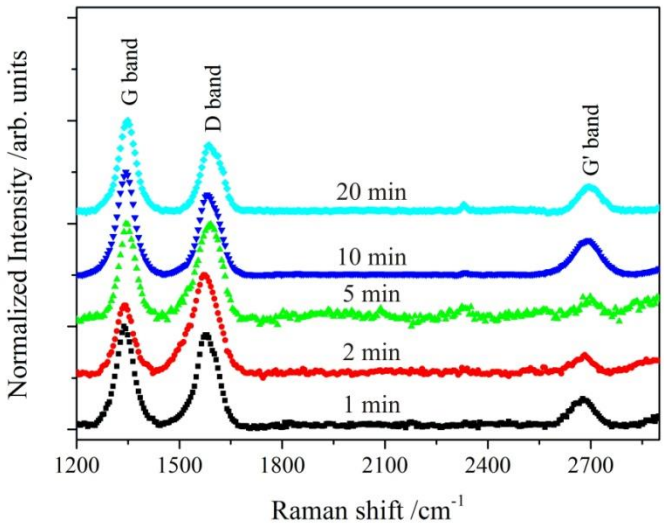

Figure IV-1 - Raman spectra of a MWCNT/EG dispersion measured at different exposure times.

In order to determine the optimal dispersion time without significant process-induced defects, Raman spectroscopy studies were performed by taking aliquots after 1, 2, 5, 10 and 20 minutes of ultrasound processing (Figure IV-1). The evaluation of the structural status of MWCNT can be additionally analysed by observing not only the traditional I_D/I_G ratio, but also the evolution of the $I_{G'}/I_D$ [100]. Both intensity ratios depict the amount of defects and the carbonaceous

purity of the samples, respectively [101]. Furthermore, by analysing the coherent length of the nanotubes it is possible to determine how defective the MWCNTs are. This length (L_a) depicts the distance that separates two consecutive structural defects on the structure. This relationship is inversely proportional to I_D/I_G and is related particularly to the excitation wavelength (λ) utilised in the Raman spectrometer, as described by following equation [102]:

$$L_a = (2.4x10^{-10})\lambda_{laser}^4 \left(\frac{I_D}{I_G}\right)^{-1} \qquad \text{(Equation IV.1)}$$

The resulting L_a values are summarised in Table IV-1.

Table IV-1 – Normalised intensity values and ratios for the three most important bands of MWCNTs (D, G and G' bands).

Time	I_D	I_G	$I_{G'}$	I_D/I_G	$I_{G'}/I_D$	L_a (nm)	State
0	0.683	1	0.234	0.68	0.34	28.1	*Non-dispersed*
1	1	0.917	0.296	1.09	0.30	17.6	
2	0.704	1	0.225	0.70	0.32	27.5	
5	1	0.990	0.291	1.01	0.29	19.0	
10	1	0.778	0.336	1.29	0.34	14.9	*Dispersed*
20	1	0.761	0.357	1.31	0.36	14.7	

The selected MWCNTs present very defective initial structures. Even though the quality and purity parameters are better for exposure times lower than 10 minutes, the fact that the CNTs are not properly dispersed makes them unsuitable for the blending. The first clear observation of a proper dispersion is noticed at 10 minutes of ultrasound, with insignificant modification in the following 10 minutes (see Figure IV-2 a-f). Interestingly, the quality (I_D/I_G) and purity ($I_{G'}/I_D$) markers as well as the inter-defect distance do not considerably change between 10 and 20 minutes of ultrasound. Therefore, after Raman evaluation, the chosen dispersion time was fixed at 10 minutes of ultrasound bath. This processing time allows a quick disentanglement of the CNT bundles and provides a time window of 10 minutes were the blending can be performed without further modification of the CNTs.

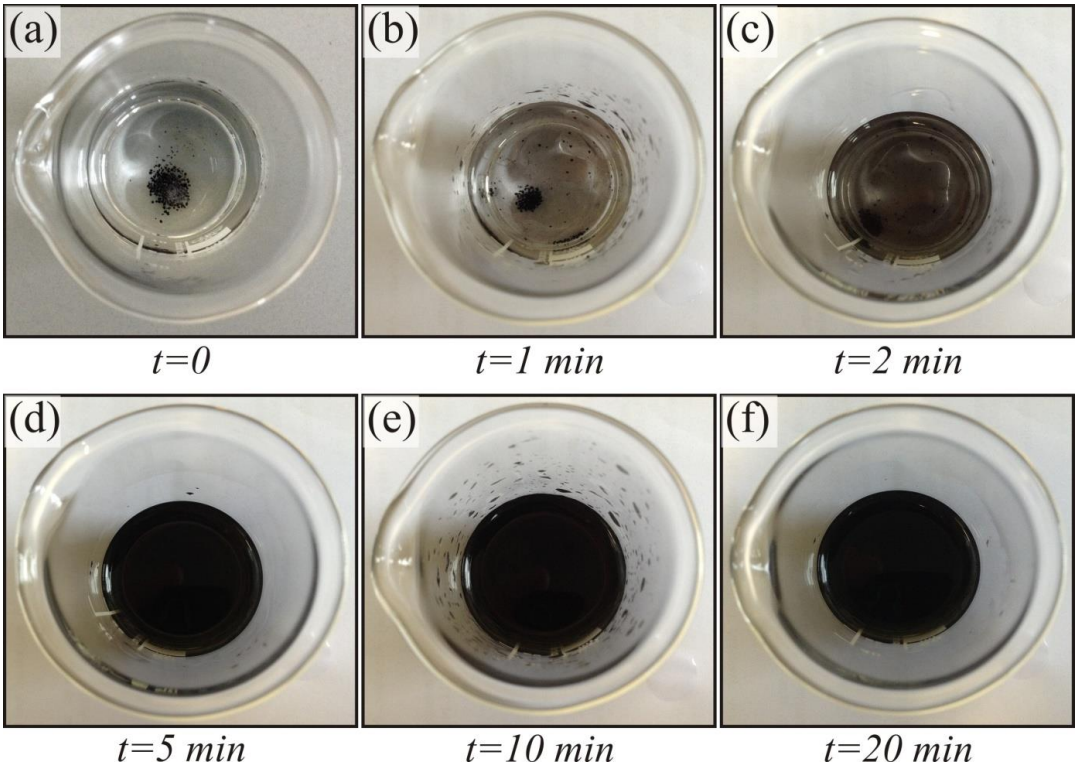

Figure IV-2 – Different stages of the MWCNT dispersion in ethylene glycol. (a) initial state, (b) after 1 min, (c) after 2 min, (d) after 5 min, (e) after 10 min and (f) after 20 min. The dispersion is unacceptable up to 5 minutes of ultrasound due to the visual detection of large MWCNT agglomerates.

Figure IV-3 presents the results obtained for the dispersion in Ethylene Glycol (EG) after 10 minutes of ultrasound analysed with electron microscopy. For the evaluation, the dispersion was dried onto a Si wafer and observed in SEM. It is interesting to note that the MWCNTs are finely dispersed with no large agglomerates observable.

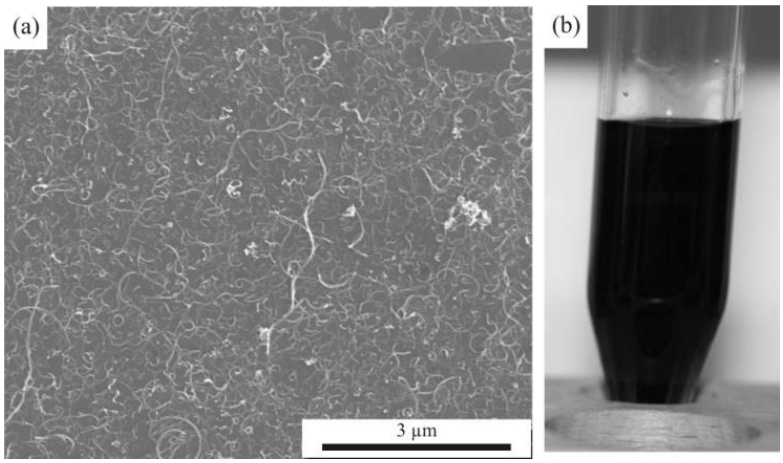

Figure IV-3 – SEM micrographs of: (a) dried MWCNT dispersion, (b) MWCNT/EG colloid after dispersion in ultrasound.

The next evaluation step is to observe the MWCNT/Ni system after the colloidal blending process and the distribution of the nanotubes within the metallic particles. Figure IV-4 shows

the initial state of the MWCNTs as agglomerates (Figure IV-4a), the starting Ni dendritic powder (Figure IV-4b) and the final product after the evaporation of EG (Figure IV-4c). In the latter, it is observed that the dispersed MWCNTs tend to coat the surface of the Ni particle. Interestingly, despite being distributed over the metallic powder surface, the sintering and final density of the composites was not significantly affected, achieving, in some cases, (i.e. 1 wt%) almost full densification (approx. 99%).

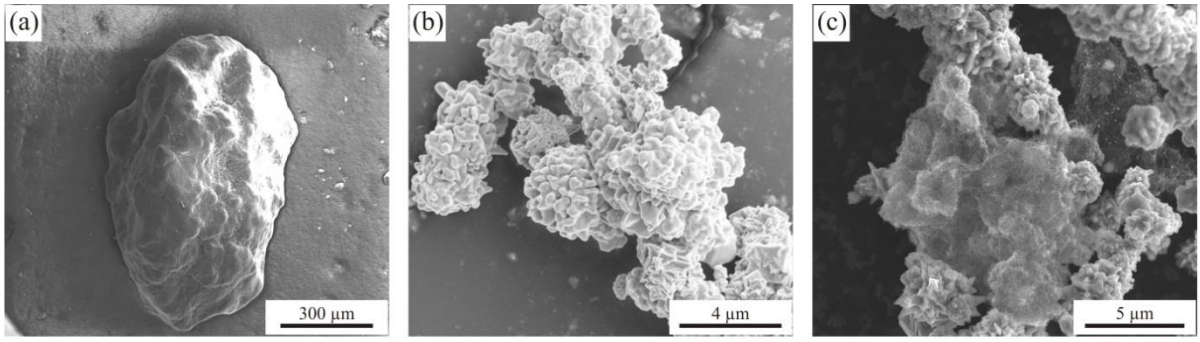

Figure IV-4 – SEM micrographs of: (a) as-received MWCNT agglomerate particle, (b) starting dendritic Ni particles and (c) MWCNT-coated Ni dendritic powder after solvent evaporation.

IV.2.2. CNT degradation analysis

CNT structural integrity assessment

As a reference for the following analysis, the Raman spectrum of the initial state of the agglomerates is shown in Figure IV-5a. The amount of defects and impurities is studied by comparing the relative intensities of the characteristic D, G and G' bands [100,101]. The first intermediate state is studied after 10 minutes of dispersion in an ultrasound bath as illustrated in Figure IV-5b. In comparison with the initial state, an increment in the intensity of the D and G' bands is noticeable, demonstrating, to some extent, the rise in the amount of defects. This is an expected result due to the aforementioned issues related to ultrasonic dispersion, however, it must be avoided, since defects in CNTs act as nucleation sites for fracture propagation [103].

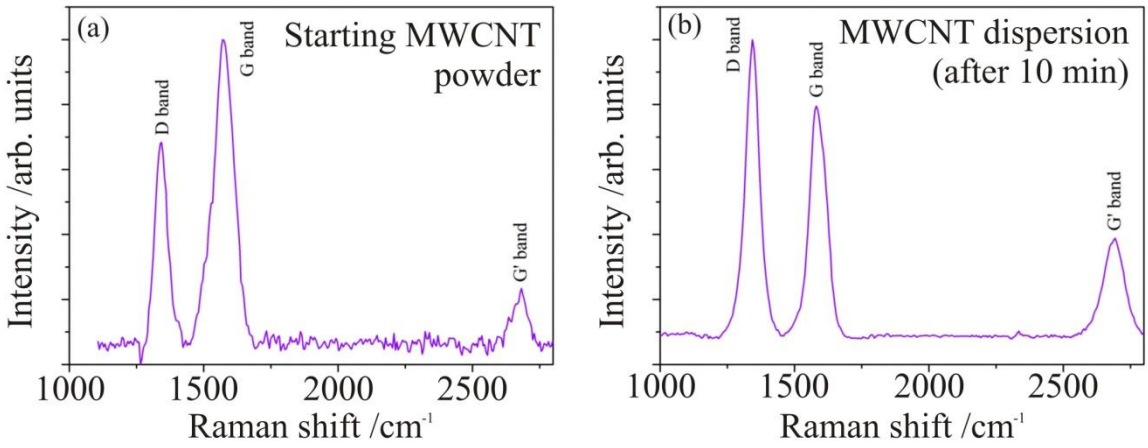

Figure IV-5 – Raman spectra of: (a) Starting MWCNT agglomerates and (b) MWCNT dispersion after 10 minutes of ultrasonication. The characteristic D, G and G' bands are identified.

The next step in the structural evaluation is to analyse the evolution of defects and impurities of the CNTs after the sintering process (Figure IV-6). Here, the CNTs are subjected to high temperatures (850 °C) in vacuum and are in direct contact with the matrix.

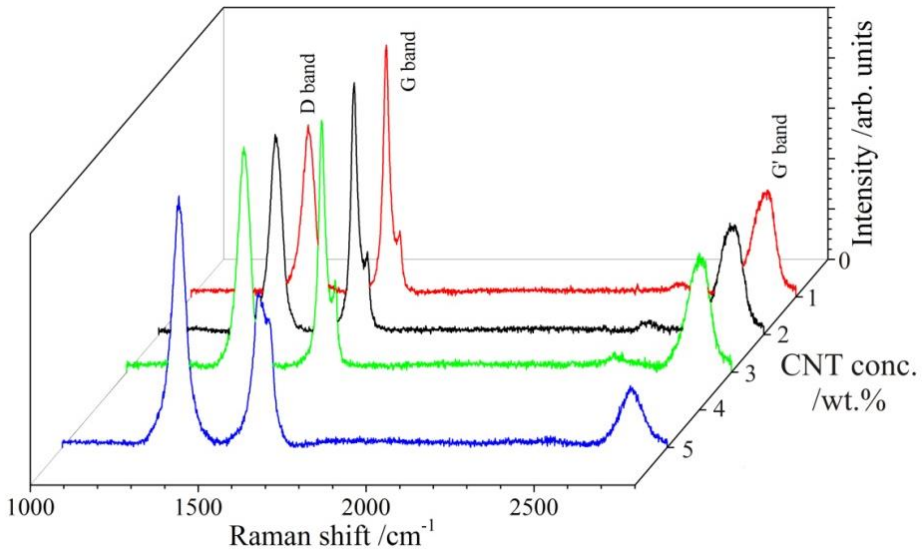

Figure IV-6 – Raman spectra of sintered MWCNT/Ni bulk composites with different MWCNT weight fractions. The characteristic D, G and G' bands are identified.

The first observable peak corresponds to the D band, generated by the presence of defects and impurities (i.e. remaining catalysts, etc.) in the CNT structure [101]. Close to 1600 cm^{-1} the G band is observed, and is attributed to carbons with sp^2 hybridisation. A shoulder positioned towards higher wavenumbers is noticed in all the samples. According to Zhao et al. [104], this splitting of the G band is attributed to the different resonance types of the inner and outermost of the MWCNTs. Finally, the G' band is observed at approximately 2700 cm^{-1}, and corresponds

to an overtone of the defect-related band, but with lower sensitivity than the first order band [101].

DiLeo and co-workers reported that the defect level estimation becomes non-trivial for MWCNTs [100]. The usually studied I_D/I_G ratio, shows a poor correlation to the purity level compared to the $I_{G'}/I_D$ ratio. This ratio is shown to provide the smallest deviation to the average purity values.

Table IV-2 summarises the intensity ratios for the MWCNTs at different stages of the process, including different partial concentrations in the matrix. Comparing the starting agglomerates and ultrasound dispersed MWCNTs, it is observed that the impurity level is similar but the amount of defects is increased. When analysing the composites, the high-MWCNT content samples (5.0 wt.%) show lower purity and a greater amount of defects compared to the samples with lower MWCNT content.

Table IV-2 - Raman intensity ratios and full width at half maximum of the G band for the different stages of the processing.

Sample	I_D/I_G	$I_{G'}/I_D$	Γ_G [cm^{-1}]
Starting powder	0.68	0.34	89.7
10 min US dispersion	1.29	0.34	66.9
MWCNT/Ni HUP 1.0 wt%	0.68	0.62	25.3
MWCNT/Ni HUP 2.0 wt%	0.79	0.54	28.8
MWCNT/Ni HUP 3.0 wt%	0.89	0.52	25.3
MWCNT/Ni HUP 5.0 wt%	1.61	0.24	60.7

Interestingly, between the starting MWCNTs and the 1 wt% sample there is no difference in the defect state of the samples but the purity is increased for the composite. This may be due to the burning or removal of impurities during the sintering process. In the case of the 5 wt% samples, even though all the intensity ratios described in Table IV-2 show a deterioration compared to those of the dispersed state, the MWCNTs remain as such, showing all the characteristic bands.

Another interesting morphological parameter that could be analysed with Raman spectroscopy is the crystallinity. The crystallinity of a graphitic structure can be qualitatively assessed by analysing the full width at half maximum (Γ) of the G band (Figure IV-7). The analysis is based on the uncertainty principle.

$$\Delta E . \Delta t \geq \frac{\hbar}{2} \qquad \text{(Equation IV.2)}$$

Considering the graphitic lattice as a harmonic resonator, the attenuation half-time could be correlated to the amount of defects present in the lattice. That means, the higher the attenuation half-time, the lower the amount of defects. Then, from equation IV.2 it can be concluded that when the energy difference is large, the time period is shorter, representing a highly defective structure. Relating it to a Raman spectrum where the Raman shift represents an energy difference, obtaining thinner peaks would represent a higher crystallinity of the CNT. Such Raman peak features are shown in Figure IV-7.

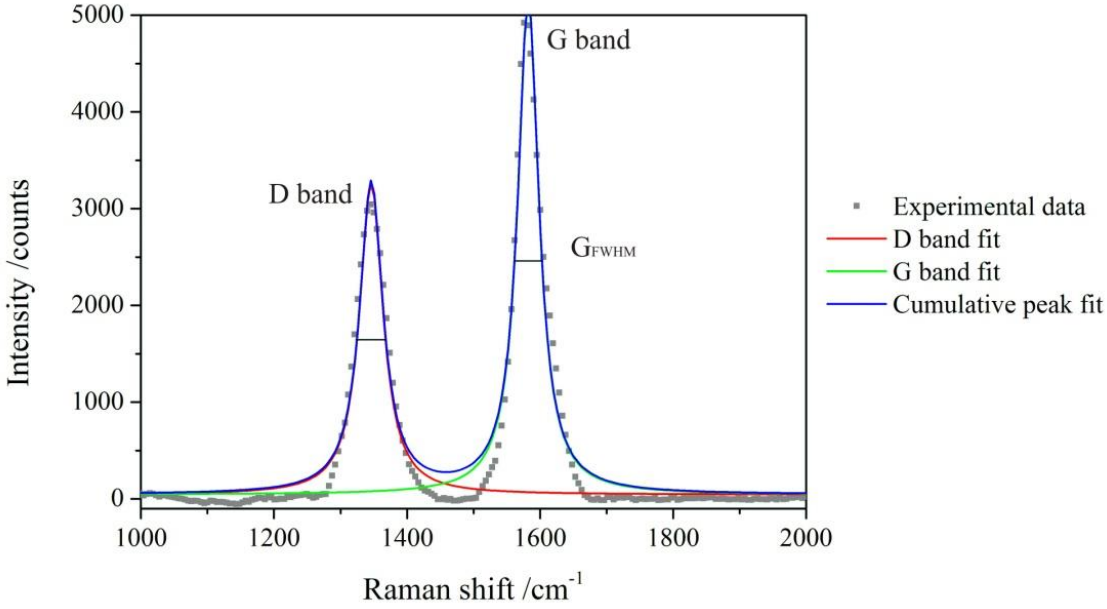

Figure IV-7 – Example of a typical Raman spectrum of MWCNTs. The FWHM of the G band indicates the qualitative crystallinity of the sample.

The peak widths (Γ) are shown in Table IV-2. Comparing the dispersed colloid to the initial state, there is a reduction in the peak width. This might be due to the debundling of the MWCNTs instead of an improvement in crystallinity, which allows them to resonate more freely. Comparing the sintered samples to the dispersed state, there is a significant improvement after processing up to the 3 wt.% sample. As the MWCNTs are better dispersed throughout the matrix, it would be simpler to correct defects by annealing at the process temperature, whereas for the 5 wt% sample, no evident improvement is observed. Considering the partial volume fraction for this concentration (about 26%), a strong reagglomeration of the MWCNTs in the matrix and a poor resonant response are expected.

IV.2.3. Nickel carbide formation and interfacial characterisation

The C-Ni system consists of a simple eutectic with a limited solubility of C in Ni. The maximum solubility of graphitic C in fcc Ni is 2.7 at.%C (0.56 wt.%) at 1600 K [105]. The existence of a carbide (Ni_3C) is predicted at approximately 25 at.%C (4.7 wt.%) as shown in Figure IV-8.

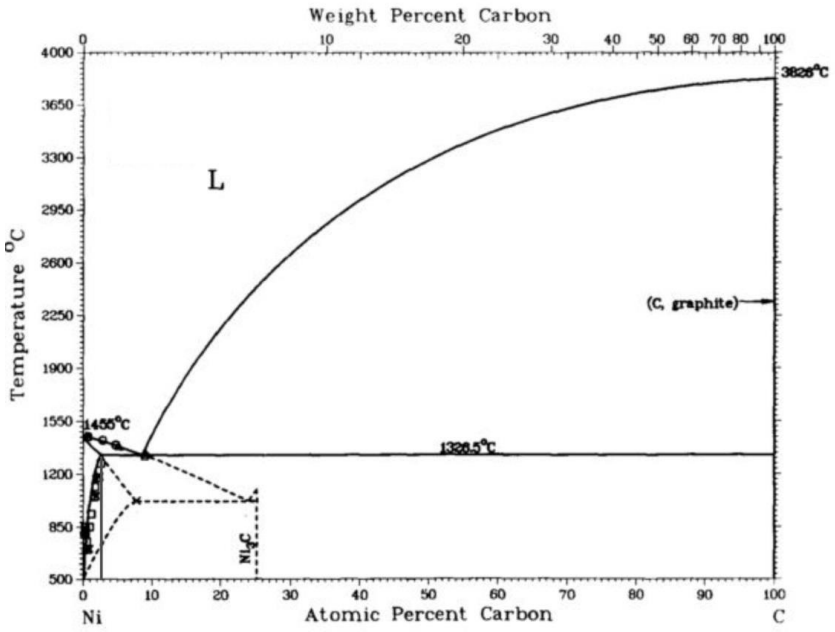

Figure IV-8 – Ni-C (graphite) phase diagram [105].

Thermodynamic simulations were performed with the Thermo-Calc™ software based on the CALPHAD method (Calculations of phase diagrams) [106]. Calculations were made for a Ni-C system with three different C weight fractions (1.0, 2.0 and 5.0 wt.%) for a range from room temperature to 1600 °C. The simulations were based on the thermodynamic SSOL5 database [107]. The simulation results for different partial carbon concentrations (Figure IV-9) show a positive Gibbs free energy of carbide formation from room temperature to above the Ni melting point, thus demonstrating the metastability of the phase.

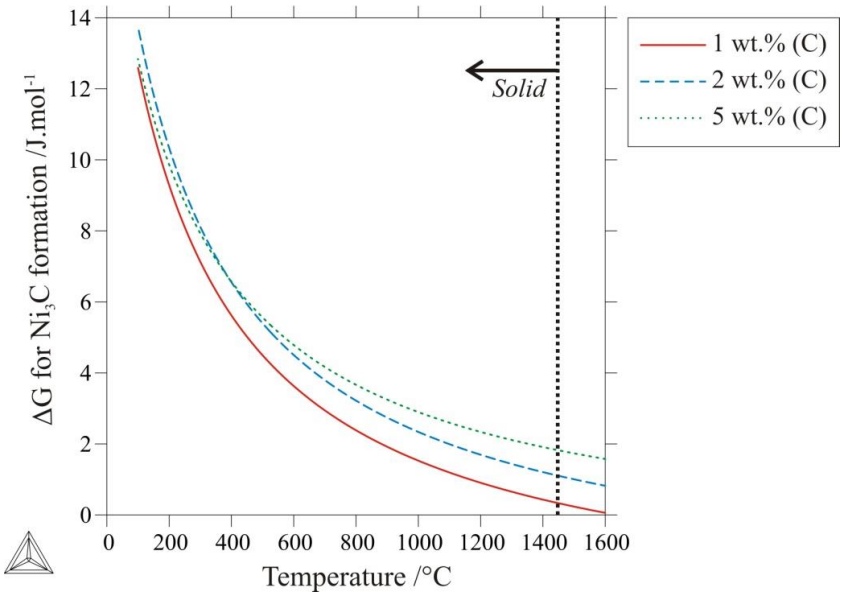

Figure IV-9 – Gibbs free energy plots for the formation of Ni_3C. The curves are simulated for three different weight fractions of C (1.0, 2.0 and 5.0 wt.%).

The formation of Ni_3C has been thoroughly studied in the literature. Particularly, the reactivity in the MWCNT/Ni system has been analysed and the stabilisation of the Ni_3C phase was achieved up to crystal sizes of 20 nm [96]. This phase is usually detected when non-equilibrium synthesis processes such as energetic ball milling are employed [97]. It is believed that Ni_3C is formed by the diffusion of C atoms from the CNT towards the initial face-centred cubic (fcc) Ni lattice [96], generating an allotropic shift towards a Ni_3C hexagonal close-packed (hcp) phase. Furthermore, after this modification, the remaining Ni cells can be stabilised into an atypical hcp Ni lattice. Thus, from a crystallographic point of view, the hcp lattice would be an indicator of a metastable phase existence. Moreover, since there are no reliable diffraction patterns available comprising the nickel carbide phase, it could be useful to analyse the Ni itself and its crystallographic status throughout the sintering process. In that sense, the acquisition of the diffraction patterns of the MWCNT/Ni system at different temperatures is a useful tool for the identification and monitoring of the presence of Ni_3C. Figure IV-10 shows the phase evolution for different temperatures. The selected example represents the highest partial carbon concentration in the samples (approx. 26.5 vol.%), which would be more favourable for the Ni-C reaction.

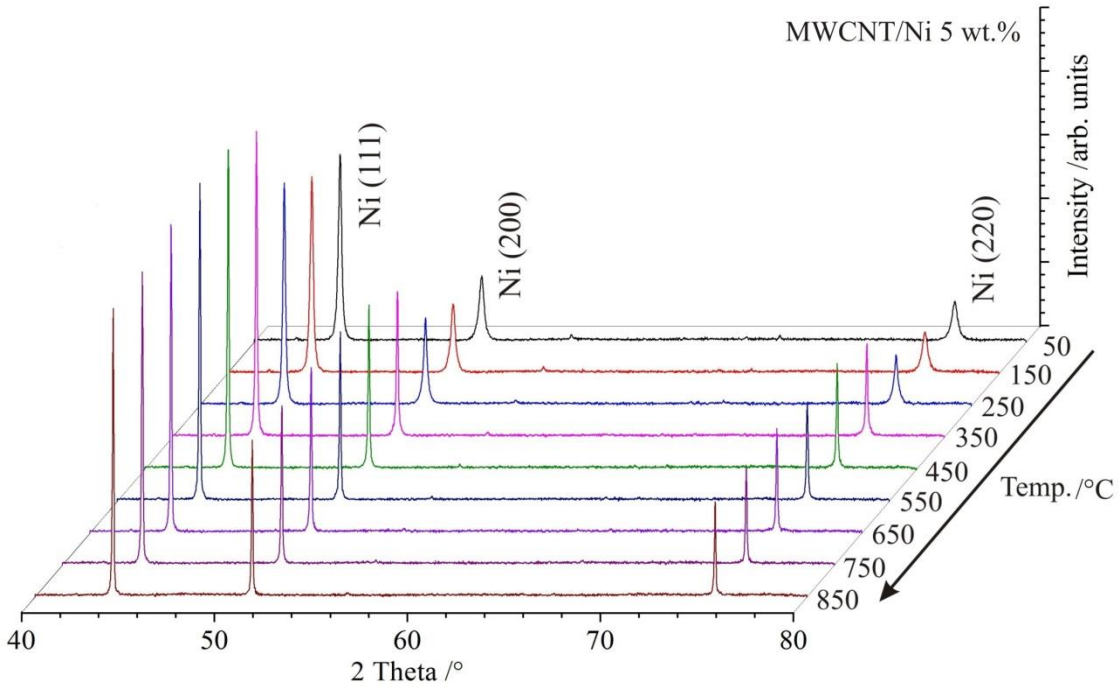

Figure IV-10 – HT-XRD spectra for the MWCNT/Ni 5wt% subjected to a temperature range from 50 to 850 °C. The observed (111), (200) and (220) reflections are typical of fcc Ni.

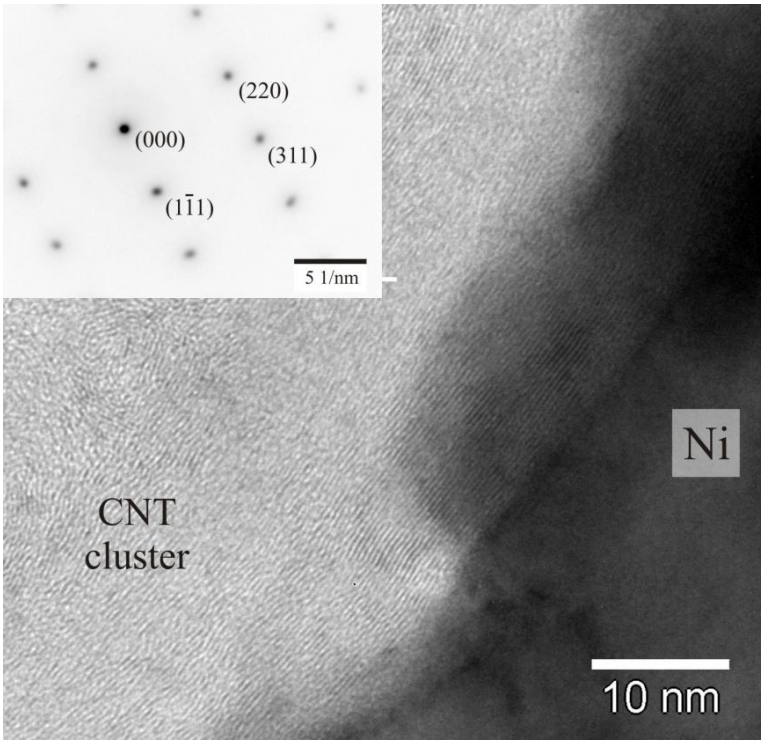

Figure IV-11 – HRTEM of the interface between the Ni matrix and a MWCNT cluster. The interface is clearly noticeable. The inset is a SAED pattern of the Ni matrix, showing a face-centred cubic structure.

Three of the Ni fcc reflections are observable in the scanned range, whereas neither carbide nor hcp Ni diffraction peaks are detected. This indicates that the nanotube dangling bonds did not

react with the nickel by forming end-contact or side-contact carbides. HRTEM was performed so as to study the interface between a cluster of MWCNT and the Ni matrix (Figure IV-11). The interface is clearly defined and no diffusion or phase formation is observable. Selected area electron diffraction (SAED) of the adjacent Ni grain further confirms the presence of a face centred cubic Ni phase.

Hence, it can be stated that no CNT degradation or carbide formation is expected even for high MWCNT/Ni ratios. Thus, one could take advantage of the outstanding physical properties by coherently integrating them into a matrix without modifying the MWCNTs morphology. Moreover, although no functionalisation is carried out for the dispersion and integration of the MWCNTs to the composite, they present a uniform and seamless interface with the metal.

IV.3. Summary

A straightforward processing method for producing MWCNT/Ni blends as precursors for powder metallurgy bulks is presented. The optimal dispersion time was set to 10 minutes, after a morphological assessment of the MWCNT throughout the processing. Additionally, it was seen that after solvent evaporation, a coating of Ni dendritic powders with dispersed MWCNTs was achieved.

The structural stability of the MWCNTs after the processing was confirmed by spectroscopic means, showing that up to a partial MWCNT concentration of 3.0 wt.% (17.5 vol.%), they are structurally improved probably due to a thermal annealing during the sintering process. Despite the fact that the highest studied concentration (5.0 wt.%) shows Raman intensity ratios that are indeed lower than those of the dispersed state, the MWCNTs remain as such, showing all the characteristic bands.

The chemical structure stability of MWCNTs was confirmed despite pressure, temperature, shortening and dangling bonds generated by sintering and ultrasound. Nickel carbide is not detected and a clear interface between matrix and reinforcement is identified on HRTEM. Moreover, SAED confirmed the cubic nature of the Ni matrix, demonstrating that no dissolution of C occurred during processing.

V. The role of MWCNT in the grain growth: microstructural analysis

V.1. Introduction

The microstructure control plays a fundamental role in the design of a material for a specific application. A widespread technique for microstructural tailoring is the second phase particle pinning [108–110]. Structural composite materials, for instance, rely heavily on the reinforcement to stabilise the grain size at a wide temperature range. When sintering, the grain growth of the matrix is usually characterised by a starting or inflection point at which the activity begins, and then the growth saturates due to Zener pinning [110,111]. This results in grain refinement compared to the unreinforced material, and translates to microstructural tailoring of the composite and its properties. This effect has been previously observed in different biphasic systems. These systems include a wide span of potential pinning phases such as precipitates, compounds, particles and/or fibres. For example, Rios et al. [112] reported the grain boundary pinning produced by Al_6Mn precipitates in an Al alloy during annealing. Humphreys observed the same effect in copper composites reinforced with Al_2O_3 particles [113]. Grain boundary pinning was also identified by the effect of carbides in high performance alloys during thermal treatments [114].

For CNT-reinforced metal matrix composites, the grain refinement strengthening has been identified in several different matrices such as: spark plasma sintered copper [115], liquid-state processed magnesium [116], hot-rolled aluminium [74] and electrodeposited nickel [117]. It was observed that the increment in the relative MWCNT volume represented an improvement in the mechanical properties (hardness and/or yield strength) due to microstructural refinement. Recently, Bakshi et al. studied the influence of the addition of CNTs in the strengthening of Al-based composites [118]. They point out that the interfacial interaction of the CNTs with the matrix plays a fundamental role in the strengthening, up to 10 vol.% of CNTs. Nevertheless, they state that this limit might be pushed up by the development of a proper dispersion within the matrix. Despite all the reports that could be found in the literature, and to the best of our knowledge, there is no information available regarding the influence of the amount and distribution of CNTs in the grain growth and the final microstructure.

This chapter focuses on the study of the grain growth evolution of the MWCNT/Ni composite system produced by a pressureless sintering process. The grain growth evolution was investigated by means of high-temperature x-ray diffraction (HT-XRD) and electron backscattered diffraction (EBSD). The influence of the MWCNTs on the grain growth of the Ni matrix was studied by varying the amount of MWCNTs in the Ni matrix.

V.2. Results and discussion

V.2.1. HT-XRD analysis – growth rates

As showed in Figure V-1a, the following Ni diffraction reflections were detected: 111 (44.505º), 200 (51.844º), 220 (76.366º) [PDF file 04-0850], observing no other additional peaks. All the reflections showed an accentuated peak contraction between 200 and 250 °C (Figure V-1b), which corresponds to the starting point of the grain coalescence in the Ni matrix. This starting point was not significantly influenced by the presence of CNTs.

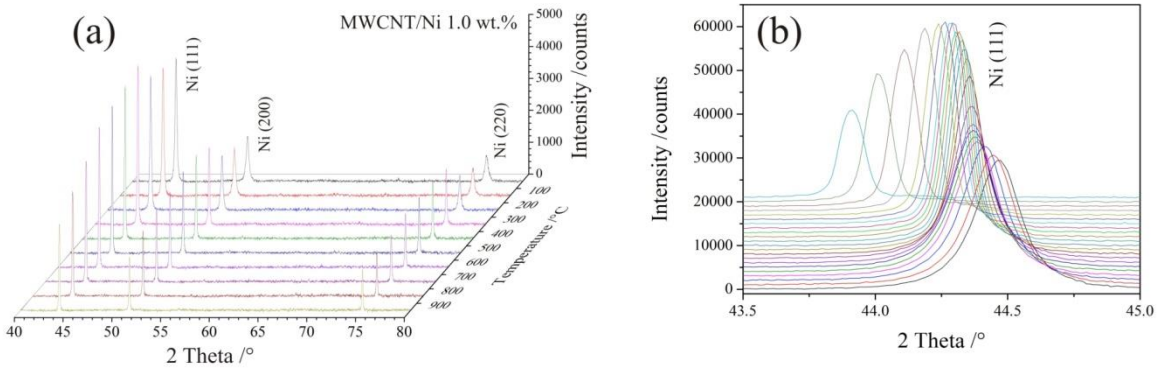

Figure V-1 – (a) Diffractograms of MWCNT/Ni 1.0 wt. % as a function of the temperature (in ° C). (b) Evolution of the Ni (111) peak through the process. A clear contraction of the peak is observed and the shift towards lower angles depicts the thermal expansion of the matrix.

The grain growth was quantified using calculations based on the work published by Thompson and co-workers [119]. They state that the widths of the diffraction peaks contain information about the grain size and strain effects, mathematically described by a Voigt profile, which is the convolution of a Lorentzian (grain size related) and a Gaussian (strain related) peak. A deconvolution of each peak was performed and the grain size at each temperature was calculated using the full width at half maximum (Γ) of the Lorentzian peak in the Scherrer equation (equation V.1).

$$D = \frac{0.9 * \lambda}{\Gamma * \cos\theta} \qquad \text{(Equation V.1)}$$

Another important issue to consider is the existence of a systematic instrumental broadening of the peak, which was extracted from the equipment software and corroborated using LaB_6 powder. This feature limits the capability of the technique to determine the grain size, allowing the calculation of the grain size up to few microns.

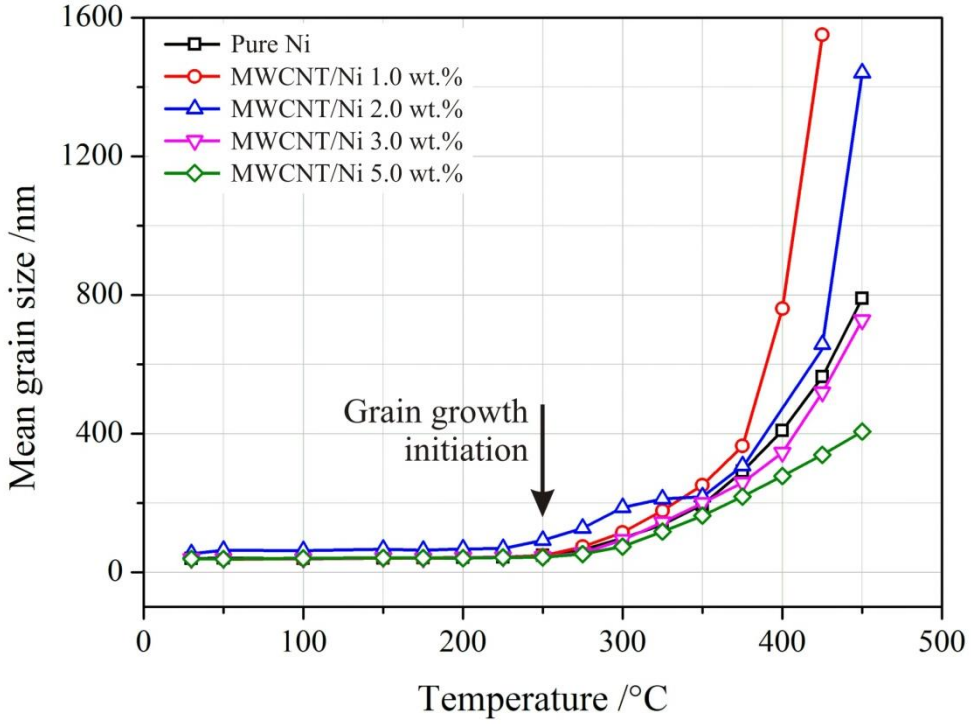

Figure V-2 –Thermal evolution of the grain size estimated from all the observed Ni reflections. The grain size estimation is limited by the instrumental peak broadening in the diffraction patterns.

The mean grain size estimated from all the observed Ni reflections as a function of the temperature in a reduced range (up to the aforementioned detection limit) is shown in Figure V-2. It can be observed that the tendency remains similar for all the samples. During the first stage, the grain growth is not yet activated and can be correlated to the initial stage sintering where grain growth is significantly slow due to the pinning action of the porosity [20]. Pores migrate to grain boundaries and act as mobility barriers reducing total grain boundary area and the surface energy.

Afterwards, a sharp positive slope is observed with the onset temperature starting close to 250 °C, which corresponds to the beginning of the grain coalescence. After this temperature, once the grain growth is activated, it evolves at different rates for each sample. Past this inflection point in the curves, begins a competition between the pinning and thermal conductivity energies. Considering the grain growth in Ni as the reference, the grains in the 1.0 and 2.0 wt.% samples grow at a faster rate, whereas the 3.0 and 5.0 wt.% samples are slightly slower. The

increase in the growth rate has already been reported for CNT-containing composites produced via powder metallurgy [120]. It is well established that grain growth is a specifically thermally-driven process [18]. The growth acceleration is a direct consequence of the high thermal conductivity of the CNTs (where the thermal energy is preferentially transported), generating a local temperature increase, thus favouring grain growth [120]. In the case of this study, the grains of the 1.0 and 2.0 wt.% samples grow faster due to a combination of a lower amount of agglomerates and porosity, which results in higher thermal conductivity. In the case of the 3.0 and 5.0 wt.% samples, significantly more agglomeration and porosity is observed, decreasing the overall thermal conductivity and, as a consequence, the growth rate. Figure V-3 shows the polished surfaces of the different samples. The increment in the agglomeration related to the CNT concentration is observable, reaching tens of microns in certain spots of the 3.0 and 5.0 wt. %. For the 1.0 and 2.0 wt. % the clustering is always in the micron to submicron range.

Yamanaka and co-workers explained the densification difficulties with pressureless sintering of CNT-reinforced composites [82]. They state that the densification is severely hindered by the presence of CNTs with concentrations above 10 vol. % (approx. 2 wt.%). Reagglomeration into clusters is observed and these are believed to obstruct the densification, interposing themselves between Ni particles. Since sintering is a mass transport phenomenon, the porosity closure will bring together the CNT facilitating their reagglomeration. For lower concentrations (up to 10 vol. %), grain growth inhibition is seen and ascribed to a stagnation of the grain boundary mobility generated by the CNTs. The same limit was observed for MWCNT/Ag bulk composites, densified by pressureless sintering [121]. Above this concentration, reagglomeration occurs, reducing the hardness and electrical conductivity of the composites.

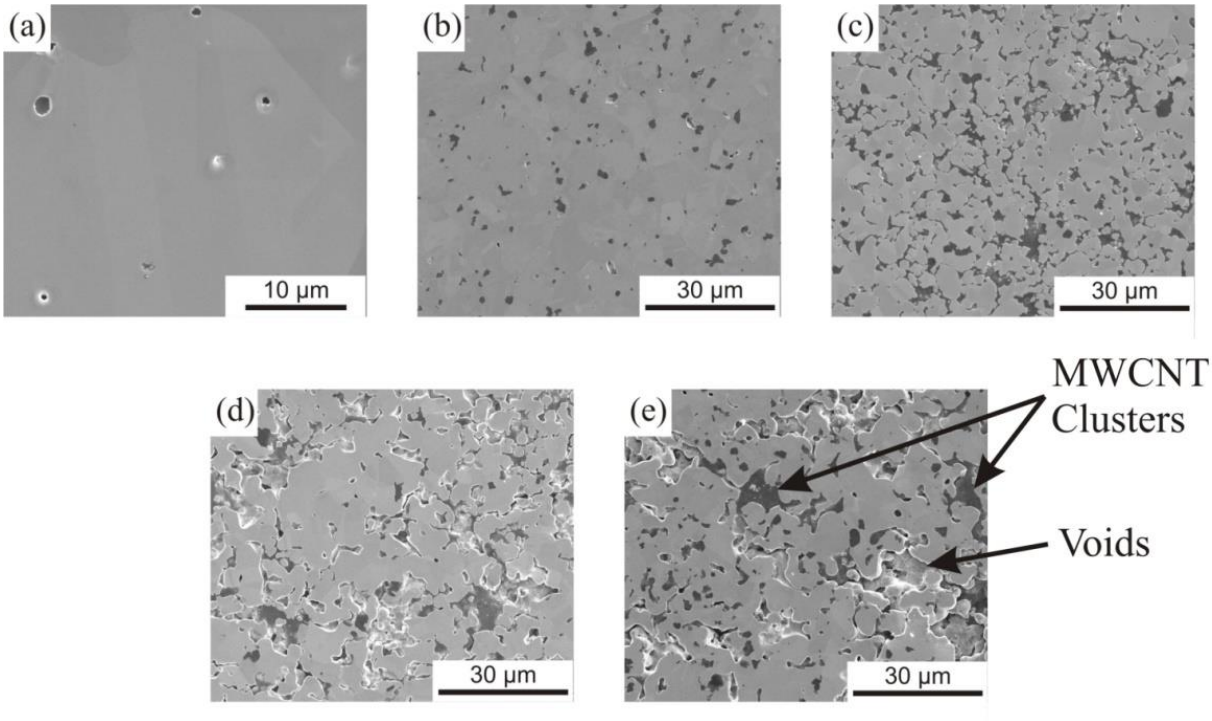

Figure V-3 –SEM micrographs of the samples. (a) Pure Ni, (b) MWCNT/Ni 1.0 wt.%, (c) MWCNT/Ni 2.0 wt.%, (d) MWCNT/Ni 3.0 wt.%, and (e) MWCNT/Ni 5.0 wt.%. The increase in the reagglomeration activity as well as the void formation is noticeable. The dark spots correspond to the reagglomerated CNTs and the regions with bright edges are the voids.

V.2.2. EBSD analysis – microstructural final state

The grain size distribution was determined by means of EBSD after sintering. Figure V-4 shows (500 x 500) μm^2 grain size maps of pure Ni, and MWCNT/Ni 1.0, 2.0, 3.0 and 5.0 wt.%. The parameters and procedures for data acquisition and processing were identical. The white zones within the Ni grains correspond to low-EBSD signal regions, which could be either due to porosity or voids in which the CNT fillers are located. As the percentage of CNT increases, the Ni grain size decreases and the void fraction increases. These voids generate free surface, which may also modify the grain growth kinetics [122]. Indeed, this effect can be observed in the grain size distributions estimated from the EBSD data and presented in Figure V-5. The resulting mean grain sizes are summarised in Table V-1.

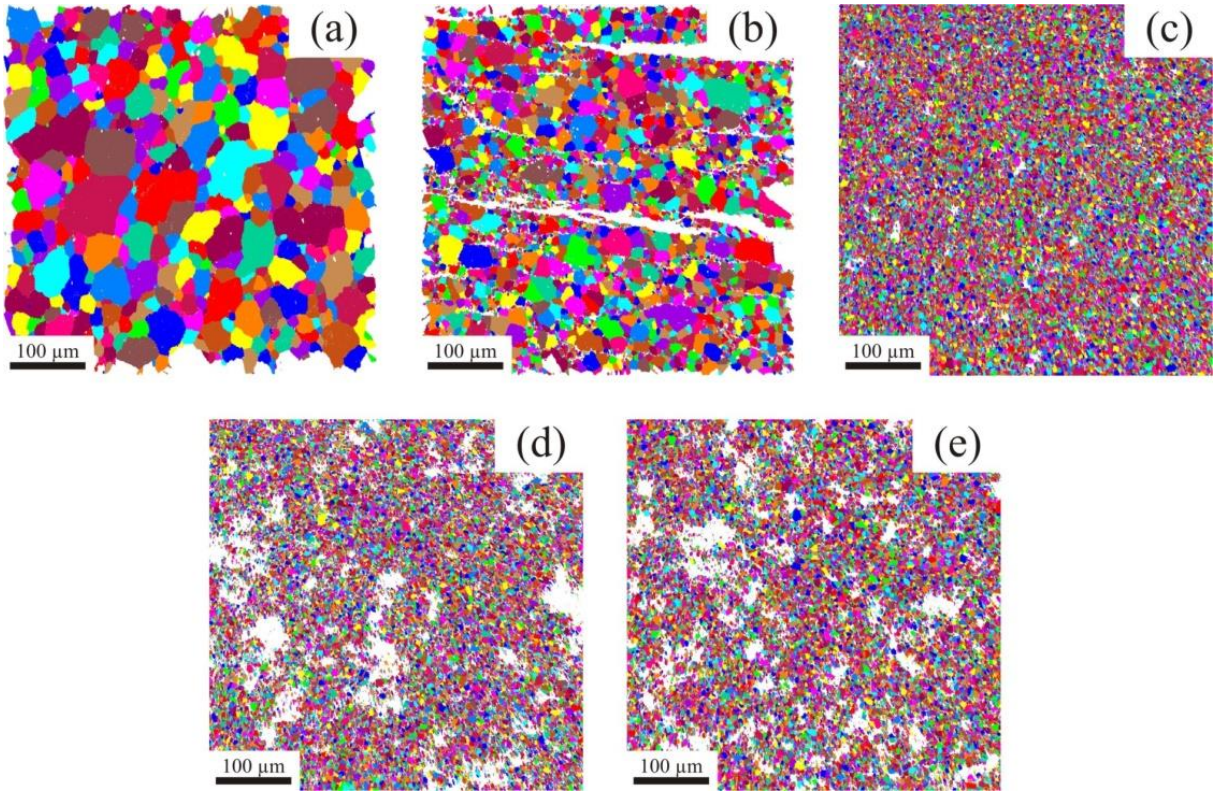

Figure V-4 – Grain size maps obtained by EBSD for the sintered samples. (a) Pure Ni, (b) MWCNT/Ni 1.0 wt.%, (c) MWCNT/Ni 2.0 wt.%, (d) MWCNT/Ni 3.0 wt.%, and (e) MWCNT/Ni 5.0 wt.%

The equivalent diameter of a circumference having the same measured area as the grain was chosen to calculate the grain size distribution (Figure V-5). The diameter distribution for the CNT-containing composites as well as the pure Ni resembles a Log-Normal distribution, in agreement to what is reported in the literature [123].

In the case of pure Ni, a broad diameter distribution can be observed with the highest count at around 50 µm. The final grain size is considerably reduced by increasing the CNT-fraction in the composite. The 1.0 wt. % sample peaks between 10 and 20 µm. The large grain sizes observed for pure Ni and 1.0 wt. % indicate abnormal grain growth. For 2.0, 3.0 and 5.0 wt.% a narrowed and even distribution is observed between 1 and 10 µm. Moreover, no significant change in the final size is observed for the 5.0 wt.% sample compared to the 2.0 and 3.0 %. This fact is directly related to the reagglomeration of CNTs, which can be observed in Figure V-3. The 5.0 wt. % corresponds to almost 26.5 vol.%, which reduces the distance between the MWCNTs and thus increases the probability of their reagglomeration.

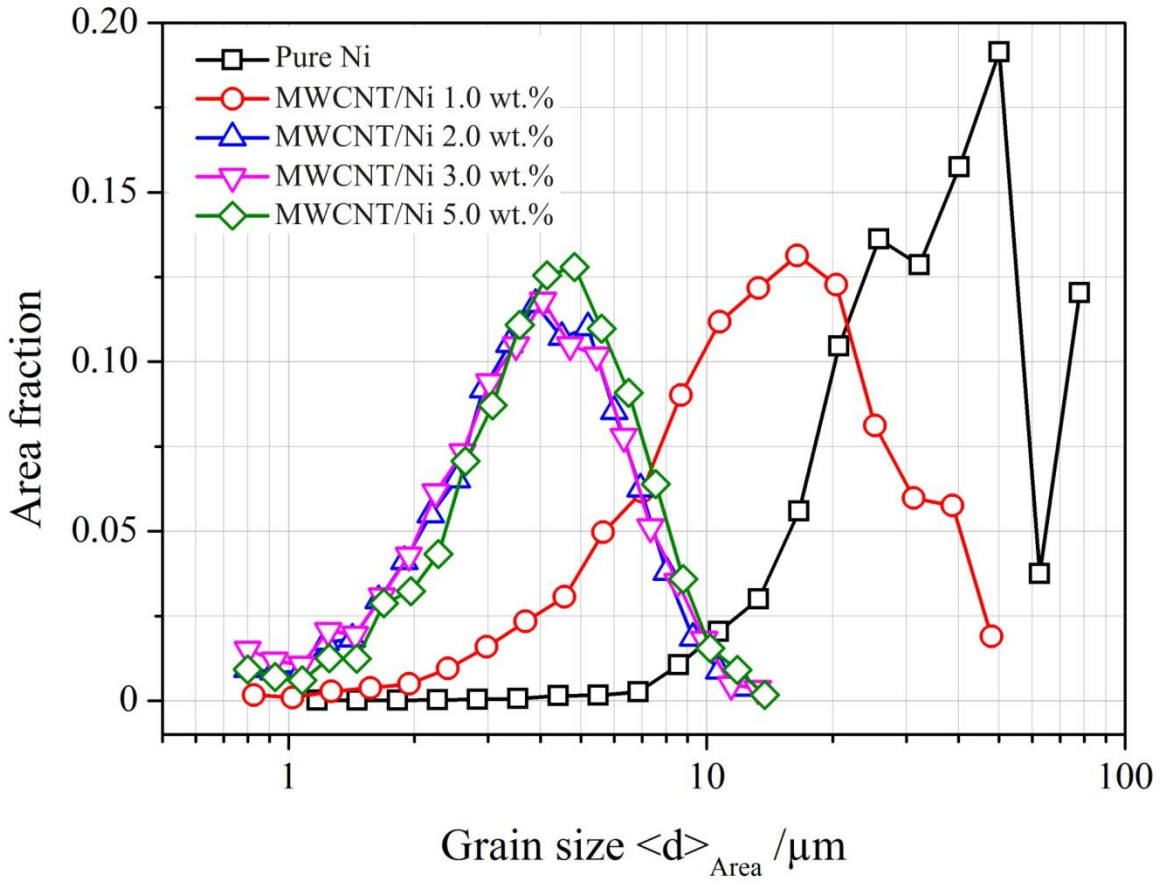

Figure V-5 – Grain size distributions of the sintered samples obtained from the EBSD maps. The grain size is significantly reduced for samples with concentrations above 2.0 wt. %

Table V-1 - Mean grain sizes of the composites after the sintering process. The values were obtained by EBSD.

Sample	MWCNT vol. %	Final mean grain size [µm]
Pure Ni	---	47.55 ± 3.06
MWCNT/Ni 1.0 wt.%	6.5	22.39 ± 0.97
MWCNT/Ni 2.0 wt.%	12.3	4.93 ± 0.13
MWCNT/Ni 3.0 wt.%	17.5	4.94 ± 0.13
MWCNT/Ni 5.0 wt.%	26.5	5.27 ± 0.10

If Zener pinning is taken into account, the resulting mean grain size is modelled with the following equation [124]:

$$D = \frac{k*r}{f^n} \qquad \text{(Equation V.2)}$$

The term k is a proportional dimensionless constant, f is the volume fraction of the second phase and r is the mean reinforcement radius. Grain growth stagnation ensues from the restriction of grain boundary mobility caused by friction with a dispersion of second phase particles (in our

case the CNTs) [108]. As seen in Equation V.2, the refinement effect is proportional to the size of the fillers. Therefore, by increasing the amount of agglomerates, the effective size of the reinforcements is increased and the drag force is reduced proportionally resulting in larger final grain sizes. Another important requirement for the microstructural refinement is the interparticle distance distribution [110]. The interface energy absorption is inversely proportional to the distance between particles. With higher amount of CNTs the interparticle distance is statistically lower. However, if reagglomeration increases, so does the expected interparticle distance, thus reducing the refinement effect on the microstructure. Thus, one could say that between 2.0 and 3.0 wt%, the CNT concentration no longer reduces the grain size. This fact fixes, to some extent, an empirical limit for the grain size control of the composites beyond which no significant additional influence is noticed. Furthermore, this reinforcing limit was also determined by Pham and co-workers at 3 wt% (approximately 17.5 vol.%)[125], for powder metallurgical CNT/Cu composites. For aluminium-based composites it was settled in a range between 3 and 5 vol.% [74].

V.3. Summary

The grain growth evolution was determined by means of HTXRD. It was found that the onset temperature is not influenced by the presence of CNTs, whereas their kinetics are indeed controlled by the amount of CNTs. In this sense, grain coalescence was found to start approximately at 250 °C. Growth stagnation is observed in all the composites, mainly induced by the dispersion within the matrix material. The dispersion plays a fundamental role in two main aspects: enhanced thermal transport which affects the growth kinetics and proper Zener pinning by reduced interparticle distance. It was observed that, for lower MWCNT concentrations, the growth is driven mainly by a thermal conductivity-related effect, whereas for the higher concentrations (3.0 and 5.0 wt.%), the growth is governed by Zener grain boundary drag. Moreover, under these experimental conditions (pressureless sintering), an empirical reinforcing limit can be set between 2.0 and 3.0 wt.%, after which no further microstructural refinement can be achieved. This limit is followed by strong CNT reagglomeration during the mass transport in sintering. Concluding, based on the presented results, it can be stated that the presence of properly dispersed CNTs in the composite is a powerful tool to tailor the grain growth and thus the physical properties of the composite.

VI. Thermomechanical behaviour: bulk dilatometry and lattice behaviour

VI.1. Introduction

As described in the theoretical section (Chapter II.3), CNTs possess outstanding physical properties which make them suitable candidates as reinforcing phases in composites. Particularly, it has been predicted that they could have very low or even negative intrinsic thermal expansion [126,127], making them the ultimate reinforcement fibres for a wide range of composites subjected to thermal cycling. The question would be how this property could be fully utilised in different materials. The hypothesis is that once an optimal dispersion of the CNT bundles and a proper integration into the matrix is achieved, the mechanical properties of the material would be improved by the increased matrix-reinforcement interfacial coherence. Thus the CNTs would act as anchoring points, preventing the expansion of the composite. However, despite the fact that the anchoring effect is mentioned in countless reports, no empirical demonstration has been provided.

As it has been reported, CNTs can actually have a negative coefficient of thermal expansion (CTE) with a minimum at 800 K [128]. These negative expansion modes are due to a gain in structural and vibrational entropy, translating into a dimensional decrease [128]. Thus the inclusion of MWCNTs into metallic matrices is expected to increase the span of application fields by improving their thermomechanical performance. Several authors [129–131] have developed studies on the thermal expansion behaviour of certain alloys and materials, yet no attention has been paid to MWCNT/Ni composites.

The aim of the work in this chapter was to achieve bulk metal matrix composites possessing remarkable thermal expansion behaviour. The samples were densified by pressureless sintering and hot uniaxial pressing both under vacuum. Thermomechanical (dilatometry) measurements were carried out on the samples under an inert gas atmosphere. Microstructural characterisation was made using x-ray diffraction (XRD) and focused ion beam/ scanning electron microscopy (FIB/SEM). Furthermore, since there is no definitive explanation in the literature for the so-called “anchoring effect”, the lattice thermal expansion behaviour of the matrix lattice was analysed in order to understand the influence of CNTs on the thermomechanical properties. The

lattice parameters were measured by x-ray diffraction (XRD) in a high-temperature (HT) chamber under medium vacuum conditions. These novel results highlight the influence of the CNT distribution throughout the Ni matrix, as well as the CNT-lattice interaction under a thermal input. The obtained knowledge constitutes a basis for a further understanding of the mechanisms acting in the composites under thermal load.

VI.2. Results and Discussion

VI.2.1. Bulk thermal expansion behaviour

The thermo-mechanical measurements showed very interesting results regarding the thermal expansion, particularly in the low temperature (50 – 400 °C) regime. The tested samples presented expansions and densifications which could be attributed to residual matrix-reinforcement stresses [132]. It is noteworthy that up to about 450 °C the lowest thermal expansion was observed for the CPS composites.

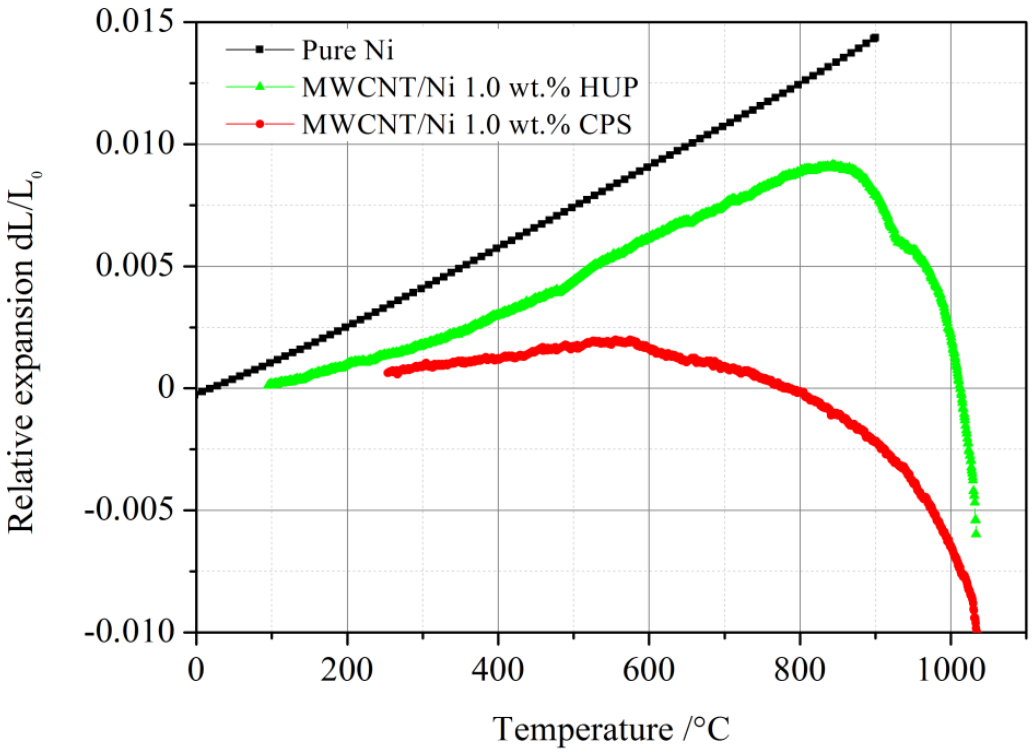

Figure VI-1 – Thermal expansion curves of the samples. As a reference, Ni expansion was plotted from [133].

The on-set densification temperature was observed at about 600 °C. Figure VI-1 shows the relative expansion (dL/L_0) of sintered specimens with 1.0 wt.% of CNTs, with a clear densification bend of the HUP specimen at about 840 °C. During the expansion a break point in the slope at roughly 450°C is observed. The densification on-set might be directly related to the initial state in the solid state sintering [134,135]. Also, another change in the densification

rate at around 930°C is detected. The maxima in the densification rates are around 1050°C or lower, which is about 400°C below the melting point of Ni (0.7 T_m of Ni).

The high densification rates and the low temperatures at which densification takes place suggests a highly pure and active Ni powder with clean (oxide-free) grain surfaces. The expansion coefficients (CTE) at 50-400 °C were $9.1x10^{-6}$ and $3.9x10^{-6}$ 1/°C for HUP and CPS, respectively, a value considerably lower than that of pure Ni ($16.3x10^{-6}$ 1/°C [133]). The lower expansion may be explained by a good fibre-matrix bonding at the high temperature sintering stage. In that case, the lower expansion of the CNTs may exert tensile stress on the matrix [132].

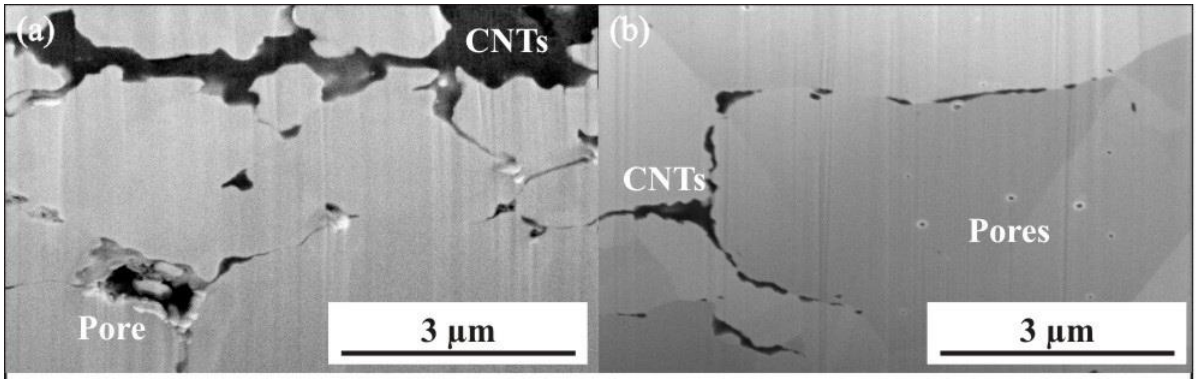

Figure VI-2 – SEM micrographs from FIB cross sections of (a) CPS and (b) HUP composites with 1.0 wt.% CNTs.

Figure VI-2a shows the FIB cross section of the MWCNT/Ni 1.0 wt.% CPS sample, which presents an acceptable densification despite the observed porosity. This sample was about 6% less dense than the pure Ni, as presented in Table VI-1.

Table VI-1 – Density values of the produced samples and their thermal expansion coefficient (CTE).

Sample	Rel. Density [%]	CTE [$x10^{-6}$ 1/°C]	R^2	CTE %
Pure Ni	100	16.3±0.08	0.99891	---
MWCNT/Ni 1.0 wt.% HUP	95.5	9.10±0.04	0.98921	-44.2
MWCNT/Ni 1.0 wt.% CPS	93.7	3.90±0.06	0.94404	-76.1

The porosity situated in the near region of the CNT clusters confirms that the cohesion between Ni and CNT clusters is low. This reagglomeration might be generated in the pressureless sintering stage of the process where the heating ramp is low and the sintering neck formation is delayed, leaving a pathway for the CNTs to bundle. In this type of free densification process, the absence of external dimensional constraints during the treatment permits the existence of voids where the CNTs agglomerate. This is not the only result of a lack of dimensional restriction; reaching full density is complex because the material is free to expand in all

directions. Moreover, it can be noticed that the pore size is in the submicron range. However, for the case of the MWCNT/Ni 1.0 wt.% HUP samples (Figure VI-2b) the pore size is drastically reduced to tens of nanometres. In this case, the clusters size is smaller compared to the CPS sample, and most of them are located at grain borders. This type of distribution might be helpful for the load transfer from the matrix to the reinforcements. Contrary to the CPS process, HUP restricts the sample in the die, allowing only inward diffusion. Based on observations, it can be claimed that the apparent intergranular CNT clustering could be actually a grain interface distribution that was covered by the matrix and could not be differentiated by the FIB cross sections. The large difference between the CNT-containing samples may be mainly due to mass transport during the thermal input. As showed in chapter V, the on-set temperature for growth in these systems is found at about 250 °C (consistent with the results shown in chapter V).

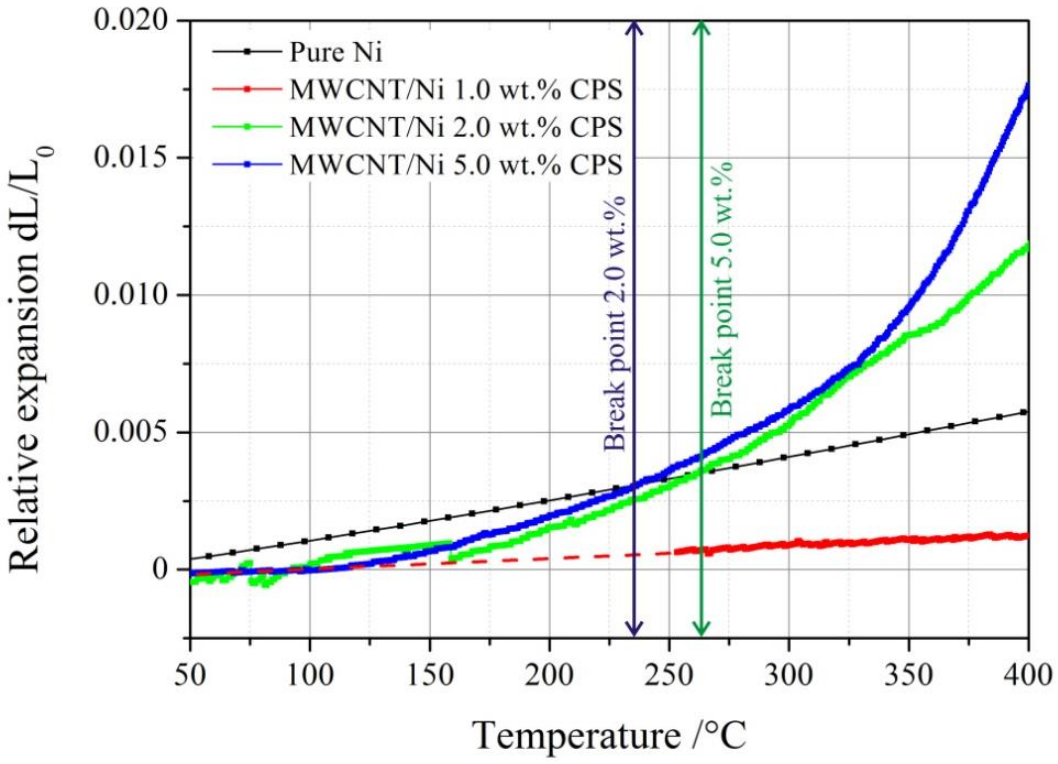

Figure VI-3 – Thermal expansion behaviour of CPS samples with different CNT amounts. The response of the 2.0 and 5.0 wt.% samples show a break point where the expansion of the Ni reference sample is overlapped. This is believed to be due to a detachment of the reinforcements from the matrix.

By focusing only on CPS samples with different CNT concentrations (Figure VI-3), interesting results are obtained. Samples with 1.0 and 2.0 wt.% showed lower CTE than pure Ni, however, the 2.0 wt.% response exceeds the Ni expansion at approximately 235 °C. The 5.0 wt.% sample had a CTE larger than the reference in the whole range.

Table VI-2 presents the CTE values, discriminated in pre and post-intercept (temperature at which a sample expands more than the reference). The hypothesis for the occurrence of this intercept in the expansion response is that the samples presented an internal pressure expansion, usually called "bloating". This bloating effect is typical in materials presenting internal porosity where certain gases (i.e. poorly evaporated solvents, water, etc) are adsorbed during or remain after processing.

Table VI-2 – CTE of the samples manufactured by CPS with different CNT concentrations. The intercept where the expansion of the Ni reference is met is also marked.

Sample	CTE [x10^{-6} 1/°C]		Intercept [°C]
	Pre-intercept	Post-intercept	
Pure Ni	16.30±0.08	-------	-------
MWCNT/Ni 1.0 wt.% CPS	3.90±0.06	-------	-------
MWCNT/Ni 2.0 wt.% CPS	13.70±0.70	57.30±0.30	256.7
MWCNT/Ni 5.0 wt.% CPS	17.30±0.30	82.00±1.00	236.4

After the application of temperature, these gases are desorbed, finding no path to exhaust due to the lack of interconnected porosity. Past a certain temperature (intercept), the internal final pressure (P_f) exceeds the surrounding initial atmospheric pressure (P_i), thus expanding the matrix in excess. A model of this mechanism is depicted in Figure VI-4.

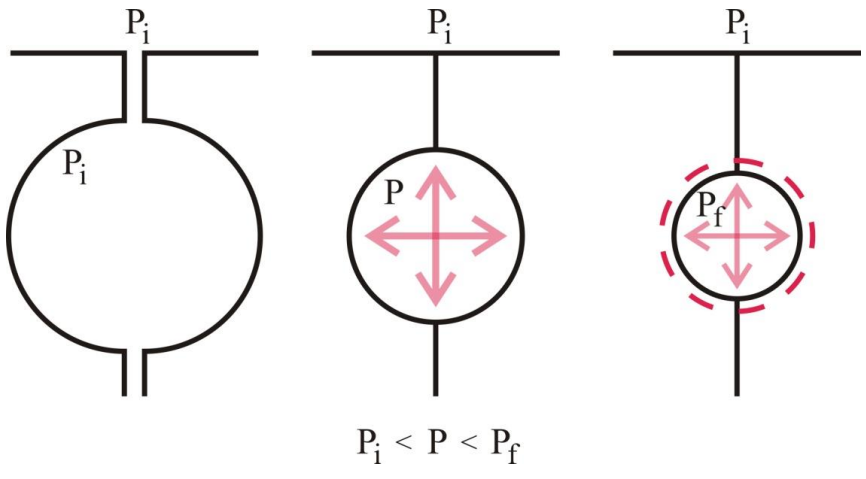

Figure VI-4 – Porosity closure diagram and bloating due to internal gas pressure in sintered samples. Adapted from [18].

VI.2.2. Ni lattice thermal expansion – HTXRD analysis and models

The SEM micrographs in Figure VI-5 reveal the integration of the MWCNTs in the Ni matrix. In the pure Ni samples, a small number of pores and grain boundaries can be seen. This amount of porosity is normal and is mainly due to the manufacturing technique. The final densities of the studied composites are around 94-96%.

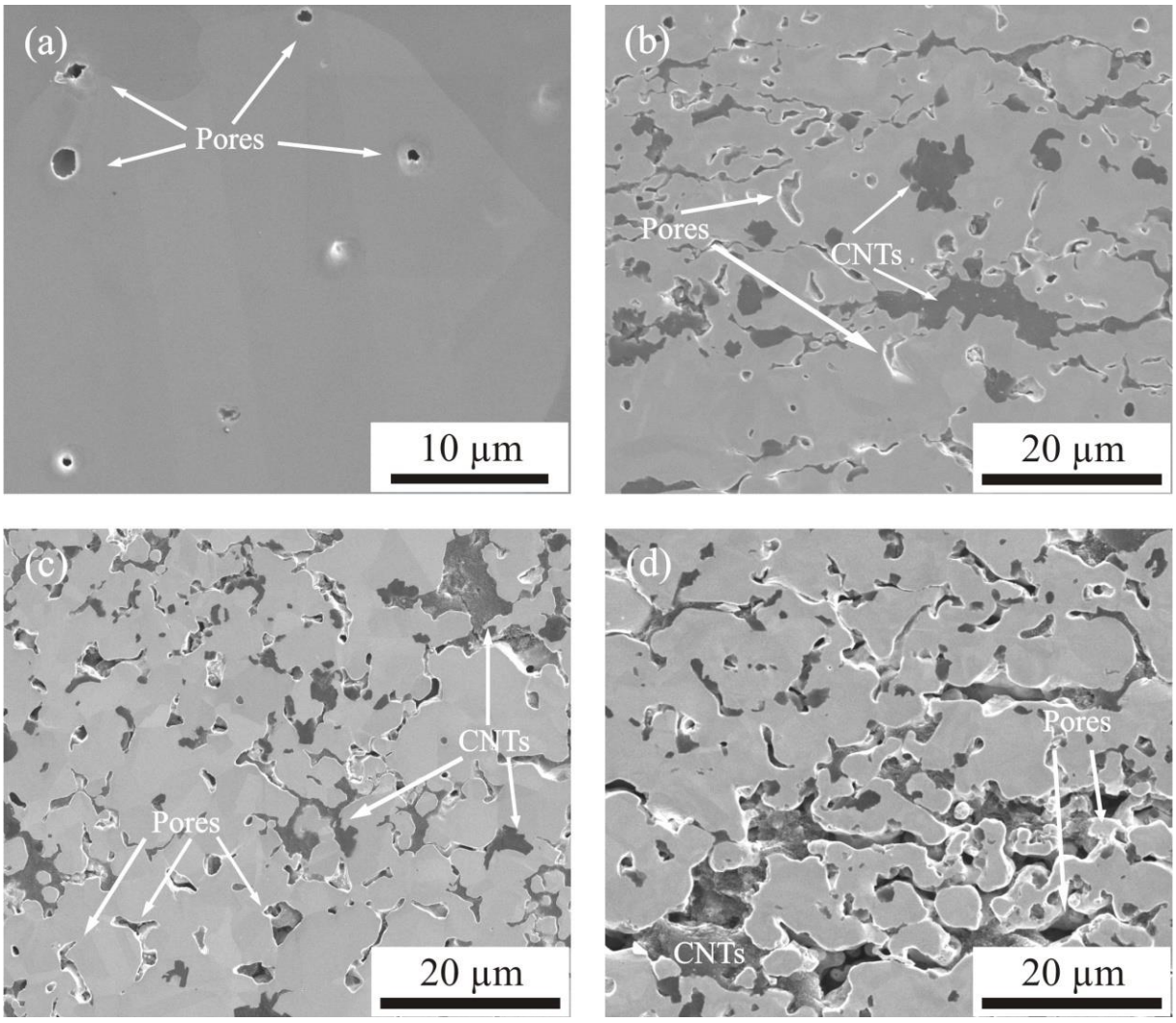

Figure VI-5 - SEM micrographs of (a) pure Ni, and a Ni matrix with (b) 1 %, (c) 3 % and (d) 5 % MWCNTs in weight. The dark grey areas inside the free volumes correspond to CNTs. The gray zones observed in the Ni matrix with different refinements correspond to different grains.

The composite samples present a larger free volume (voids) and MWCNTs at the grain boundaries. Particularly, in the 3.0 and 5.0 wt. % samples, certain pores reveal poor cohesion between the reinforcements and the matrix. As explained before, this is due to a higher degree of agglomeration of the MWCNTs, which further translates into a low adherence between the clusters and the matrix. However, the 1.0 wt. % sample displays a better dispersion and

distribution within the matrix. The reduced amount and size of the clusters improves the adhesion of the MWCNTs to the matrix.

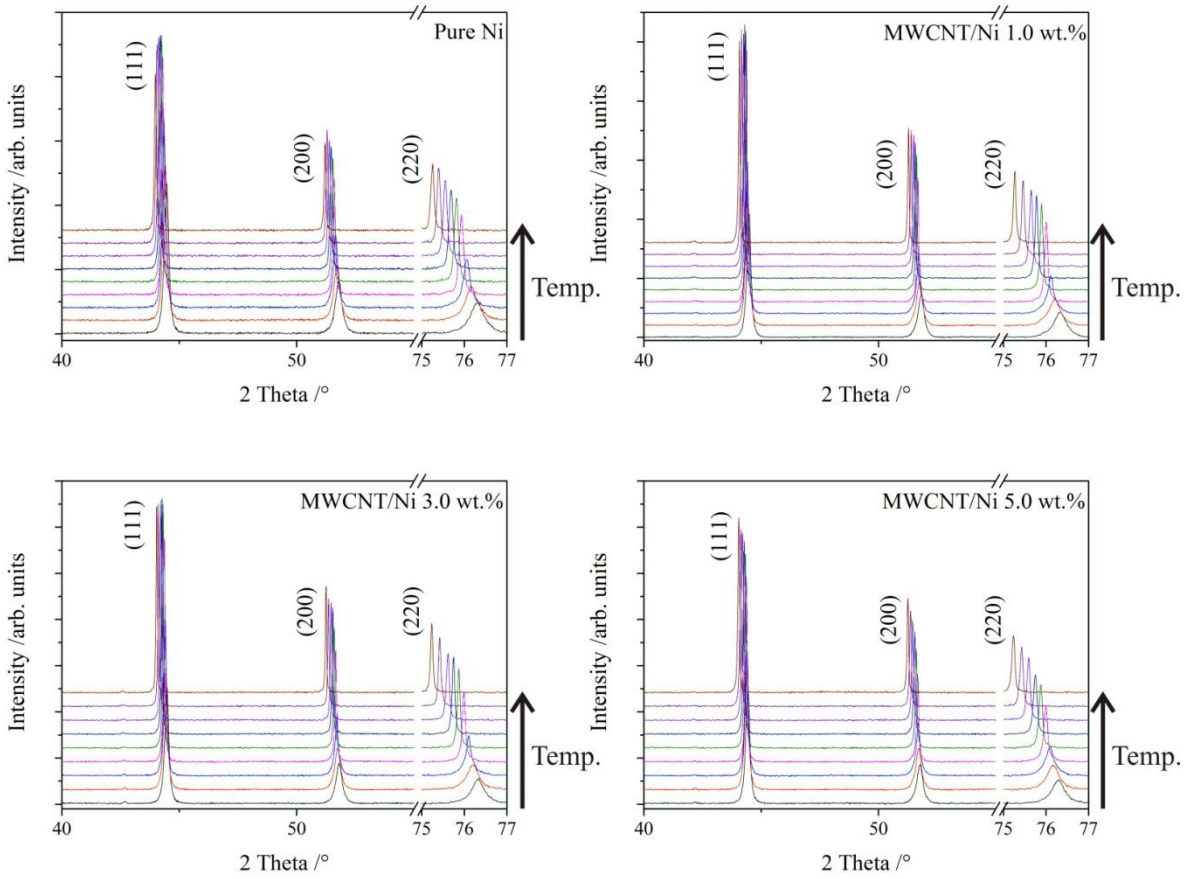

Figure VI-6 - Diffractograms of the tested samples as a function of the temperature (in ° C). The lower curve corresponds to 50°C and the last to 850°C. The measurements were made every 100 °C. The shift of the (111), (200) and (220) Bragg peaks towards lower 2θ angles are due to the expansion of the d-spacing between the corresponding planes.

The (111), (200) and (220) Bragg reflections (Figure VI-6) were observed in all the samples throughout the complete temperature range. In the diffractogram measured at 50º C they were located at 44.51º, 51.84º and 76.37º; respectively. After heating, these peaks shifted towards lower 2θ angles due to the expansion of the d-spacing between the corresponding planes. The MWCNT/Ni samples presented similar behaviour and no other Bragg reflections were observed with the inclusion of the MWCNT into the matrix. The estimated values of the face-centred cubic lattice parameter of Ni as a function of temperature are summarised in Table VI-3. It is worth noting that the Bragg reflections become narrower as the temperature increases mainly due to grain growth and stress relaxation processes. In order to avoid systematic errors from misalignments and thermal expansions of the sample holder, the 2θ scan data were corrected using the Nelson-Riley (NR) approximation [136]. The Nelson-Riley method is an

extrapolation procedure where the systematic error introduced by the eccentricity of the sample with respect to the rotation axis in the diffractometer is corrected. This eccentricity has been found to be proportional to $\cos^2(\theta)$. For the correction, the calculated lattice parameter "a" from the raw data is plotted against $\cos^2(\theta)/\sin(\theta)$, which is a widely used function for cubic systems [137]. The obtained points are later linearly fitted and the intersection with the y-axis provides the corrected lattice parameter, *a*.

Table VI-3 - Ni lattice parameters measured in all MWCNT/Ni samples by HT-XRD and estimated by the NR method.

Temperature [°C]	$a_{corrected}$ [nm]			
	Pure Ni	1.0 wt.%	3.0 wt.%	5.0 wt.%
50	0.3526(1)	0.3526(1)	0.35261(8)	0.3526(1)
150	0.35328(9)	0.3532(1)	0.35321(6)	0.35321(8)
250	0.35376(7)	0.35376(4)	0.35378(2)	0.35381(3)
350	0.354361(5)	0.35437(1)	0.35439(1)	0.35440(2)
450	0.35492(3)	0.35494(3)	0.35497(3)	0.35499(2)
550	0.35551(1)	0.3555(6)	0.35555(3)	0.35561(3)
650	0.35612(1)	0.356(1)	0.35621(4)	0.35634(3)
750	0.35674(2)	0.357(1)	0.35706(4)	0.35711(4)
850	0.35739(2)	0.358(1)	0.35792(5)	0.35796(4)

The lattice thermal expansion corresponds to a temperature-gradient-induced reversible variation of the lattice parameter of a crystal. In the general case, the relationship between the lattice parameter and the temperature can be modelled by polynomial dependence [138]. The first-order temperature term describes a harmonic behaviour, valid for small amplitudes of atomic vibration (< 1%). The second-order term corresponds to the asymmetry of the mutual Coulomb repulsion between atoms. The third-order term corresponds to large amplitudes of atomic vibration that lead to energy dissipation. Non-harmonic behaviours are usually significant at temperatures close to absolute zero or melting points. Since the melting point of Ni is higher than 1400 ºC [139], harmonic first-order behaviour of the lattice expansion was thus assumed.

The lattice parameter estimated by NR was fitted with a linear regression [136]. As presented in Figure VI-7, the curves show a similar behaviour, but differ in their slopes. The CTE is defined as the fractional variation in length per unit temperature change $\alpha = (1/L_0)\cdot\partial L/\partial T$. The

calculated CTE of the pure Ni samples was 16.6(2) x10^{-6} 1/°C, which agrees with the standard powder value [133,140]. The values for the MWCNT/Ni composites were 18.6(7) x 10^{-6} 1/°C (1.0 wt. %), 18.3(5) x 10^{-6} 1/°C (3.0 wt. %) and 18.6(5) x 10^{-6} 1/°C (5.0 wt. %). The composites showed a higher lattice CTE than that of pure Ni by around 12% for the 1.0 wt. % samples, while the increment in amount of MWCNTs did not significantly affect the thermal expansion of the composites.

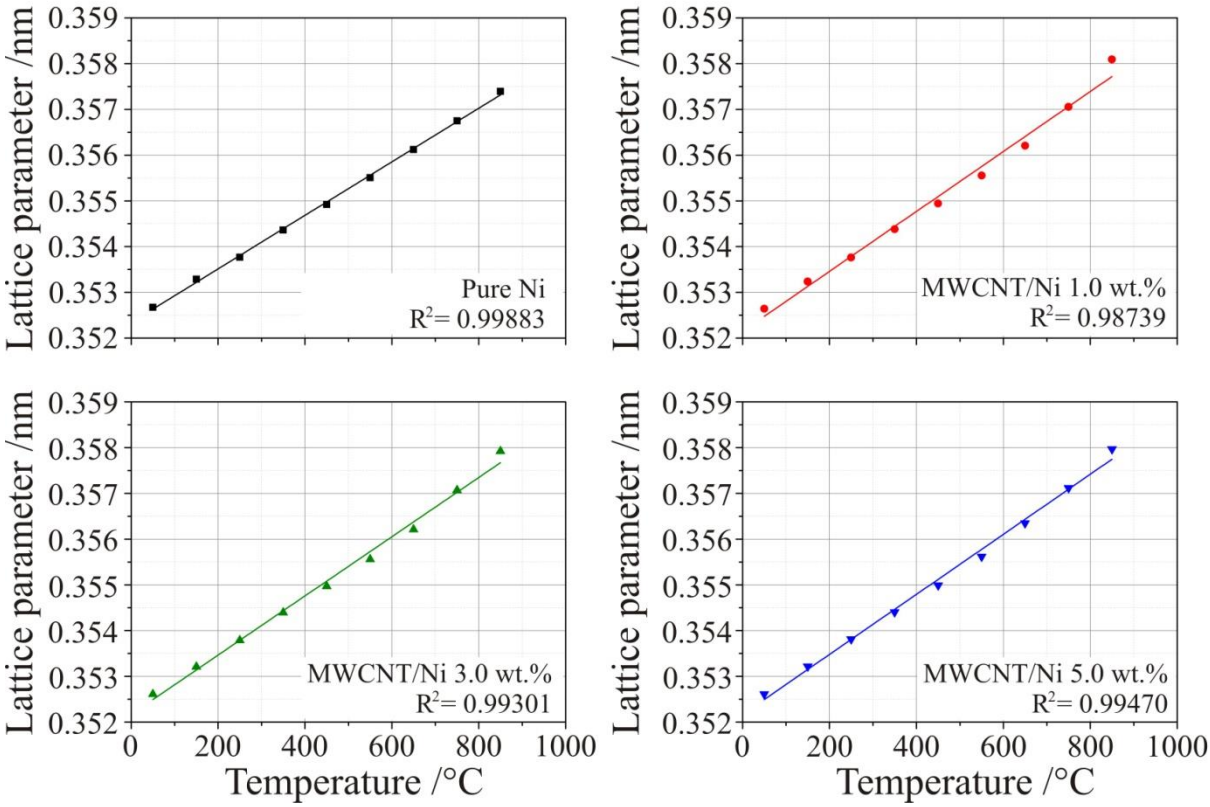

Figure VI-7 - Lattice parameter of the MWCNT/Ni composites estimated from the data shown in Fig. VI-6 using the Nelson-Riley method. Linear regression fitting was performed in order to estimate the thermal coefficient of expansion of the composites as a function of the percentage of MWCNTs added to the Ni matrix. The statistical error of the measurements is lower than the size of the data symbols.

These results disagree with the behaviour of the thermal expansion coefficient reported in the previous sub-chapter measured by differential dilatometry. Regarding this, Roy et al. [141] mention that in materials with a very low CTE, the bulk thermal expansion is usually not necessarily identical to that of a single crystal from which it is composed. Indeed, this anomaly is produced mainly by a compensation effect resulting in an average CTE value. This difference was also observed by Ferrer-Anglada and co-workers in their report on the thermal expansion behaviour of Cu/CNT composites with large partial concentrations (30-55 wt.% Cu) [142]. They measured the thermal expansion of Cu by means of XRD in a narrow temperature range (20-260 °C), observing an increase in the CTE of approximately 7% compared to that of pure

Cu. By analysing the available research on this topic, it was found that the fundamentals of the interaction between the CNTs and the metallic matrix were to some extent not deeply discussed and described. Uddin et al. observed [143] that the addition of MWCNT to Cu and Al reduces the CTE up to 20% compared to that of the pure metals. The explanation given is based on the uniform dispersion and proper embedding of the MWCNT in the metallic matrix, restraining the grains, bridging and pulling the matrix together during the thermal cycling. Another work carried out in this direction [144] reports a reduction of about 65% in the CTE of an SWCNT/Al composite. This decrease is explained by powerful constraints provided by the SWCNT, grasping the matrix material. Deng et al. observed a decrease in the CTE of CNT/Al2024 of 12% [145]. They justify this improvement by the formation of a proper interface between the CNTs and the matrix coupled with the fact that CNTs have very low intrinsic CTE [145]. Finally, Datsuyk et al. found that a decrease in the CTE of bulk CNT/Cu composites of up to 75% can be achieved by the combination of the low expansion coefficient and large surface area of CNTs [146].

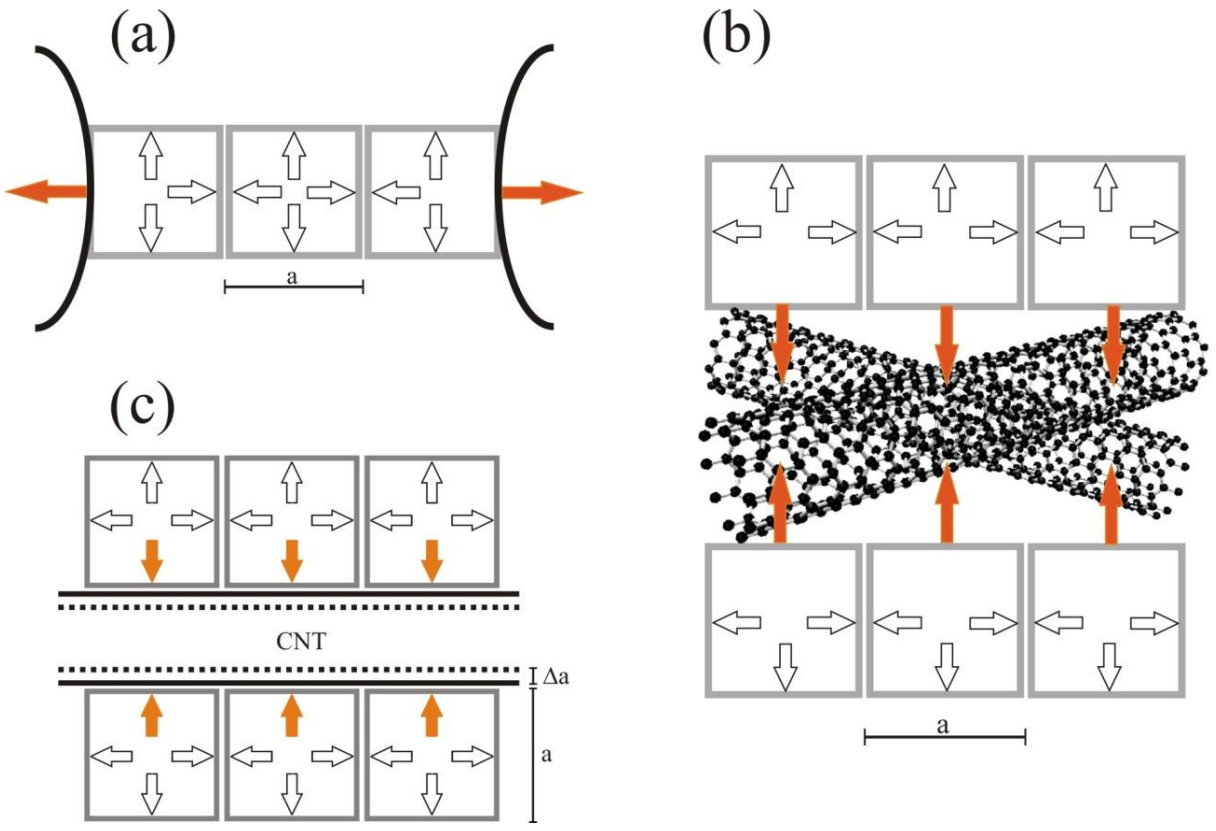

Figure VI-8 - Scheme of possible thermal expansion mechanisms of the Ni unit cells in presence of CNTs (not to scale). Lattice expansion between (a) porosities, (b) CNT clusters and (c) grain boundaries delimited by a single CNT. The lattice parameter of Ni is represented by "a".

In order to explain the observed behaviour of the CTEs, three main probable lattice expansion mechanisms that could be acting in the composites during the thermal input are suggested. Since

the expansion is measured in the Ni matrix, the lattice unit cells that are adjacent to pores or clusters present more free volume to expand without restraint (Figure VI-8-a and b). When a single CNT is in a grain border (Figure VI-8-c), the adjacent unit cells also expand more than the ones inside the grain since CNTs have zero or negative thermal expansion under thermal inputs [128]. The linear and volumetric thermal expansion behaviour and the contraction modes for the CNTs are shown in Figure VI-9 [128]. In the temperature range tested in this work, the CNTs present a volumetric contraction ranging from 2 and 4%. By analysing the variation of the lattice parameter with the temperature for all the samples (with and without embedded CNTs), a shift in the values in the $10^{-2} – 10^{-3}$ Å range is observed. This variation represents the absolute dimensional change in the lattice. When compared to the lattice parameter at room temperature and the CNT diameters, it is about 3 to 4 orders of magnitude lower. Despite this difference and considering the CTE close to zero for the CNTs [128], it can be assumed that the anchoring provided by the CNTs to the matrix could actually be enhanced by the absorption of lateral displacement by the CNTs. When studying the behaviour at a lower scale, this effect is observed as a partially-free expansion of the lattice within the composite. However, when measured macroscopically, it produces a reduction in the coefficient of thermal expansion.

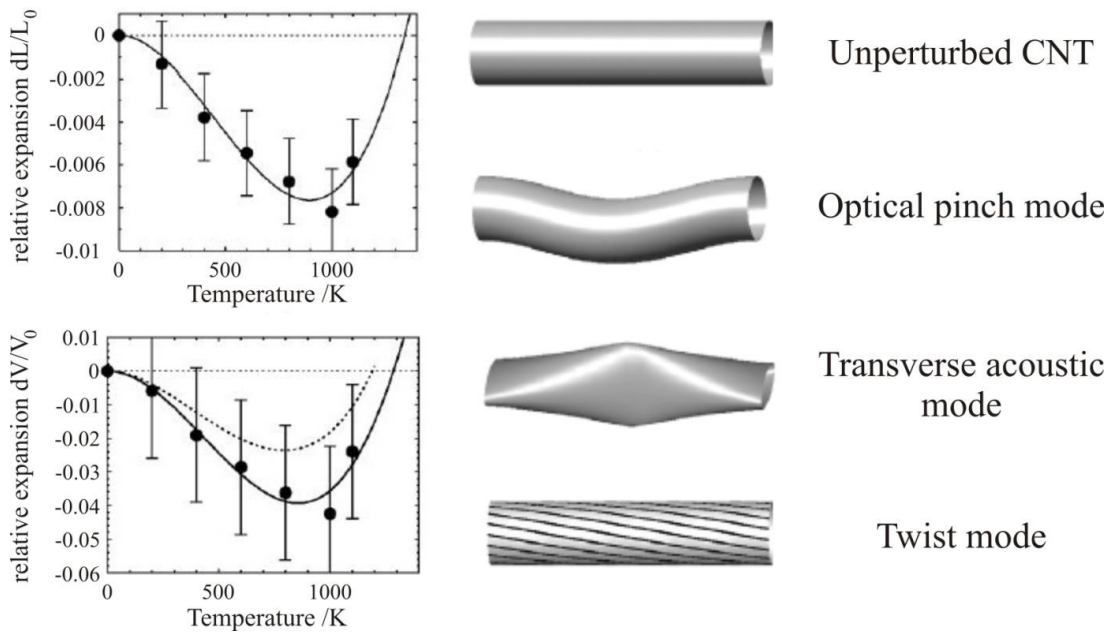

Figure VI-9 – Relative linear and volumetric thermal expansion of CNTs up to 1400 K. CNTs have negative thermal expansion in a very large temperature range. On the right hand side, the probable expansion modes proposed by Kwon et al are depicted [128].

This difference might be due to unmeasured lattice defects originated by the addition of CNTs into the manufacturing process. The presence of second-phase particles introduces deviations from the expected behaviour based on previous studies carried out with the same technique. For

example, in the case of Ni-based alloys [129,130], the results are in accordance with commercial values. The influence of second phases on the behaviour must be carefully determined using complementary techniques (such as in-situ high temperature TEM) in order to state a definitive conclusion regarding the thermomechanical behaviour of composites. In this regard, further experiments are required in order to either confirm or dismiss the presented hypotheses.

VI.3. Summary

The response to thermal expansion of the composites was analysed by bulk dilatometry, showing a decrease in the CTE for both manufacturing methods. Particularly, the CPS sample showed a marked reduction (approximately 76%) compared to pure Ni. This difference might be due to mass transport during a second sintering of the composite. The HUP sample also showed a significant reduction of the CTE, evidencing the interaction with the CNTs. The reduction in both types of composites is directly related to the anchorage given by the MWCNTs to the matrix preventing larger thermal expansions. A subsequent study with higher CNT concentrations presented interesting results regarding the interactions. The 2.0 wt.% sample had an intercept which separated the response in two sections. The first showed a decreased CTE compared to pure Ni, whereas the second exceeded it. The 5.0 wt.% sample exceeded throughout the whole process the reference response. Both behaviours are correlated to a bloating effect, produced by the impossibility of the adsorbed gases to exhaust and leave the remaining porosity. This behaviour should be avoided in order to obtain a useful response in the composites.

In order to corroborate the widely cited anchoring effect of the CNTs, the lattice expansion behaviour of the Ni matrix was studied by means of HT-XRD. The lattice parameters of the Ni composites were determined as a function of the temperature by XRD using the Nelson-Riley method, thus avoiding systematic errors from the thermal expansion of the sample holder. Interestingly, the addition of MWCNTs as fillers increases the lattice coefficient of thermal expansion mainly due to the presence of free volume between the grains in the matrix produced by the agglomeration of nanotubes and porosity. Moreover, no significant variation of the CTE was observed after increasing the percentage of carbon nanotubes. From the interpretation of the experimental results, three different acting mechanisms are proposed which may explain the macroscopic response in the bulk material. The difference in the bulk CTE measured in previous works can be explained by the presence of dislocations, defects and voids. Moreover,

anchoring provided by the CNTs to the matrix could actually be enhanced by the absorption of lateral displacement by the CNTs. The results presented in this chapter also highlight the importance of stating the limitations of different techniques that measure similar physical properties. Other complementary techniques should be accordingly compared in order to state a definitive conclusion regarding the thermomechanical behaviour of Ni matrices filled with CNTs.

VII. Mechanical properties: grain boundary strengthening

VII.1. Introduction

Metal matrix composites show great advances towards the improvement of the mechanical properties of materials with low intrinsic strength such as aluminium or copper. Particularly, nickel is a moderate-strength metal with a density comparable to that of copper but with a higher melting point, hardness and tensile strength. Many studies on the hardness and wear properties of nickel-based coating films focused on samples prepared by electroless [117] or electrochemical deposition techniques [80,147,148]. They observed that the addition of MWCNTs to a metallic matrix leads to a hardness increment of the samples.

In this chapter, the work is focused on powder metallurgy bulk Ni/CNT samples. An increment in hardness is expected, which could be tailored by varying the amount of reinforcement. The addition of MWCNTs should hinder the grain growth and increase the hardness, verifying the Hall-Petch relationship. The composites are characterised using X-ray diffraction (XRD), Electron Backscattered Diffraction (EBSD) and Vickers micro hardness. The relationship between the hardness and the mean grain size of composites with four different MWCNT concentrations (1.0, 2.0, 3.0 and 5.0 wt.%) is investigated. An approach to predict the final grain size of the composites comparing the experimental data to the theoretical models is proposed.

VII.2. Results and discussion

XRD was employed with two main purposes: the first is to assess the initial grain size of the unsintered samples using the method described before, and the second, to analyse the possible formation of new phases from the reaction between the CNTs and the matrix during the experiment. Moreover, as a complementary evaluation of the reactions between said components, Raman spectroscopy was performed on the composites.

The initial grain sizes of the composites as well as the reference sample are depicted in Table VII-1.

Table VII-1– Initial and final mean grain sizes and Vickers microhardness of the studied samples. The initial grain size was determined by XRD measurements, whereas the final grain sized was determined by EBSD.

Sample	Initial grain size (XRD) [nm]	Final grain size (EBSD) [μm]	Vickers Hardness [$HV_{0.1}$]
Pure Ni	27.9 ± 16.7	8.87 ± 0.47	107.1 ± 4.5
MWCNT/Ni 1.0 wt.%	27.8 ± 12.7	7.58 ± 0.62	121.3 ± 5.1
MWCNT/Ni 2.0 wt.%	28.4 ± 16.9	6.30 ± 0.32	123.9 ± 2.7
MWCNT/Ni 3.0 wt.%	29.3 ± 16.7	5.11 ± 0.17	136.4 ± 6.2
MWCNT/Ni 5.0 wt.%	27.3 ± 15.7	6.39 ± 0.21	135.1 ± 3.5

All the samples start with approximately the same grain size (between 27 and 29 nm). After the densification process, the final grain size shows a marked tendency inversely proportional to the amount of CNTs in the composite up to 3.0 wt.%. The 5.0 wt.% sample does not fit into said tendency. The high volume fraction (approximately 27%) favours the reagglomeration of the CNTs, reducing the energy absorption from the moving grain boundaries (Figure VII-1), as already discussed in previous chapters. The reagglomeration of CNTs has been previously studied and described in powder metallurgical samples [82].

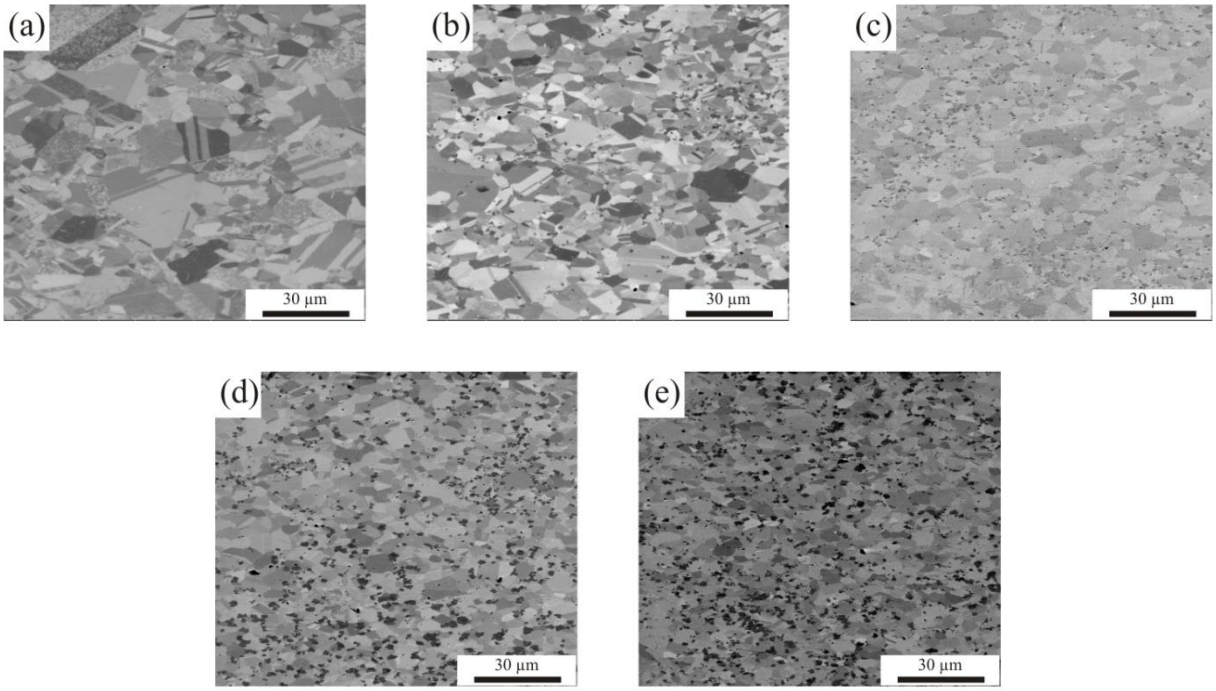

Figure VII-1– Ion channelling contrast electron micrographs of (a)Pure Ni,(b)1.0 wt.%, (c) 2.0 wt.%, (d) 3.0 wt.% and (e) 5.0 wt.% samples . The darker spots observed within the Ni matrix correspond to submicron CNT-bundles.

The electron micrographs taken at a magnification of 1000x show the distribution of the submicron sized CNT-clusters distributed within the Ni matrix (Figure VII-1). The increase in the cluster concentration is noticeable for the high CNT-content composites. Furthermore, no significant porosity is observed on the analysed surface, depicting a proper densification in the samples.

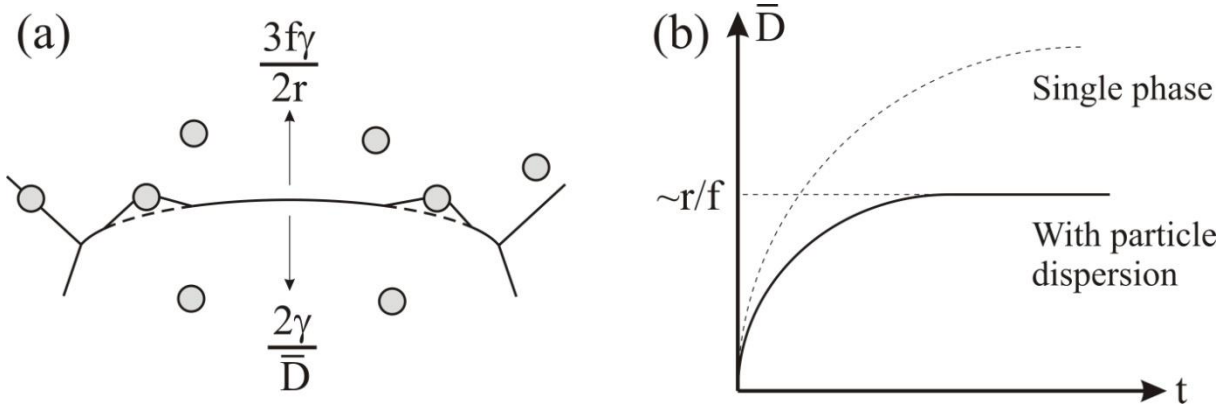

Figure VII-2 – (a) Scheme of the interaction forces between the grain boundary and the second-phase particles. (b) Theoretical model highlighting the grain growth stagnation in the presence of a particle dispersion [108].

In all composite cases, the final grain size is directly related to grain growth stagnation due to Zener pinning generated by the presence of a second phase, in this case predominantly the CNTs. The physical foundation of this effect is that the fillers act as pinning points reducing the grain boundary mobility by diminishing the interfacial energy every time a boundary passes through (Figure VII-2a) [108]. When the driving force of grain growth equals the restraining force exerted by the reinforcement, the growth is halted. This effect is already well known for composites with a second-phase particle dispersion, acting as a final grain size control mechanism during growth or recrystallisation (Figure VII-2b) [109].

The final grain size distribution of the samples was determined by EBSD maps enabling the analysis of the influence of the CNTs on the microstructural growth type. Pure Ni (Figure VII-3a) and MWCNT/Ni 1.0 wt.% (Figure VII-3b) present an abnormal grain growth, whereas MWCNT/Ni 2.0 wt.% (Figure VII-3c), MWCNT/Ni 3.0 wt.% (Figure VII-3d) and 5.0 wt.% samples (Figure VII-3e) exhibit a refined and uniform microstructure. Abnormal growth is known to happen when normal grain growth is hindered by the presence of second-phase particles [108]. These particles might be precipitates, reinforcements or even porosity. Thus, it can be stated that low concentrations of CNTs (i.e. 1.0 wt.%) is not enough to produce a uniform refinement of the microstructure, effect clearly observed in the higher concentration samples

where the uniformity of the refinement was influenced by the proper dispersion and larger amount of CNTs.

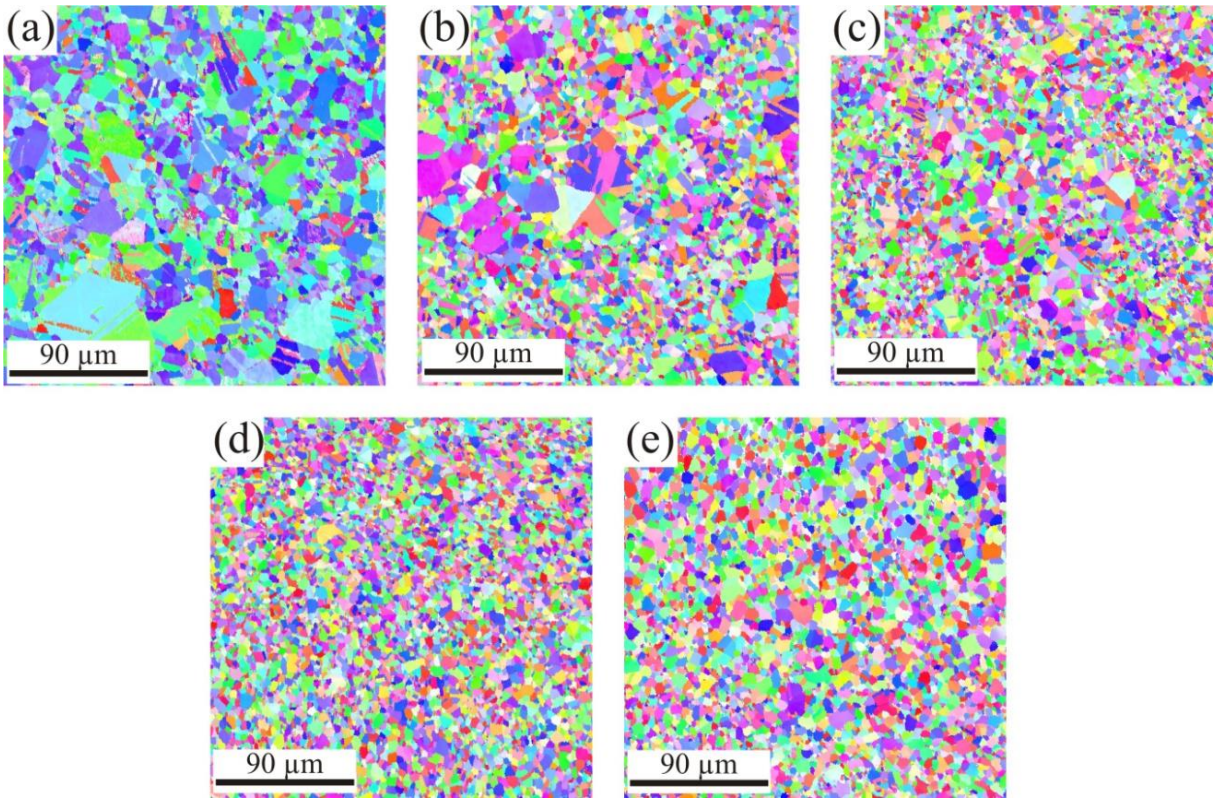

Figure VII-3– Inverse pole figures (IPF) of the studied samples (a) Pure Ni, (b) MWCNT/Ni 1.0 wt.% , (c) MWCNT/Ni 2.0 wt.% , (d) MWCNT/Ni 3.0 wt.%, (e) MWCNT/Ni 5.0 wt.%. Each colour represents a crystallographic orientation.

The mean grain size distribution can be described by a log-normal function [123], and is shown for each sample in Figure VII-4. For the case of pure Ni (Figure VII-4a) and MWCNT/Ni 1.0 wt.% (Figure VII-4b) the span of the grain size distribution covers approximately up to 45 µm and 27 µm respectively. The size spread is not regular, showing misfit points on the larger grain size columns depicting a multimodal grain size distribution. This is a clear characteristic of abnormal growth. However, in the samples with higher CNT contents this is not observed, presenting log-normal distributions with high correlation coefficients. By comparing all the curves, there is a clear shift of the mean value towards lower grain sizes up to the 3.0 wt.% sample. Already in the 5.0 wt.% sample, there is an inversion towards larger grain sizes resulting in a mean grain size comparable to that of the 2.0 wt.% sample.

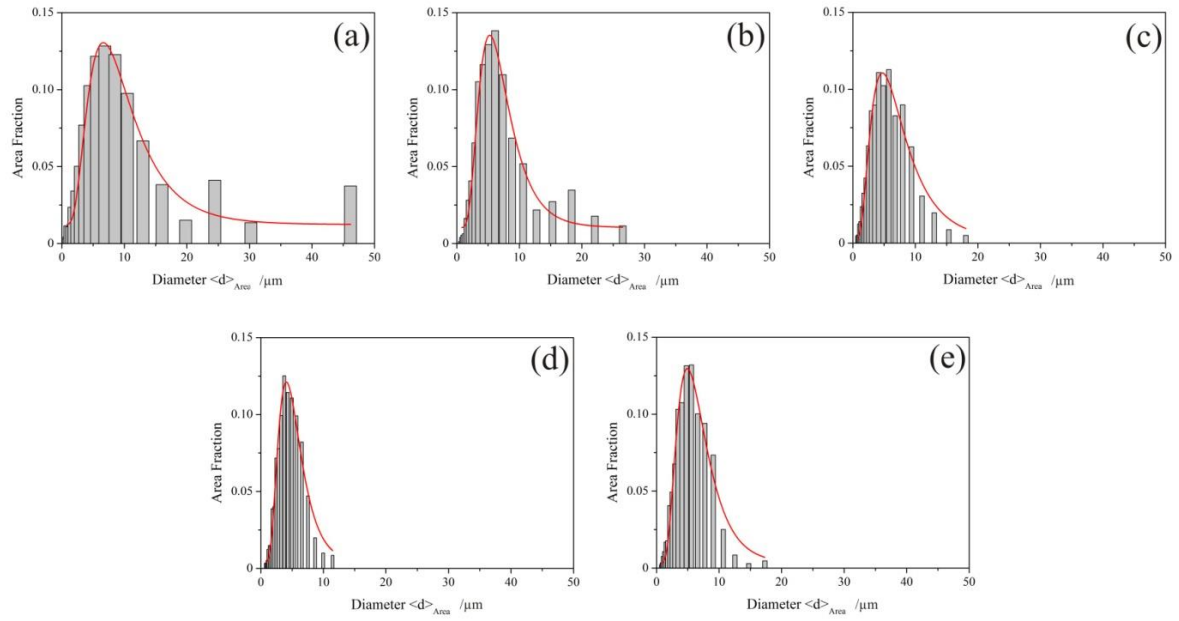

Figure VII-4– Final mean grain size distributions of the samples obtained by EBSD measurements. (a) Pure Ni, (b) MWCNT/Ni 1.0 wt.%, (c) MWCNT/Ni 2.0 wt.% , (d) MWCNT/Ni 3.0 wt.% and (e) MWCNT/Ni 5.0 wt.%. All the samples show a Log-normal type distribution of the grain sizes.

The refined grain size should lead to a mechanical response as described by the Hall-Petch effect, which states that the yield strength (or hardness) is inversely proportional to the grain size [39]. As stated before, grain growth stagnation is promoted by the CNTs, resulting in a final grain size smaller than in pure metals under the same conditions. This feature increases the amount of grain boundaries, hindering the dislocation mobility and therefore improving the hardness. The Hall-Petch effect in metal matrix composites reinforced with CNTs has been reported in the literature for certain systems. Choi et al. [74] described the strengthening of MWCNT/Al composites (manufactured by hot rolling of ball milled powder) as a consequence of grain refinement and load transfer from matrix to reinforcement. Carpenter et al. [117] discussed the increase in hardness as a sum of Orowan strengthening and the Hall-Petch effect for electrodeposited CNT/Ni coatings.

Hardness values are presented in Table VII-1. The CNT-reinforced samples showed hardness improvements of 13.2, 16.7, 27.4 and 26.1% (1.0, 2.0, 3.0 and 5.0 wt.% respectively) relative to the pure Ni reference. In order to assess the influence of the Hall-Petch effect in the mechanical behaviour of materials, the grain size dependency of the hardness was plotted (Figure VII-5).

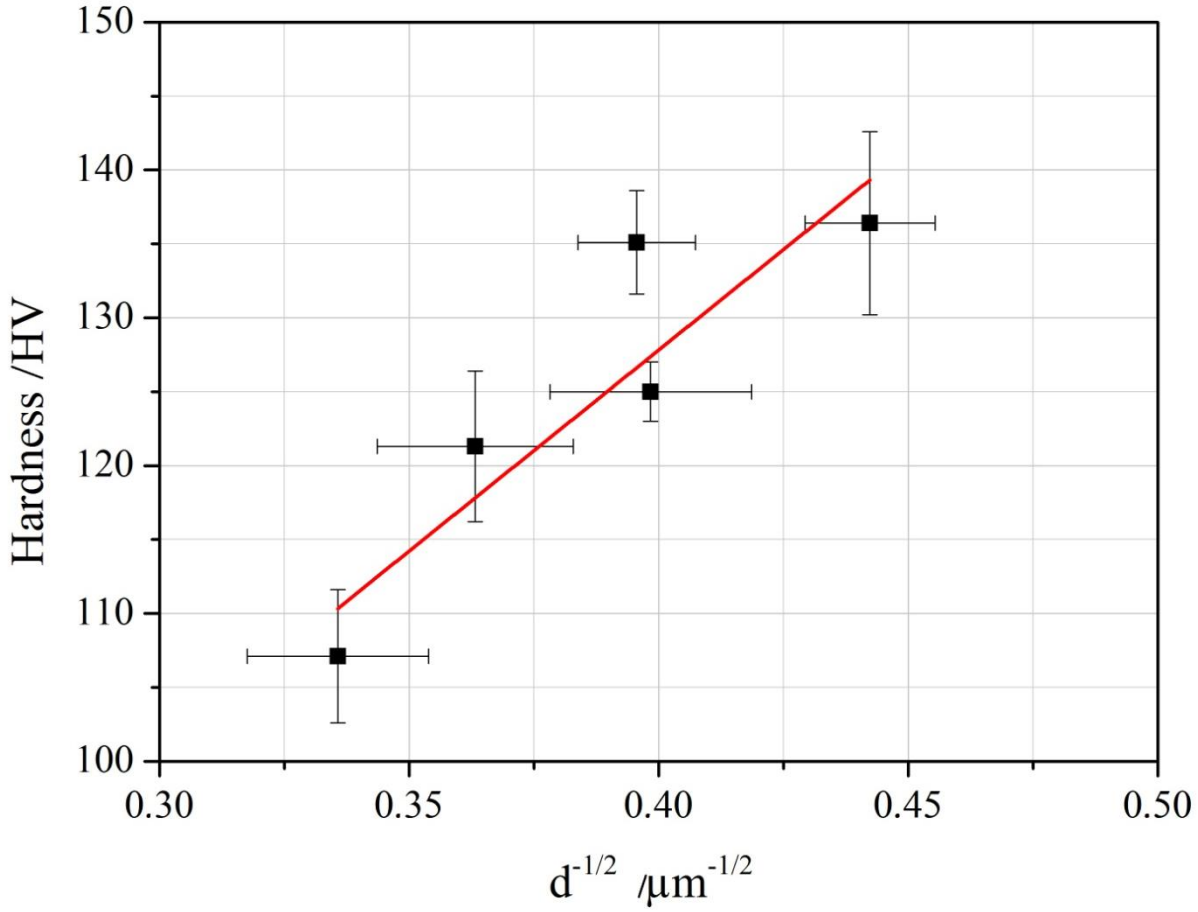

Figure VII-5– Hall-Petch plot of the composite hardness versus the inverse square root of the mean grain size. A linear fit is depicted to highlight the tendency.

The plot contains a linear fit of the data set, confirming a predominant Hall-Petch effect that correlates the mechanical properties to the microstructure. It must be clarified that Hall-Petch is probably not the only hardness enhancing mechanism acting in the samples, a load transfer from the matrix to the reinforcements might also be expected. However, this is not considered as the prime mechanism due to the low wettability of the CNTs with metals [53], which results in a weakly bonded interface between the MWCNTs and the Ni matrix.

With regard to the grain size refinement due to a second phase dispersion, several authors have reported prediction laws which should represent the expected final grain size [124] and are based on the Zener model reported by Smith [149]. The prediction is based upon an empirical equation which considers the size and volume fraction of the second phase. As such, it only predicts the final grain size for a particular system under specific conditions. For the case of the present study, four of the many reported models were tested based on the study of Muralidharan et al. [114] so as to assess the fitting to the experimental results. The considered models are those from: Zener and Hillert, which both consider random particle/ grain boundary

intersection; Anderson, which was designed from 2D growth computer simulations; and Anand-Gurland, which considers that all particles are placed at grain boundaries. The results are shown in Table VII-2. It can be clearly seen that the results differ significantly with those obtained by direct measurement with EBSD (Table VII-1).

Table VII-2– Predicted final size in composite materials subjected to Zener pinning [114,124].

			Predicted mean final grain size [μm]			
Sample	Vol. fraction MWCNT/Ni (*f*)	CNT radius (*r*) [m]	Zener	Hillert	Anderson	Anand-Gurland
			k: 4/3; n:1	k: 8/9; n:0.93	k: 4.5±0.8; n:0.31±0.02	k: 4; n:0.5
1%	0.0647	$7.5x10^{-9}$	0.155	0.085	0.158	0.118
2%	0.1226		0.082	0.047	0.129	0.086
3%	0.1747		0.057	0.034	0.116	0.072
5%	0.2649		0.038	0.023	0.102	0.058

Since the analysed models failed to predict the final grain size, a new approach is proposed based on the mean grain sizes of the 1.0, 2.0 and 3.0 wt.% samples. Beyond 3.0 wt.%, there is no significant additional reinforcing effect of the CNTs due to reagglomeration. This statement is in close agreement with previously reported values for MWCNT/Cu bulk composites produced by powder metallurgy [125].

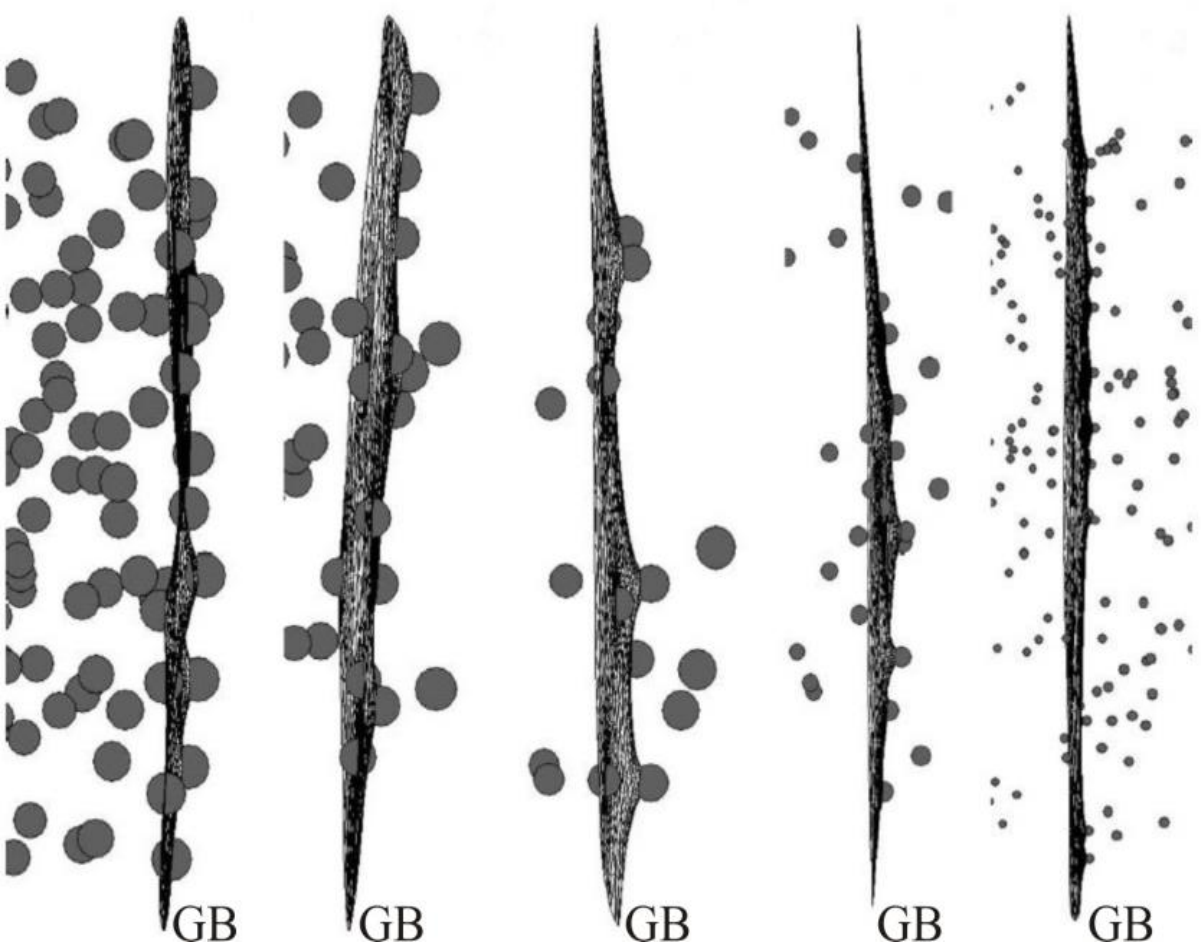

Figure VII-6 – Classical approach for the grain boundary pinning by spherical particles [110].

The general equation predicting the grain size (Equation VII-1: D represents the mean final grain size, r is the second-phase radius and f is the second-phase volume fraction), is based on the assumption that the second phase is spherical and has a monomodal size distribution (Figure VII-6). These hypotheses collide with the reality, in which the particles usually have a randomly-shaped multimodal size distribution. In this sense, Sun et al. [150] reported an approach in which they consider the specific surface per unit volume (S_v) as an important factor. This stereological parameter approximates the model to real cases, since it does not need to consider the 3D particle size distribution or the assumption of spherical particles. For this study, the boundary drag model would be as is shown in Figure VII-7.

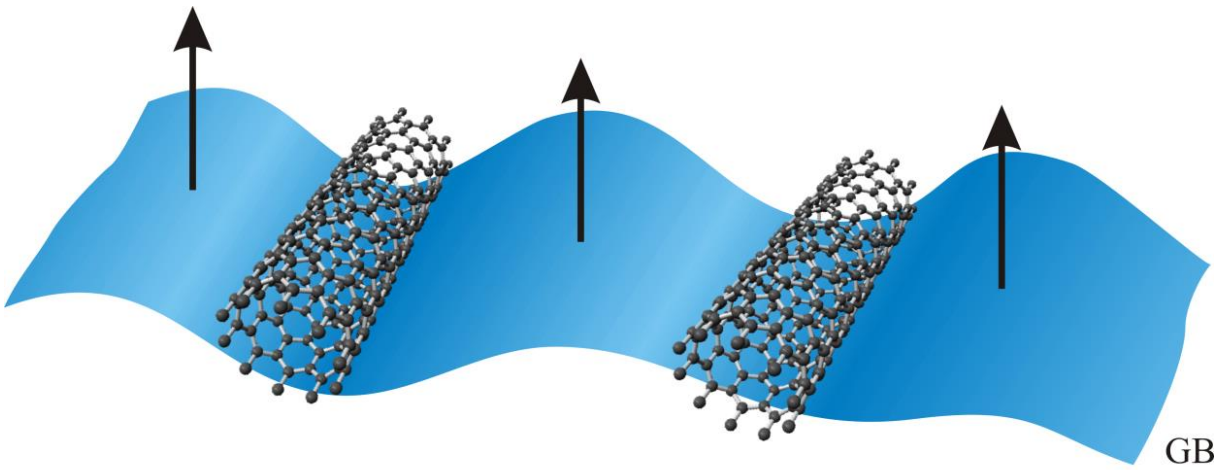

Figure VII-7 – Scheme of the grain boundary pinning by cylindrical bodies (in this case, carbon nanotubes).

If the new parameter is considered in the general equation, it results in the following:

$$D = \frac{k.r}{f^n} \quad \text{(Equation VII-1)} \qquad D = \frac{4.k}{S_v.f^n} = \frac{k'}{f^n} \quad \text{(Equation VII-2)}$$

For the case of CNTs, this approach was analysed by Lahiri et al. [76], observing that the influence of S_v is inversely proportional to the final grain size (Equation VII-2). When working with coarse-grained materials (as in this study), it is expected that the proportionality constant k reach values higher than those reported for the ideal cases. Summarising, considering the nature of the reinforcing phase and its high specific surface [151], the model was constructed starting with the modified general equation (Equation VII-2) and a confidence index of 98%. The following model was obtained based on the calculation of the remaining parameters (i.e. factor n and proportionality constant, k') for the particular case of this study:

$$D = \frac{2560 \pm 70}{f^{0.397 \pm 0.013}} \ [nm] \quad \text{(Equation VII- 3)}$$

A graphical representation of the obtained model is depicted in Figure VII-8. The experimental data and its standard deviation is also plotted to observe the validity of the model within the studied partial concentration range. The curves have a very good correlation to the experimental points. Since this is a first approximation to the bulk MWCNT/Ni system, it is recommended that further experiments with different CNT concentrations should be carried out in order to refine the proposed model.

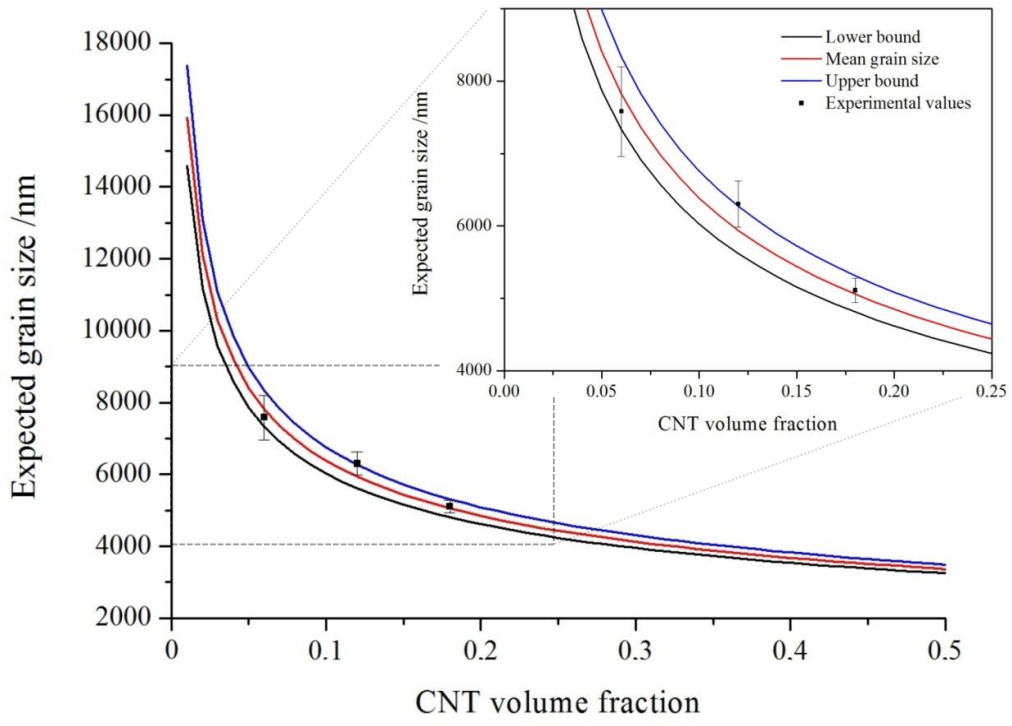

Figure VII-8 – Plot of the proposed model with the upper and lower bounds. The inset shows in detail a reduced reinforcing range (up to 25 vol%)

VII.3. Summary

An empirical reinforcement limit has been determined for CNT reinforced MMCs at 3.0 wt.% (approx. 17 vol.%). No significant improvement in the mechanical properties is observed beyond this limit. The reduction of the reinforcing effect above this value is mainly generated by the reagglomeration of CNTs due to the high volume fraction (approx. 27 vol.%).

The Hall-Petch relationship is confirmed for the composites, irrespective of the relative CNT amount. Despite this fact, it must be clarified that Hall-Petch is probably not the only enhancing mechanism acting; a load transfer from the matrix to the reinforcements might also be expected.

A new growth modelling equation is proposed for the studied system, suitable for composites up to the aforementioned empirical concentration limit and independent from the second phase particle shape. Beyond this point, the behaviour cannot be described by Zener pinning due to the increment in the CNT reagglomeration. Further experiments with different CNT concentrations are required in order to refine the proposed model.

VIII. Tribological properties: friction and wear behaviour

VIII.1. Introduction

One of the main factors affecting the reliability of electrical contacts is their tribological behaviour. This problem was partially overcome by the use of coatings, but a common drawback is life span [152]. The existence of high friction between to electrical contacts will induce severe plastic deformation and subsequent failure. Moreover, the generated wear particles will generate failure mechanisms (i.e. ploughing), increasing the friction and thus, accelerating their damage. A low-friction material is thus advantageous in the sense that it avoids superficial plastic deformation at the contact surface and may result in elastic sliding [153].

In the present chapter, the friction results obtained for bulk CNT-reinforced Ni composites manufactured by two different powder metallurgy routes are shown. These results are contrasted with a pure Ni reference in order to determine the influence of the CNTs on the friction and wear behaviour, correlated to the resulting composite microstructure. Finally, the conventional Archard wear model was adjusted to achieve a more suitable description of the microstructural influence on the wear rate.

VIII.2. Results and discussion

VIII.2.1. Microstructural characterisation

Figure VIII-1 shows EBSD surface scans of the samples before the tribological tests and the respective grain distribution histograms. It can be observed that the size of the grains decreases by adding CNTs to the composite [120]. This has been already clarified in chapter VII and is generated by grain growth stagnation produced by the CNTs.

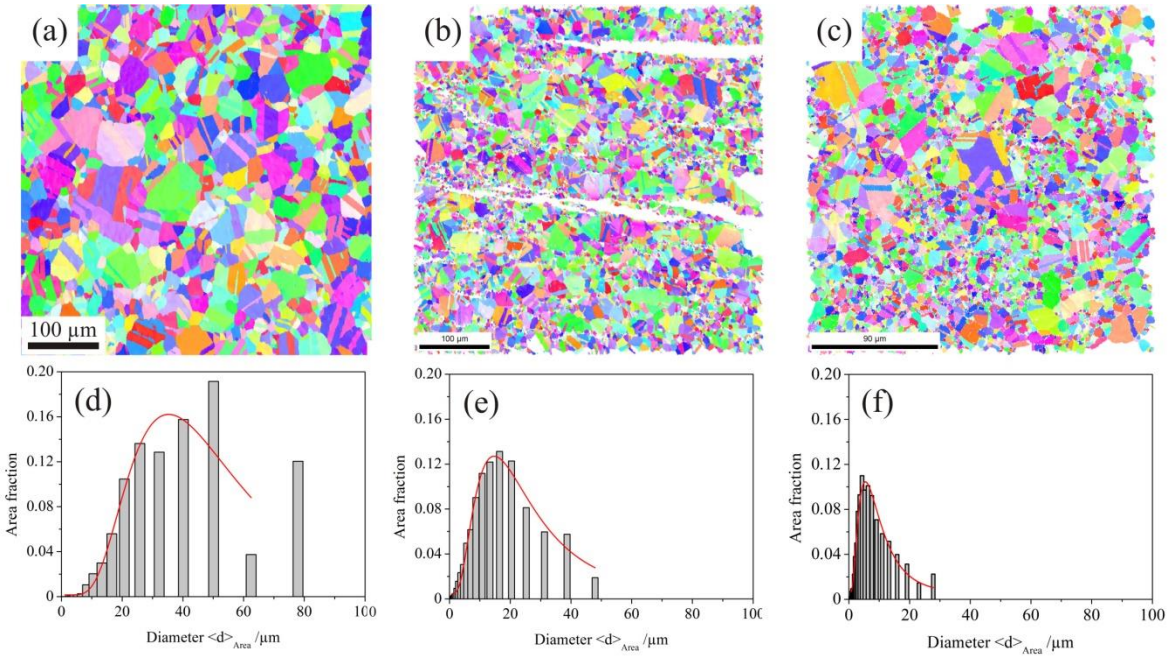

Figure VIII-1 – EBSD inverse pole figure maps of the surface prior to the tribological tests, highlighting the grain size distribution of (a) Pure Ni, (b) MWCNT/Ni 1.0 wt.% CPS and (c) MWCNT/Ni 1.0 wt.% HUP. The scale bar in (c) differs from those in (a) and (b). Figures d, e and f are the respective grain distribution histograms.

The main difference between the Ni reference sample (Figure VIII-1a) and the MWCNT-reinforced samples (Figure VIII-1 b and c) is that the grain growth in the former is only hindered by the porosity. During sintering, porosity migrates to grain boundaries, reducing the energy and slowing the growth, whereas in the CNT samples, the nanotubes provide an extra hindering phase which further reduces the grain boundary mobility [154].

The difference between the two composites is mainly due to the higher amount of agglomerates in the CPS sample. With this production technique, a higher degree of reagglomeration due to poor cohesion between the matrix and the CNTs has been observed, related to the absence of pressure during sintering, as already explained in previous chapters [82,140].

This difference in the agglomeration can be noticed in Figure VIII-2, which shows fracture surfaces of the MWCNT/Ni 1.0 wt.% CPS (Figure VIII-2a) and HUP (Figure VIII-2b) samples. The agglomerates and voids in the CPS sample are highlighted with an ellipse on the figure.

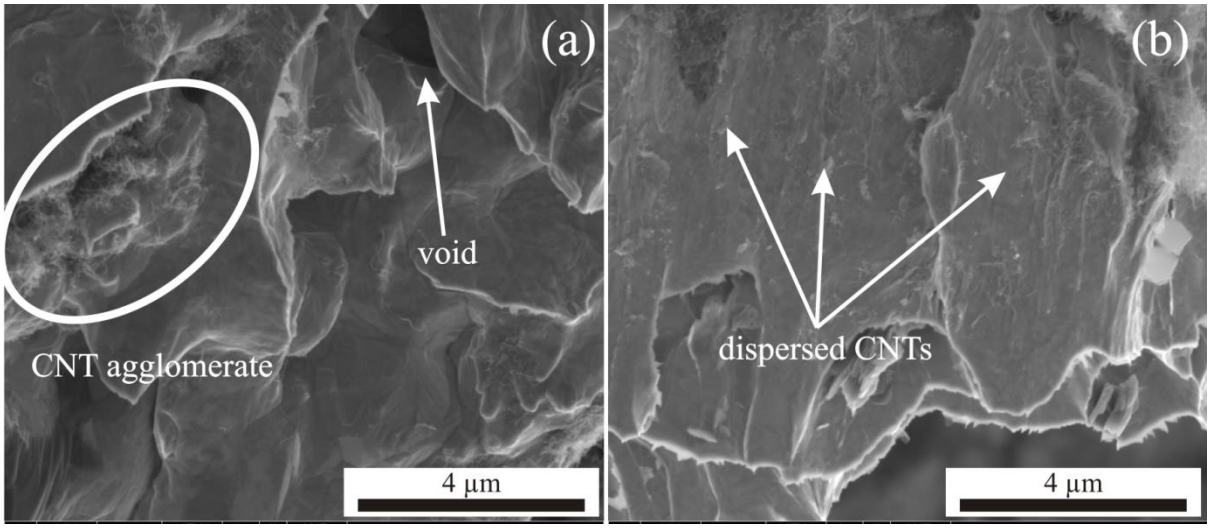

Figure VIII-2 – Fracture surfaces of the CNT-containing samples. (a) MWCNT/Ni 1.0 wt.% CPS and (b) MWCNT/Ni 1.0 wt.% HUP. The CNT agglomerates, voids and dispersed CNTs are highlighted.

Another difference between CPS and HUP is the densification temperature used during sintering [18]. However, this is not the only factor playing a role on the final grain size and density, since the applied pressure during HUP helps to improve the densification by avoiding the swelling (or gas bloating) of the sample. Moreover, there are other densification mechanisms in HUP that do not act in CPS (i.e. plastic deformation and creep).

A summary of the mean grain size and microhardness values for the tested samples is found in Table VIII-1.

Table VIII-1 - Mean grain size, Vickers microhardness and root mean square roughness of the samples

Sample	Mean grain size [µm]	Vickers microhardness $HV_{0.1}$	RMS Roughness [nm]
Pure Ni	47.54 ± 3.06	92.2 ± 2.6	18.8 ± 17.7
1.0 wt.% CPS	22.39 ± 0.96	119.3 ± 5.3	26.7 ± 7.1
1.0 wt.% HUP	7.58 ± 0.62	131.5 ± 7.0	46.9 ± 10.2

VIII.2.2. Friction behaviour

The coefficient of friction (COF) was evaluated for loads ranging from 50 to 300 mN for the three sample sets. Figure VIII-3 depicts the values for each load, showing a clear difference between the CNT-containing samples in comparison to the Ni reference.

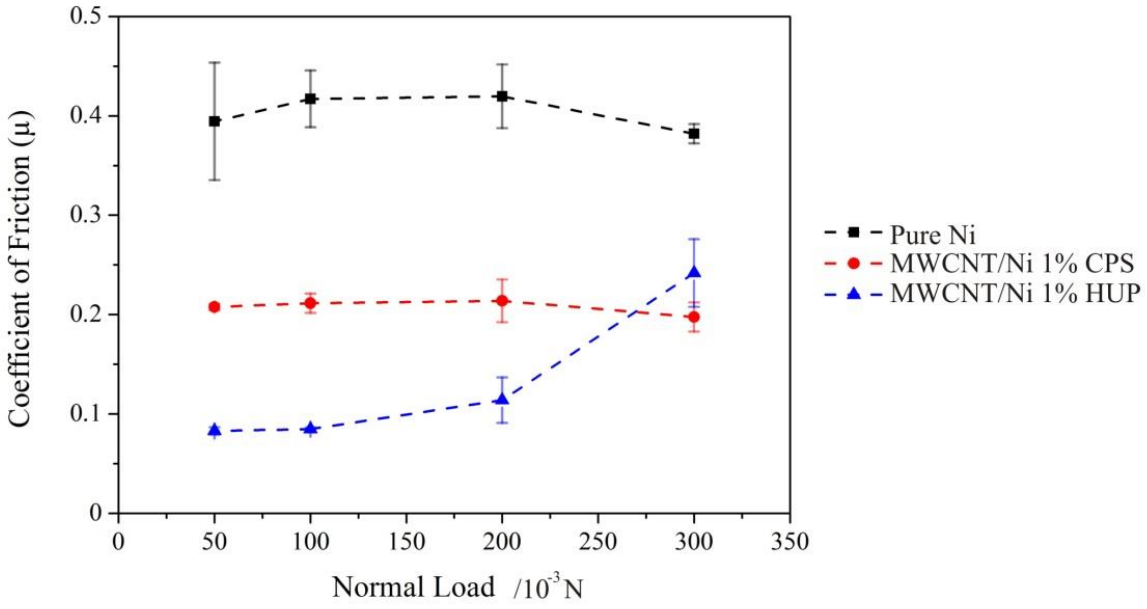

Figure VIII-3 – Average coefficient of friction (COF) versus the different experimental loads under dry conditions.

In the case of the 1.0 wt.% HUP sample, the maximum COF reduction is about 67%, whereas in the CPS sample the reduction is close to 50%, both of which are above the expected values reported in the literature [155,156]. This significant difference could be related to several isolated effects or a combination thereof.

For the sake of the analysis, the discussion of the friction results will be separated into two different regions. The first one covers lower loads, i.e. 50 and 100 mN. The second group covers the higher tested loads (200 and 300 mN), where a non-trivial behaviour is observed particularly in the HUP sample.

Region I – Lower loads

In this load region, the evolution of the COF throughout the friction experiment is roughly the same for the three types of samples, showing no particular influence of the load on the friction behaviour (Figure VIII-4).

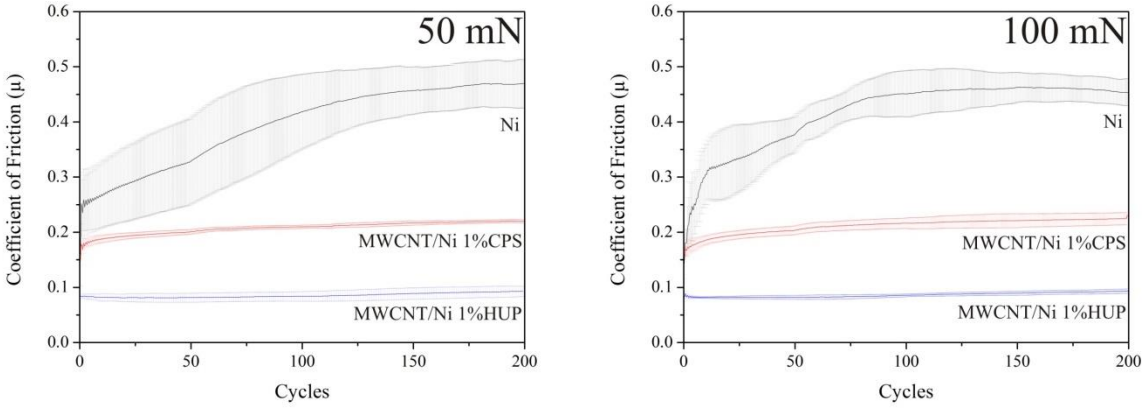

Figure VIII-4 – Mean COF evolution over the sliding cycles for lower loads. Experimental loads for each are shown on the upper right corner.

The obtained mean COFs were 0.4, 0.2 and 0.1 for the pure Ni, 1% CPS and 1% HUP samples, respectively. The reference value is in good agreement with those reported in the literature for microcrystalline Ni tested against Al_2O_3 [157]. Equation 1 is used to calculate the Hertzian stresses, where P is the applied normal load, D is the counterpart diameter and C is the effective elastic modulus. The latter can be estimated with equation VIII-2.

$$\sigma_H = 0.918\sqrt[3]{\frac{P}{D^2C^2}} \qquad \text{(Equation VIII-1)}$$

$$C = \left(\frac{1-\nu_1^2}{E_1}\right) + \left(\frac{1-\nu_2^2}{E_2}\right) \qquad \text{(Equation VIII-2)}$$

Considering the tribological pair being tested (Ni/Al_2O_3) and combining equations VIII-1 and 2 with the data available in the literature, the initial (Hertzian) elastic contact pressure between these materials amounts to 1.56 GPa. This value highly exceeds the estimated yield strength of the samples (obtained from the relationship $\sigma_y \sim$ hardness/3), which ranges from 0.3 to 0.45 GPa (pure Ni and 1% HUP respectively). Therefore, under equal load, the yield strength is lower, resulting in a greater penetration depth and a subsequently increased real contact area. In other words, the increase in hardness of the sample hinders the indentation depth of the dynamic counterpart, thus reducing the contact area during the friction test. It would then be reasonable to state that the main role in the friction behaviour at the mentioned loads is played by an indentation-induced plastic deformation mechanism. This effect was also observed in the work of Shafiei and co-workers [157], where they compare the tribological performance of Ni with different grain sizes (micro and nanocrystalline) and mechanical properties. Since all the mean grain sizes in this work are in the micrometre range, our assumption can be correlated to

said study. Nevertheless, another important factor is the presence of a distribution of individual CNTs as well as clusters, which are believed to act as self-lubricating materials [156,158]. As mentioned before, the frictional behaviour can be a combination of effects which are difficult to isolate.

Region II – Higher loads

For higher loads, the COF evolution of the reference and CPS samples remain almost unchanged, whereas in the case of the HUP sample, the COF increases considerably, especially for 300 mN, where the COF of the CPS is surpassed at about 65 cycles (Figure VIII-5).

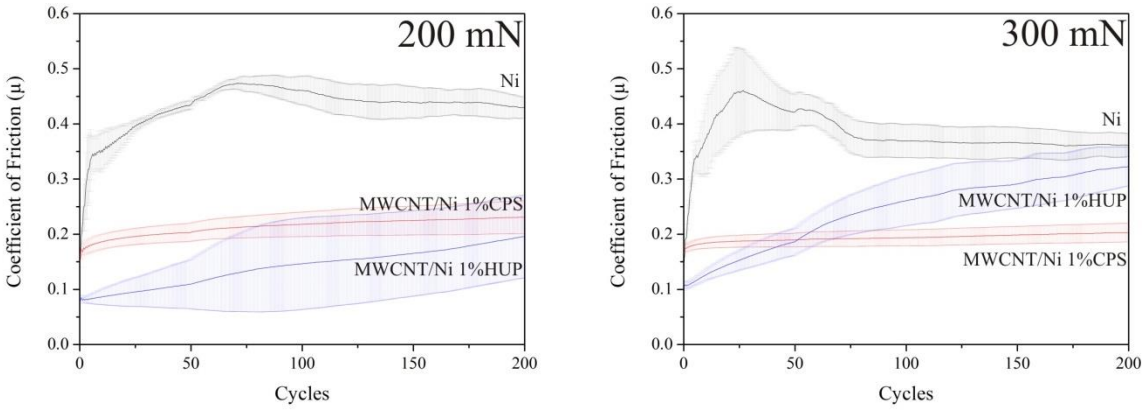

Figure VIII-5 – Mean COF evolution over the sliding cycles for higher loads. Experimental loads for each are shown on the upper right corner.

It is clear that the major influence is not particularly related to the mechanical properties of the composites, but to an underlying effect. In order to understand the experimental findings and to elucidate the aforementioned effect, the chemistry of the worn surfaces was studied by Raman spectroscopy. Focus was put on the 300 mN tracks, believed to contain higher chemical activity. Figure VIII-6 depicts the analysed sectors of each track and their correspondent Raman spectra. There is a clear transition of the wear activity from severe (in the case of the reference sample) to mild wear on the hot-pressed sample. Regarding the chemistry, nickel oxide (NiO) was detected in all the wear tracks [159]: sporadically in the pure Ni and MWCNT/Ni 1%CPS wear tracks, yet continually in the 1%HUP. This may be due to the fact that the larger grains have lower interfacial strength leading to a grain peeling mechanism in the most superficial layers [160]. Moreover, the pure Ni and 1%CPS samples show spallation of the oxide layer with a visible amount of breakage, also resulting in oxide depleted regions.

It is well documented that there is a direct relationship between the microstructural characteristics of a polycrystalline material and its oxidation kinetics. This means that the lower the mean grain size, the higher the oxide layer formation rate. This is attributed to the larger grain boundary area which further translates to an improvement in the diffusion paths for oxygen [157,161]. This formed tribolayer may be both beneficial and detrimental to friction. The upside is that an oxide layer may provide a decrease in the friction coefficient and wear rates in a first stage as studied by Stott et al. [162]. These so-called glazes, when subjected to low speed reciprocating sliding conditions, tend to be compacted providing wear protection. However, due to the brittle nature of the oxide scales, the indentation of the dynamic counterpart will break the glaze and increase the roughness of the track, i.e. increased coefficient of friction [163]. Particularly for NiO [156], it has been found that it acts as a high shear strength layer which increases the friction coefficient. Furthermore, the quality of the CNTs can be estimated from the spectral data. The intensity of the D band illustrates the amount of defects and structural modification in the nanotubes, thus, as is widely accepted, the D to G band ratio accounts for the quality [156]. The I_D/I_G mean ratio were 0.89 (state of the CNTs prior to the tribological tests for both kind of samples), 1.09±0.07 for 1%CPS and 0.93±0.11 for 1%HUP. The higher amount of defects of the 1% CPS sample leads to infer that the CNTs were strongly tribomechanically active during the test as a friction interface which prevents asperity contact. On the other hand, in the 1%HUP sample the CNTs were not as operative throughout the process, being the oxide layer the main interfacial protection.

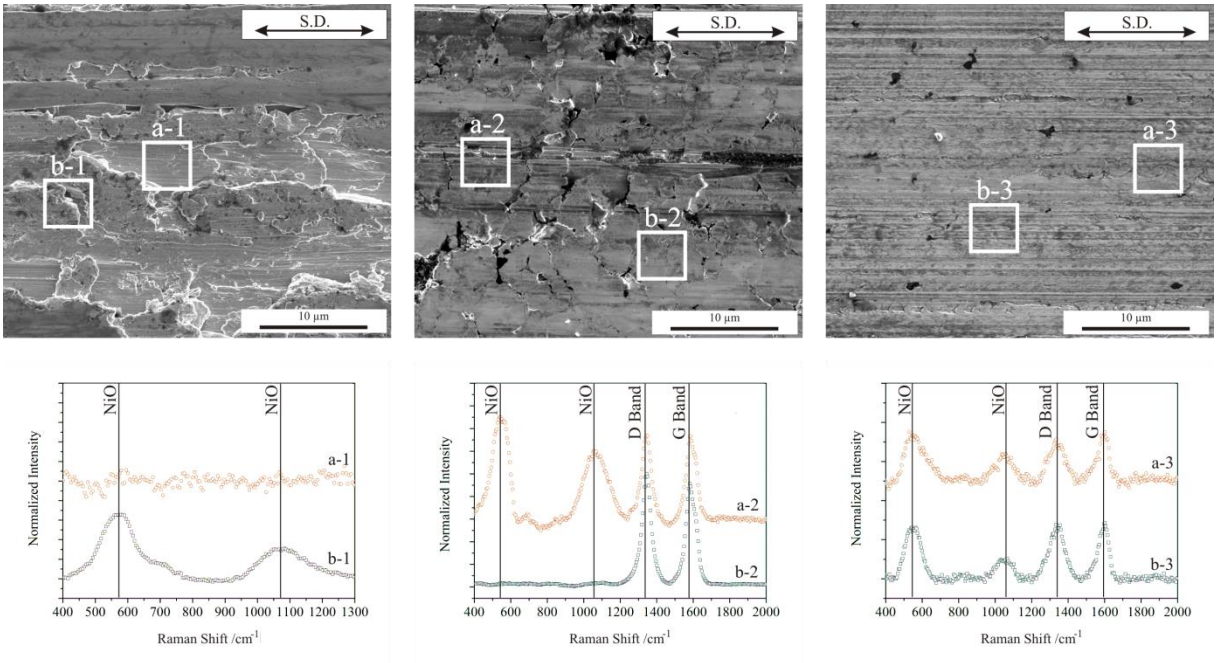

Figure VIII-6 – SEM micrographs of the worn surfaces and their correspondent Raman spectra. From left to right: Pure Ni, MWCNT/Ni 1%CPS and MWCNT/Ni 1% HUP tested at 300mN.S.D stands for sliding direction.

As mentioned before, it is highly unlikely that only one type of friction mechanism is acting in the process, rather, a combination of effects is the more plausible case. Some authors relate the difference between CNT-reinforced bulk composites and the plain matrix to an effect exclusively brought on by the CNTs. In the study carried out by Scharf et al. [156], they observed the formation of a graphitic film which presents low shear strength and favours lubrication. On the other hand, for Dong et al. [158], a decisive carbon film decreases the friction coefficient and retards severe wear. Another important mechanism that is frequently assumed in this type of friction is the enhancement of the interfacial strength between the CNTs and the metallic matrix [160]. It is believed that the increased interfacial strength retards the peeling of the matrix grains, thus reducing wear. A further hypothesis formulated in the literature states that during the friction tests, the CNTs are released to the surface acting as spacers which prevent the asperities from contacting and, to some extent, acting as a lubrication medium [164].

VIII.2.3. Wear behaviour

The evolution of the removed volume follows a marked increment in all three samples, but with different slopes (Figure VIII-7). The wear behaviour is expected to follow the Archard model, which states direct proportionality to the sliding distance and load, and an inverse proportionality to the mechanical properties (hardness) of the tested material. The aforementioned slopes are represented in the equation by a proportionality constant symbolised

by K. For composite materials, this relationship can be further reformulated by considering the Hall-Petch effect generated by the different microstructural refinements brought by the reinforcing phases [165], leading to a modified Archard model. By combining both relationships, the following equation is obtained:

$$W = K\left(\frac{LS}{H}\right) = K\left[\frac{LS}{(H_0 + kd^{-0.5})}\right] \qquad \text{(Equation VIII-3)}$$

Where W is the wear rate per unit sliding distance, K is the wear coefficient, L is the applied load, S is the total sliding distance, H_0 is the hardness of a defect-free single crystal of the bulk material, k is a proportionality constant and d is the mean grain size of the composites. From this equation, the influence of the microstructure on the wear rate during sliding wear can be directly estimated, the wear rate being proportional to the mean grain size of the material.

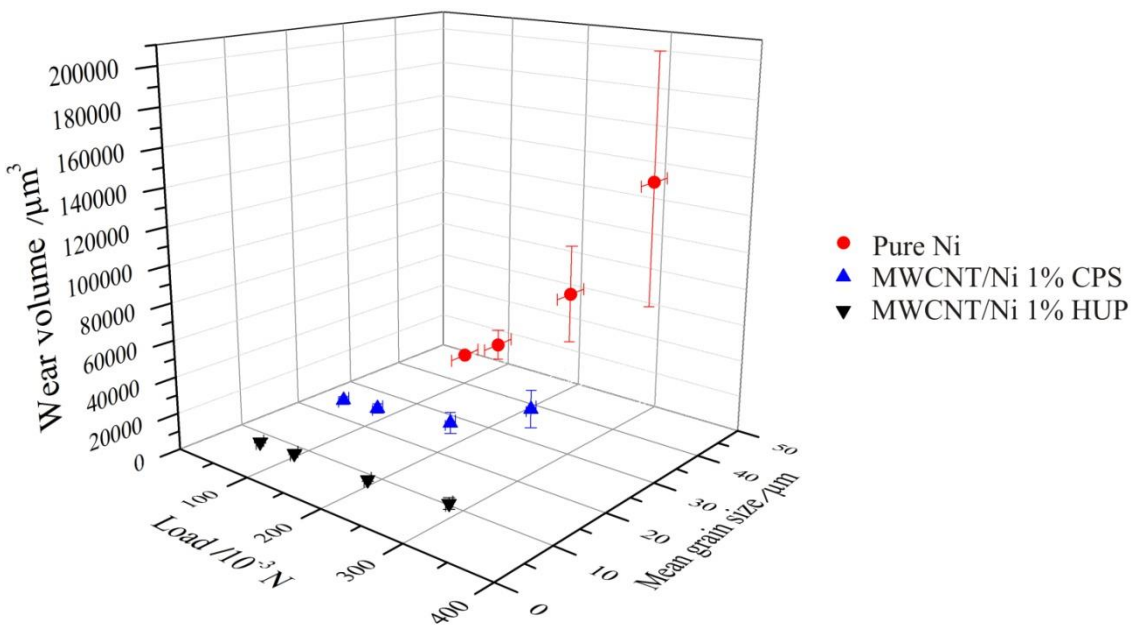

Figure VIII-7 – 3D plot of the wear volume as a function of the applied load and mean grain size. The error is originated from the irregularity (wear track depth and width) of the wear tracks.

The estimation of the wear constant K from the experimental data is presented in Table VIII-2. There is no unanimous agreement about what this constant physically represents, but Rigney has summarised the most accepted interpretations [166]. Most of these express the generation of third bodies and the relationship between the contact and the asperities. Another explanation states that this constant relates the removed to the plastically deformed volume. Since the author affirms that researchers should be cautious in interpreting and extrapolating the experimental wear rates, it would be useful to correlate this constant to a supplementary factor which might help to identify the wear mechanisms affecting sample response. A helpful tool for the

determination of the acting mechanisms in sliding friction from morphological data is provided by the Zum Gahr equation [167] (also named cutting efficiency f_{AB}):

$$f_{AB} = \frac{\sum A_{below} - \sum A_{above}}{\sum A_{below}} = \frac{B - A}{B} \qquad \text{(Equation VIII-4)}$$

Where B is the cross-sectional area of the wear groove below an arbitrary reference plane (for this case, the unaffected sample surface), A represents the summation of the cross-sectional areas of the material displaced to the sides and/or within the track as ridges. The values of f_{AB} range from 0 for a ploughing mechanism (pure plastic deformation) to 1 for a cutting mechanism (pure abrasive effect).

Table VIII-2 - Wear constant K and cutting efficiency f_{AB} values calculated from the experimental data.

Sample	Wear constant K ($x10^{-5}$)	Cutting efficiency f_{AB}
Pure Ni	17.50 ± 13.00	0.60 ± 0.15
MWCNT/Ni 1%CPS	8.75 ± 2.39	0.76 ± 0.13
MWCNT/Ni 1%HUP	2.03 ± 0.56	0.24 ± 0.15

Observing both the cutting efficiency and wear constant results (Table VIII-2), the pure Ni and 1%CPS samples are closer to a cutting mechanism. Considering the relatively scattered values, this may be mainly attributed to irregularities in the analysed wear tracks. Both show a high K value representing more removed than plastically deformed volume. Furthermore, the fact that CNT agglomerates are larger in size and quantity in the CPS samples (compared to HUP samples) [140] makes them tend to roll over the wear surface until they are removed without being taken apart [168]. On the other hand, the 1%HUP sample shows a low f_{AB} value, which indicates that ploughing is the dominant mechanism. This is consistent with the lower K value for this composite, which represents a lower amount of removed versus plastically deformed volume (according to the interpretation given before). These low values of K and f_{AB} for the HUP samples could be related to a redeposition of broken oxide particles that are somehow embedded within the matrix throughout the process.

Summarising, since an isolated interpretation of the constants is very complex (K and f_{AB}), a joint interpretation may prove more useful and straightforward. For this particular case, a good correlation between both is observed.

The presented results are helpful to approach an elucidation of certain aspects of the friction and wear behaviour of these CNT-reinforced bulk composites. It can be concluded that the CNTs have two effects concerning wear ad friction:

- Microstructural refinement: modified oxidation kinetics generates oxidation friction mechanisms; grain boundary strengthening increases hardness and modifies wear behaviour.
- High loads possibly produce higher CNT (friction) activity (higher CPS I_D/I_G ratio, i.e. more active CNTs) as an interfacial lubricant layer.

VIII.3. Summary

Tribochemical studies proved the formation of an oxide layer in all samples, and of a carbon coating film in the CNT-containing samples. The CNTs showed activity throughout the friction process, acting as an interfacial layer which may act as a friction-reducing agent. The formation of a uniform Ni oxide layer in the HUP sample proved to be detrimental to its friction behaviour. This can be traced back to the reduction of the lubricating effect by keeping the CNTs away from the counterpart.

Non-trivial friction behaviour is observed in the lower grain size sample which might be related to the enhanced oxidation kinetics and the subsequent breakage of the formed oxide layer.

For low loads (50-100 mN), the main friction mechanism is related to the indentation depth of the dynamic counterpart, whereas for higher loads (200-300 mN) oxidation plus interfacial lubrication is more significant.

The main influence of the CNTs in the friction and wear behaviour is related to the microstructural refinement, which improves both the oxidation kinetics and the mechanical properties of the composites.

A modified Archard model (considering the mean grain size influence) was applied and complemented by a morphological analysis (cutting efficiency) in order to understand the wear mechanisms acting in the process. It was found that for the coarse-grained samples, grain peeling is preponderant, whereas redeposition arises in the refined samples.

IX. Electrical properties: transport and coupling

IX.1. Introduction

The improvement of the electrical properties of metals is a hard task to face. Particularly, in electrical contact materials, composites are not intended to improve these properties as the main goal, but to overcome other issues related to the duty life of the component. For example, in low-voltage relays, Ag-based composites reinforced with ceramic particles are employed nowadays. However, the ceramic reinforcement plays a fundamental role in avoiding contact inter-welding and increased arc dissipation. These obstacles are important enough to relegate other physical properties to the background. It has been demonstrated that the addition of this type of reinforcements reduce the overall electrical and thermal conductivity [16]. Nevertheless, with the increasing tendency towards energy-efficient and reduced-weight materials, the search for a new type of functional reinforcement becomes necessary. As mentioned before, carbon nanotubes possess outstanding intrinsic physical properties, among which we can highlight a great thermal stability (up to 4000 K), chemical stability (reactivity with other components) and thermal conductivity. Regarding the electrical properties, the analysis of the interactions between metal-CNT and CNT-CNT is still unclear in the scientific community. Dissimilar reports regarding the electrical coupling of CNTs can be found, reporting several different effects that might be acting. Due to their low dimensionality, it is theoretically predicted that the conductivity in CNTs (both, thermal and electrical) is ruled by quantum effects [169], whereas from certain experimental investigations it can be inferred that the conduction mechanisms are governed by quasi-ballistic or diffusive mechanisms.

Regarding the electrical properties in CNT/metal composites, the literature provides a low amount of starting information. Xu et al. found that the electrical resistivity was increased for an increasing weight fraction of CNTs (1, 4 and 10 wt.%) in CNT/Al composites up to 94.1% in certain cases [170]. The researchers mentioned the agglomeration of CNTs in the grain boundaries as well as the formation of carbides (specifically, AlC_2), which increment the amount of electron scattering, as the reasons for the resistivity increase. In an attempt to improve the interface and dispersion of CNTs in an Al matrix, Nie et al. produced Mo-coated CNT/Al composites [171]. They observed that the inclusion of these coated CNTs was not able to

improve the electrical conductivity of the composites. The authors blame the low CNT and Mo conductivities (in comparison to Al) and the amount of porosity observed in the composite (up to 5%), being the latter the most probable factor. However, Uddin et al. Also based their explanation of the improvement of the electrical conductivity in SWCNT/bronze and MWCNT/bronze composites on the grain boundary distribution of the CNTs [172]. They measured a 20% improvement for very low CNT concentrations (0.1 wt.%). On the other hand, they were not able to improve Cu-matrix composites even up to 2 CNT wt.%. In electroless-deposited MWCNT/Cu composites, the increase in the electrical resistivity was significant [173]. With volume fractions ranging from 10 to 40 vol.%, the electrical resistivity reached up to 700% of the reference value for pure Cu. Again, the justification is based on the agglomeration of the CNTs on grain boundaries forming an interfacial phase, which is detrimental for the electron transfer. In the case of MWCNT/Ag composites produced by powder metallurgy, the electrical resistivity was increased up to 4.5 times that of pure Ag [121]. For concentrations above 10 vol.%, the increased amount of CNT/metal interfaces coupled with a large amount of porosity (from 12 to 24%) are cited as the cause.

In this case of study, MWCNTs were selected as reinforcements due to the statistical fact that they possess at least one zero-gap layer [11], as opposed to SWCNTs (which might present either metallic or semiconducting behaviour). Thereby, certain unwanted effects can be avoided, such as Schottky barriers (formed at the metal-semiconductor junctions). Also, in MWCNTs the adjacent walls are generally non-commensurate (possessing different chiralities) with a negligible interlayer electronic coupling and could alternate between metallic and semiconducting [174]. MWCNTs show a pseudo-gap in I-V measurements following a power scaling law for conductance, characteristic of a Luttinger liquid. The interlayer coupling in MWCNTs is comparable to graphite (approx. 10 meV) and is inversely proportional to the tube diameter [174]. This interlayer coupling can be easily overcome, since the available thermal energy at room temperature (300 K) exceeds that energy gap ($k_B.T = 25.8$ meV). Another report confirms that the charge transport from an outermost layer to an inner layer is believed to be a tunnel transport and would not be a major issue to overcome [175]. However, several resistance-generating effects are unavoidable in the processing of composites, where interfaces determine the behaviour, such as Coulomb blockades, resonant tunnelling, Fano resonances, etc. Electrical resistance at interfaces is thus of paramount importance, since both matrix and reinforcement are good electrical conductors. Therefore, a seamlessly integrated reinforcement would

theoretically improve the electron transfer, efficiently reducing the energetic losses in the applications.

The electrical properties were studied in composites with 1.0, 2.0, 3.0 and 5.0 wt.% manufactured by colloidal mixing in ethylene glycol and hot uniaxially pressed. The electrical resistivity was determined by means of a 4 point probe device with scanning voltages from 1.0 to 3.0 V DC. The MWCNT cluster distribution of the 1.0 wt.% sample was evaluated with FIB/SEM tomography and the quantitative data of the reconstructed structure was analysed with a commercial software (MAVI). The experimental resistivities were contrasted with well known models in order to assess the arrangement of the CNTs within the composite.

IX.2. Results and discussion

The mean values of the electrical resistivity and their correspondent standard deviation are shown in Table IX-1. An improvement is solely observed for the 1.0 wt.% sample, showing 3.3% lower resistivity than the reference sample. However, for the rest of the samples set, very fluctuant values are observed. The 2.0 and 5.0 wt.% possess resistivities significantly larger than the reference, whereas the 3.0 wt.% only shows a marginal increase of 4.2%. It is worth noting that within the standard deviation of the measurements, samples containing 1.0, 2.0 and 3.0 wt.% showed values lower than the reference. These values are even below the theoretical Ni and attest to the heterogeneity of the sample set. However, the 5.0 wt.% samples were always far above the theoretical Ni value.

Table IX-1 – Experimental values of the electrical resistivity of the composites with different CNT concentrations.

Sample [wt.%/vol.%]	Electrical resistivity [x10^{-8} Ω.m]	Difference to ref. [%]
Pure Ni	8.05 ± 1.60	---
1.0 (6.5)	7.79 ± 3.12	-3.3
2.0 (12.3)	9.87 ± 2.73	22.6
3.0 (17.5)	8.39 ± 4.12	4.2
5.0 (26.5)	16.30 ± 2.74	202.5

The electrical properties of Ni are not significantly affected up to large concentrations (3.0 wt.%). This corresponds to the empirical limit found in chapters V and VI for the microstructural studies and the mechanical properties.

As a complementary analysis, a FIB/SEM tomography on the 1.0 wt.% sample was performed. The objective was to quantitatively analyse the connectivity between the clusters and to assess the probable path an electron would take through the network (Figure IX-1).

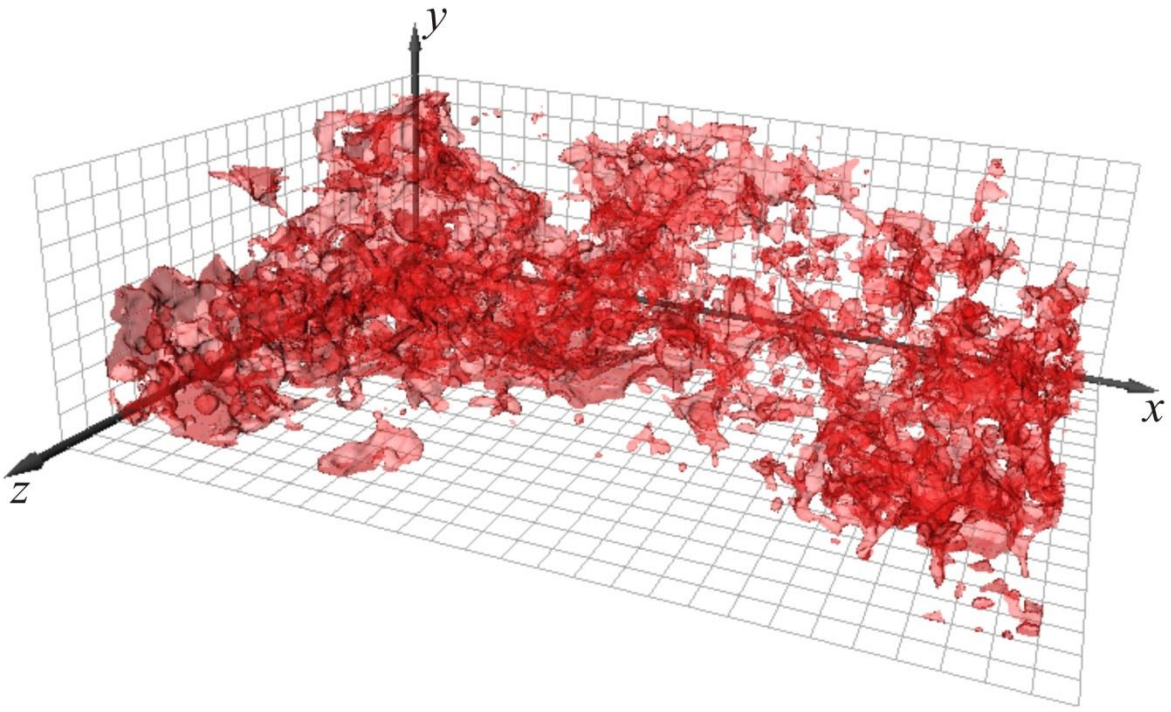

Figure IX-1 – FIB/SEM tomography of the CNT-cluster distribution in a MWCNT/Ni 1.0 wt.% composite. The interconnectivity between the clusters is thus clearly depicted.

Qualitatively, the reconstructed cluster distribution tends towards a random distribution rather than an aligned cluster order. Due to the limitations in resolution and reconstruction in FIB/SEM tomographies, only clusters can be segmented and shown and not the CNTs. The mathematical evaluation is summarised in Table IX-2.

Table IX-2 – Field parameters for a MWCNT/Ni 1.0 wt.% composite, reconstructed after a FIB/SEM tomography.

Direction	Mean geometric tortuosity	Max. geometric tortuosity	Min. geometric tortuosity	Euler number
X	1.00664	1.02469	1	
Y	1.01507	1.11178	1	***− 874***
Z	1.02652	1.21429	1	

The focus was put on two relevant parameters for transport properties (electrical and thermal) such as the Euler number (which represents the interconnectivity between particles) and the geometrical tortuosity (which shows the minimal path an electron would take from one extreme to the other). The Euler number has a strong negative value, representing a strongly interconnected network of particles [176]. Furthermore, the mean geometric tortuosity supports

this assertion by showing values close to one. The combination of these features leads to the assumption that, when an electron is injected into the CNT network, the strong interconnectivity would ensure its movement throughout the system. The only factor that would govern electron mobility would therefore be the inter-tube coupling and the internal scattering.

As already mentioned, the tomography can show the connectivity of the clusters but cannot resolve whether the CNTs are aligned or not within each cluster. Thus, it would be necessary to assess this feature by an alternative mean. In order to try to model and interpret in which way the CNTs affect the electrical properties of the composites, the electrical resistivity was simulated with different amounts of CNTs under different arrangements. The selected models were the Rule of mixtures (ROM) and an Effective Medium Approximation (EMA). ROM is perhaps the most widespread method to model the physical properties of a composite material [177]. Particularly, the axial and transversal arrangements (known as Voigt and Reuss, respectively) are very useful as an initial approximation by defining upper and lower limits for the behaviour of the composite. A schematic representation is shown in Figure IX-2.

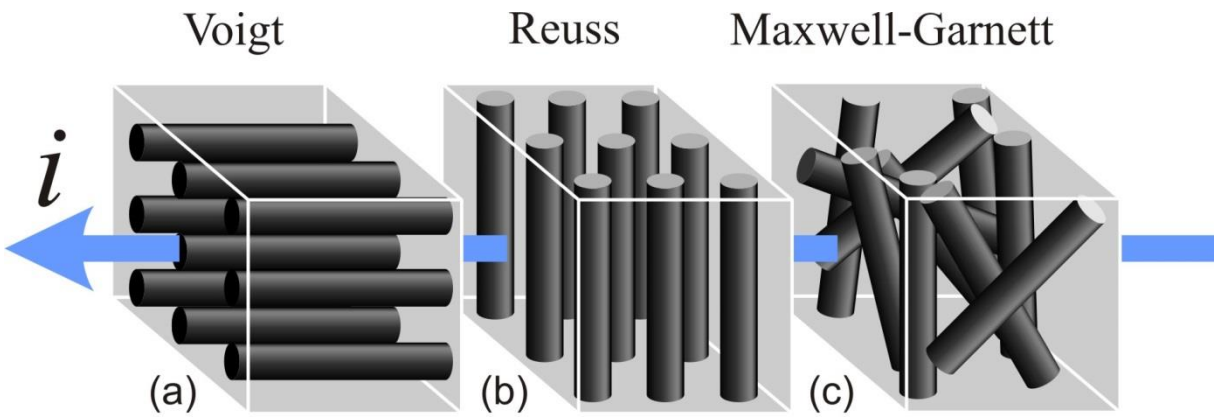

Figure IX-2 – Schematic representation of the upper and lower bounds (Voigt (a) and Reuss (b), respectively) of the rule of mixtures and the EMA model (Maxwell-Garnett (c)). The blue arrow represents the current flow.

The resulting electrical resistivity with the parallel arrangement (Voigt) is calculated by:

$$\rho_c = \left(\frac{f}{\rho_f} + \frac{1-f}{\rho_m}\right)^{-1} \qquad \text{(Equation IX-1)}$$

The resistivity in the transversal arrangement (Reuss) is calculated by:

$$\rho_c = f * \rho_f + (1-f) * \rho_m \qquad \text{(Equation IX-2)}$$

Where ρ_c is the composite's effective resistivity, ρ_f is the resistivity of the CNTs, ρ_m is the resistivity of the matrix material and f the CNT volume fraction. As an intermediate state, the EMA model considers completely random distribution of the second phases within the

composite. The most relevant feature of this model is that the small particles within a continuous matrix are far apart from each other in order to avoid local distortions to the transport characteristics. The Maxwell-Garnett (M-G) is a special case of EMA, particularly suitable for transport phenomena [178].

$$\left(\frac{\rho_c-\rho_m}{\rho_c+2\rho_m}\right) = f\left(\frac{\rho_f-\rho_m}{\rho_f+2\rho_m}\right) \qquad \text{(Equation IX-3)}$$

The used resistivity values for Ni was $6.99\text{x}10^{-8}$ Ω.m [139]. Since the resistivity value of CNTs is still under scrutiny in the community, a theoretical value provided by Hjortstam et al. of $0.35\text{x}10^{-8}$ Ω.m [83] as well as a mean value of those obtained by Ebbesen et al., $2.8\text{x}10^{-6}$ Ω.m, were considered for the modelling [179]. These values differ significantly (3 orders of magnitude) and the lower value is even below the more conductive metals such as Ag ($1.58\text{x}10^{-8}$ Ω.m), Cu ($1.68\text{x}10^{-8}$ Ω.m) and Al ($2.65\text{x}10^{-8}$ Ω.m) [139]. This value (provided by Hjortstam) is even two orders of magnitude lower than in-plane highly ordered pyrolytic graphite (HOPG), which has a resistivity of approximately $4\text{x}10^{-7}$ Ω.m [139]. Therefore, it might be quite an optimistic value for predictions. However, the higher considered value (from Ebbesen), was obtained experimentally and presents a decent correlation to other reported values for MWCNT.

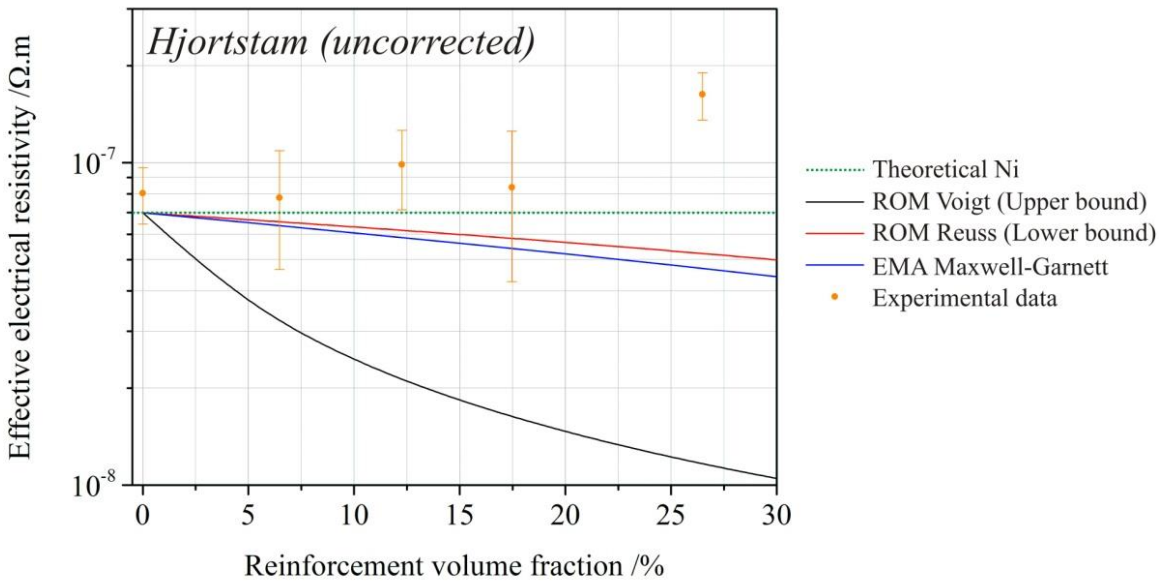

Figure IX-3 – First modelling approach: comparison of different models to the experimental data using the theoretical value for Ni and the CNT resistivity given by Hjortstam.

In a primary evaluation with the value from Hjortstam, a large deviation of the experimental data from the proposed models is observed (Figure IX-3). Moreover, it is noticeable that the

value of pure sintered Ni has a significant deviation from the theoretical value. This is expected since the theoretical value is represented for highly pure, defect-free Ni. In spite of presenting full density, the sintered Ni might have a certain amount of internal oxidation as well as a considerable amount of defects. Therefore, to have a more realistic approximation by the models, the experimental value for pure Ni was used in a second iteration of the modelling. With the new model curves (Figure IX-4), the results still differ from the expected values but are closer to both, the lower bound of the ROM (Reuss) and the EMA model, which represent transversely aligned CNTs and randomly distributed CNTs, respectively.

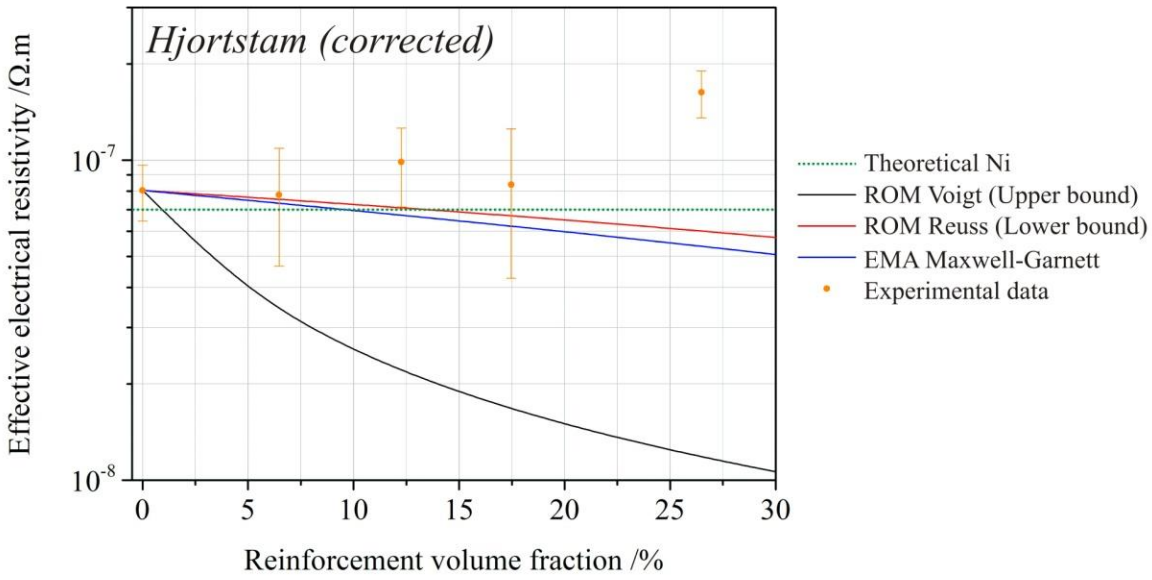

Figure IX-4 - Second modelling approach: comparison of different models to the experimental data using the experimental value for Ni and the CNT resistivity given by Hjortstam.

The third approach was made using the same mathematical models but with the higher CNT resistivity and the experimental value for Ni (8.05×10^{-8} Ω.m) (Figure IX-5). In this case, the experimental data shows an acceptable correlation to the Voigt approximation. It is within the expected behaviour since the measurements were made perpendicular to the pressing direction. The pressing is expected to form orthogonal layers with respect to the applied force. On the other hand, the 5.0 wt.% sample is closer to a random distribution (represented by the M-G model). The significant increase in the resistivity of the 5.0 wt.% sample may be due to the poor wettability of agglomerates to the metallic matrix, as seen in the previous chapters. This would severely hinder the electron injection to the CNT network and thus, the CNT-filled voids would be seen as plain porosity. A good dispersion translates to a homogeneous distribution and an enhancement of the matrix properties facilitating the electrical and thermal transport through

the interface. When the material is designed to work as an electrically conductive material, it is desirable to have the lowest possible porosity.

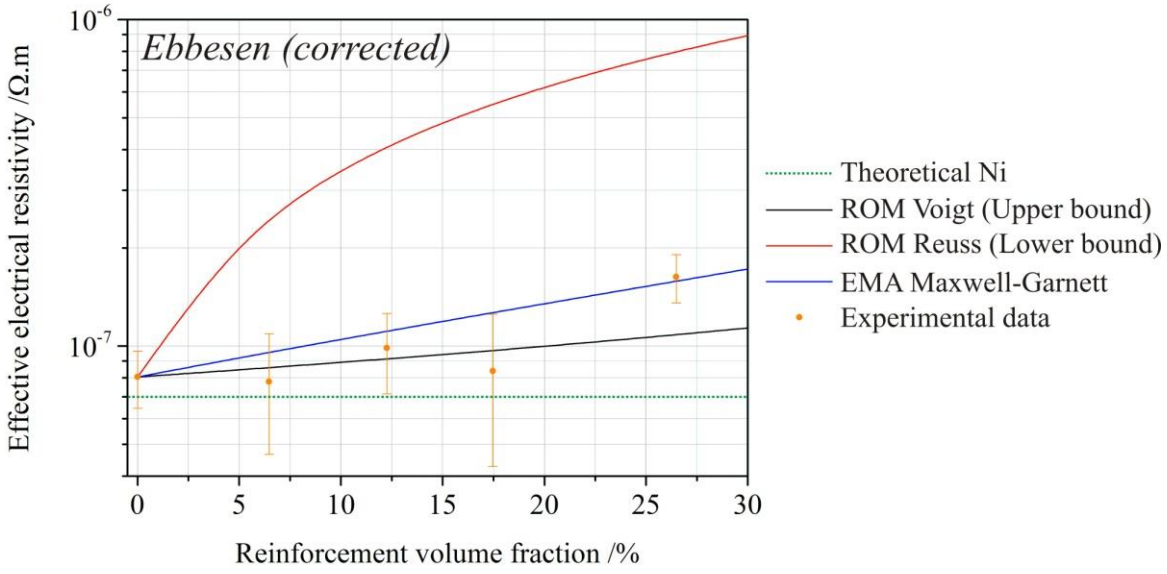

Figure IX-5 - Third modelling approach: comparison of different models to the experimental data using the experimental value for Ni and the experimental CNT resistivity given by Ebbesen.

These models are quite limited and severely underpredict the influence of the interfaces and reagglomeration of the CNTs. After extensive searching in the literature, it was not possible to find a proper model that would adequately consider these neglected features. Furthermore, the actual values of the interfacial resistance between metals and CNTs are still a topic of discussion within the community. A review study on this topic differentiates the contact resistance between MWCNTs and metals in two categories: side-contact and end-contact [180]. The former ranges from 1.7 to 50 kΩ and the latter from 50 to 300 kΩ. A clear conclusion that can be drawn from these values is that electrons in CNT/metal composites would flow through side-contacts instead of end-contacts.

The large resistance on side-contacts may generate a tunnelling barrier with a Coulomb blockade [38]. However, it is expected that in this type of composites, the interfacial area between CNTs and metals is sufficiently large so as to shift the resistance towards the lowest values [38,180]. In case of an optimal coherent contact (full coating of the CNT with metal), the contact resistance is expected to decrease to values that can be directly disregarded [181]. To achieve this, an intimate contact at the open end of each MWCNT must be generated, contacting all walls.

Concerning the MWCNT agglomerates, the literature provides very interesting information that was somehow disregarded in the previous studies in metal/CNT composites. As shown before, all the reports base their discussion in the negative effect of the agglomerates in the electrical conduction. Interestingly, the electrical properties of agglomerates are not as low as to generate such a decrease in the conductivity. For example, Aliev et al. show curves of MWCNT sheets measured in different directions, and their values are still acceptable compared to those of semiconductive, or ceramic reinforcements [47]. Even when the MWCNTs are subjected to highly energetic processing (such as SPS), they tend to form a percolative path through the network with resistivities as low as 10^{-5} Ω.m [182,183].

Contact between CNTs is believed to be governed by quantum resonant effects such as resonant tunnelling or the Fano effect. For a better understanding of these effects, the model can be represented as the electronic coupling between a quantum wire and a quantum dot (Figure IX-6). An electron travelling through the quantum wire can be at a certain moment coupled to an electron within the dot, exciting it and inducing its movement in an orthogonal direction. This coupling implies an energy loss in the original electron, which could be correlated to a diffusive energy lost in transfer.

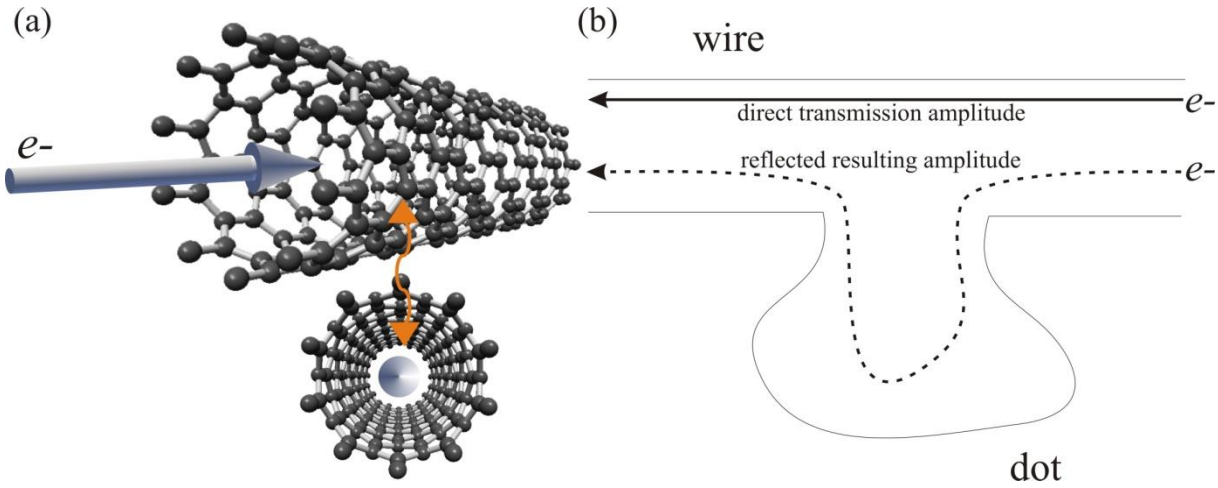

Figure IX-6 – Schematic representation of the resonant tunnelling effect in cross-linked CNTs. It is comparable to the electronic coupling between a quantum wire and a quantum dot.

However, Santini et al. found that the contact resistance in a MWCNT/MWCNT contact was always below the MWCNT/metal contact resistance for all the different nanotube diameters tested, therefore showing great potential to be used as horizontal interconnects [184].

The transfer mechanisms involved at the interface are still a topic of discussion within the community. Some have contacted a single CNT with metal oxides to build a transistor and

analyse the interfacial transport. However, an absolute interfacial resistance, strongly influenced by numerous factors in reported [185]. An issue that is still left to prove is the formation of Schottky barriers in the contact of a metal with a semiconductive graphene layer. Theoretically, Schottky barriers would not be an issue, since the barrier formed between a metal and a semiconducting CNT layer has a width of few nanometres and electrons can tunnel through it [38].

Summarizing, it can be observed that in the study of the electrical behaviour of metal/CNT composites, the participation of CNT agglomerates in the decreased conductivity is usually overestimated. The literature provides very useful information that may lead to think that the main factor ruling the decay in the conductivity would be the detachment of the CNTs (either individual or as agglomerates) from the matrix. This effect would be seen (from an electrical perspective) as porosity, and therefore as a detrimental factor. When working with voltages over a certain threshold (in the mV/V range) coupled with a proper manufacturing technique (high final densities), all the unfavourable effects such as: interfacial resistance, intertube decoupling, interlayer isolation and energy gaps can be straightforwardly overcome, resulting in some cases, in improved electrical conduction.

IX.3. Summary

A reduction in the electrical resistivity of the composites compared to the pure Ni sample was achieved for a 1.0 wt.% concentration. The 2.0 and 3.0 wt.% samples showed a marginal increase, whereas the 5.0 wt.% sample significantly exceeded the Ni reference (approximately 200 %). Contrary to what is reported in the literature, the MWCNT agglomeration does not play a fundamental role in the decrease of the conductivity as does cohesion to the matrix. This is observed particularly in the 5.0 wt.% sample, where the MWCNTs do not show a proper contact to the matrix. The comparison to well-known models was useful to interpret how the MWCNTs are ordered in relationship to the electrical current flow. As expected, the 1.0, 2.0 and 3.0 wt.% samples have MWCNT networks aligned with the current flow (orthogonal plane to the applied force during sintering). In the largest evaluated concentration, the most suitable model describes a totally random distribution, which could be correlated to unordered agglomerates. The presented results might be helpful as a first assessment for the future utilisation of such composites in electrical (contact materials) or electronic (packaging materials) applications.

X. Concluding remarks and outlook

X.1. Concluding remarks

The present work demonstrates the possibility to successfully produce bulk MWCNT/Ni composites via powder metallurgy with near full final densities and enhanced mechanical, thermomechanical, tribological and electrical properties.

This was achieved by the development of a straightforward production method for the manufacturing of the composites without the need for covalent CNT functionalisation that would hinder their outstanding intrinsic physical properties. Studies presented in chapter IV showed that after the processing and blending of the precursors, CNTs conserve their structure. Moreover, a chemical and structural assessment demonstrated (in contrast to what can be found in the literature) that there is no detectable carbide formation due to CNT degradation, despite the amount of initial defects.

In chapter V, the microstructural evolution throughout sintering was simulated and evaluated in a high temperature chamber by performing in-situ X-ray diffraction. It was observed that the grain growth can be hindered by the presence of dispersed CNTs, up to a certain concentration (between 2.0 and 3.0 wt.%). Moreover, the porosity also plays a role in the growth hindrance by migration to grain boundaries during densification. Furthermore, it was possible to observe the influence of agglomerates on the growth kinetics, concluding that the samples with less CNT agglomerates present a faster growth. This is because the CNTs act during growth as fast heat transport paths, accelerating the growth.

Chapter VI dealt with the thermomechanical behaviour of the composites. An improved performance was obtained, showing a maximal CTE reduction of about 76%, achieved with 1.0 wt.% MWCNT samples. This improvement was also observed for other matrix materials (Cu, Al, etc.) and is attributed to an anchoring effect of the CNTs on the matrix. The absolute value of the thermal expansion is comparable to certain low-expansion materials such as Al_2O_3, Si or glass. However, the anchoring behaviour disappears at a certain temperature (approx. 450 °C) with higher amounts of CNTs. Over this temperature, a detachment of the MWCNT from the matrix is observed added to important bloating (expansion of pores due to evaporation of remaining solvent). For larger CNT concentrations (5.0 wt.%), bloating governs the thermal expansion.

The so-called anchoring effect together with the very low or even negative expansion coefficient of the CNTs have been mentioned countless times in the literature as responsible for the improved thermomechanical behaviour in CNT-reinforced composites. In this sense, after the experimental evaluation of the Ni lattice in thermal cycles, this work proposes three main mechanisms which may explain the anchoring effect and are based on the over-expansion of the lattice and the lateral displacement absorption of the CNTs.

The influence of the CNTs on the mechanical properties of the composites was evaluated and discussed in chapter VII. Improved mechanical properties were observed due to microstructural refinement. Correlated to what was explained in chapter V, the CNTs anchor the grain boundaries during growth up to certain concentrations, beyond which no further refinement is observed. Unlike in the CPS samples studied in chapter V, the limit was found to be at 3.0 wt.%. This is due to differences in the mass transport during the sintering process, which tends to agglomerate the previously dispersed CNTs. Thus, the empirical limit for achieving a good distribution and therefore good properties in HUP samples was set at 3.0 wt.% (17.5 vol.%.). The Hall-Petch relationship is confirmed for the composites, regardless of the relative CNT amount. Despite this fact, it must be clarified that Hall-Petch is probably not the only enhancing mechanism present; a load transfer from the matrix to the reinforcements might also be expected. Furthermore, since the microstructure affects all the physical properties, it is important to find a simple way to predict the final microstructure. In this regard, a refinement prediction equation was proposed for the MWCNT/Ni bulk system based on a modified Zener drag model considering the CNT geometry. The proposed model was validated with experimental values.

Another important characteristic for both, structural and functional composites is the tribological (wear and friction) behaviour. In this case, improved tribological behaviour was observed for the composites. The presented results are helpful to approach an elucidation of certain aspects of the friction and wear behaviour of these CNT-reinforced bulk composites. It can be concluded that the influence of the CNTs has two effects:

- Microstructural refinement modifies the oxidation kinetics, thus generating an oxidation wear mechanism; grain boundary strengthening increases the hardness of the material. Moreover, a carbon film was detected by Raman spectroscopy on the wear track, evidencing the intervention of the CNTs in the friction as an interfacial layer which may act as a friction-reducing agent.

- At high loads on the samples with higher CNT (friction) activity, (higher CPS I_D/I_G ratio, i.e. more active CNTs) they might act as an interfacial layer which performs as a lubrication medium.

Non-trivial friction behaviour is observed in the lower grain size sample which might be related to the enhanced oxidation kinetics and the subsequent breakage of the formed oxide layer. For low loads (50-100 mN), the main friction mechanism is related to the indentation depth of the dynamic counterpart, whereas for higher loads (200-300 mN) oxidation plus interfacial lubrication is more significant. It was found that the main acting influence of the CNTs is on the final microstructure, affecting the mechanical properties and the tribochemistry of the surfaces. As it is well known in the tribology community, the friction behaviour is a combination of effects which cannot be analysed separately. Regarding the wear behaviour, the composites showed improved wear resistance as confirmed by a reduction in the wear volume. In order to understand the acting wear mechanisms, a modified Archard equation (considering the mean grain size influence) and complemented by a morphological analysis (cutting efficiency) was utilised for the interpretation of the obtained data. It was found that for the coarse-grained samples, grain peeling is preponderant, whereas redeposition arises in the refined samples.

The final chapter deals with the electrical properties of the composites. The electrical properties show a marginal improvement compared to the Ni reference. A reduction in the electrical resistivity of the composites compared to the pure Ni sample was achieved for 1.0 wt.%. However, 2.0 and 3.0 wt.% samples showed a resistivity increase, and the 5.0 wt.% sample significantly exceeded the Ni reference (approximately 200 %). It was observed that MWCNT agglomeration does not play a fundamental role in the decrease of the conductivity, rather cohesion to the matrix. This is observed particularly in the 5.0 wt.% sample, where the MWCNTs do not show a proper contact to the matrix. From the comparison to well-known models it was observed, as expected, that the 1.0, 2.0 and 3.0 wt.% samples have MWCNT networks aligned with the current flow (orthogonal to the applied force during sintering). In the 5.0 wt.%, the most suitable model was Maxwell-Garnett, which describes a totally random distribution, correlated to unordered agglomerates.

X.2. Outlook

The developed knowledge and obtained results in this work may serve as a starting point for the further development of MWCNT/metal composites. Their potential application field is quite

wide ranging from contact electrodes to electronic packaging materials. For the former, there are still certain typical characterisation procedures that may elucidate the suitability of these composites, but were left outside of the scope of this thesis. Particularly, a first approach with the aim of determining the thermal properties of the composites was performed. The preliminary results showed a 21% enhancement of the thermal diffusivity values compared to that of pure Ni (Table X-1). It is important to remember that the higher the thermal diffusivity, the faster the propagation of heat through the medium is. This is of paramount importance in electrical contacts, since it would reduce the exposure time to the heat input during the electrical discharge in break operations. Furthermore, when compared to commercial electrode composites, it is observed that the thermal diffusivity of the MWCNT/Ni composites is within the same range. This was difficult to foresee, since the matrix material in commercial composites is Ag, which possesses a thermal diffusivity one order of magnitude larger than pure Ni. An extended study of this property is thus recommended, incorporating different MWCNT partial concentrations to the analysis.

Table X-1 – Thermal diffusivity values of MWCNT/Ni composites, commercial electrode materials and pure metals determined by pulsed thermography.

Sample	Thermal diffusivity [mm^2/s]
Pure Nickel	33 ± 5
MWCNT/Ni 1.0 % HUP	40 ± 5
$AgSnO_2$ 88/12 SPW	45 ± 5
$AgSnO_2$ 90/10 SP	43 ± 7
$AgSnO_2$ 90/10 SPW	71 ± 7
Copper (theoretical)	111
Silver (theoretical)	166
Iron (theoretical)	23

Preliminary low voltage DC (30V) arcing tests were also performed on the composites as a first assessment of the interaction of the electrical arc with the electrode. Two main initial conclusions can be assessed:

The MWCNTs were able to overcome the intense electrical discharge (Figure X-1). This is a major attribute, considering the high temperatures and aggressive atmospheres to which the material is subjected.

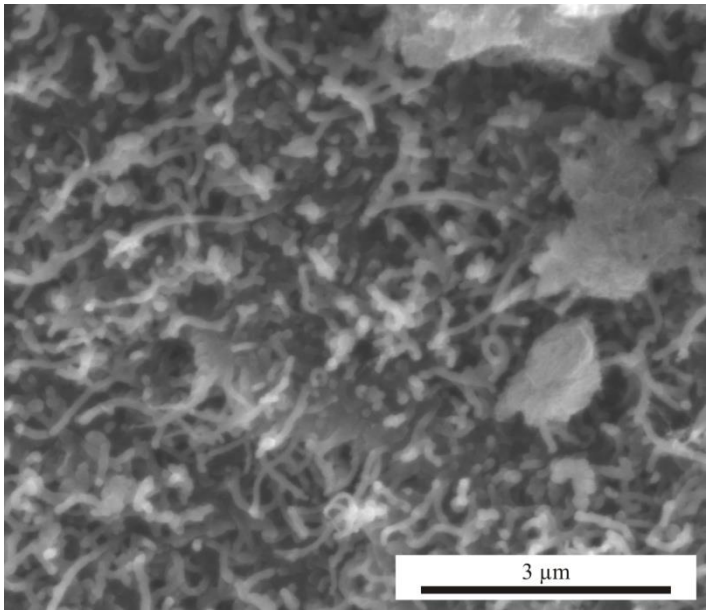

Figure X-1 – SEM image of the interior region in an electrically discharged surface of a MWCNT/Ni 1.0 wt.% composites. The MWCNTs are still noticeable.

The crater morphology shows a shallow surface and certain carbon-containing spots are noticed (Figure X-2). Also, the arc wandering can be identified as an important characteristic to take into consideration. If the arc describes a large path during the discharge time, the energy input would be more efficiently distributed on the surface, reducing damage.

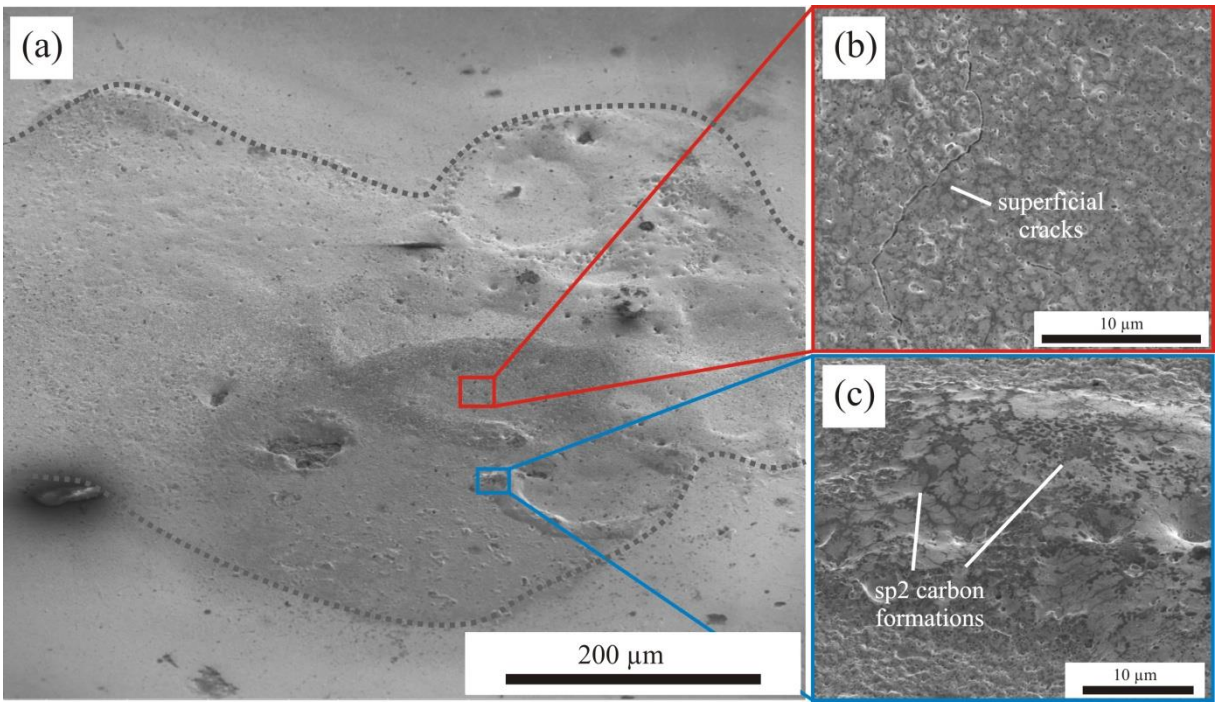

Figure X-2 – Electrical erosion crater on a MWCNT/Ni 1.0 wt.% composite. (a) General view, (b) and (c) detailed view of superficial cracks and carbonaceous forms on the crater surface.

However, there were certain undesired effects observed within the crater. Particularly, superficial cracks are detected at certain spots (Figure X-2b) and sub-superficial porosity generated during arcing (Figure X-3). The formation of porosity during the electrical discharge is related to the uncontrolled diffusion of oxygen and other gases during the exposure time as well as desorption of gases previously present in the composite (deficient solvent evaporation during processing, etc.)

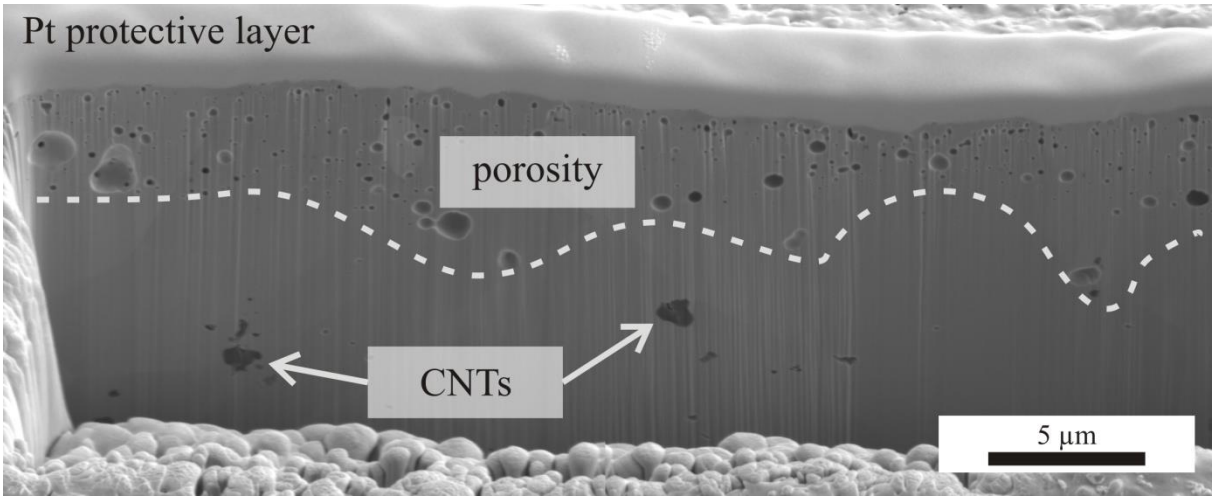

Figure X-3 – SEM/FIB cross section of the internal region of the crater. The region of increased porosity is separated with a dashed line. The Pt layer on top of the cross section avoids FIB artefacts.

These two effects may influence the response of the composite under arcing in extended make-break operations and its consequent duty life. Deeper analysis is therefore necessary to improve the material design so as to overcome the presence of these two drawbacks.

Additional studies are still missing regarding the evaluation of the contact resistance of the electrodes (crucial for the understanding in the molten bridge formation and energy loss assessment), the material transfer during arcing and Raman characterisation of the CNTs in the final state, among others.

XI. References

[1] R. Dell, Batteries fifty years of materials development, Solid State Ionics. 134 (2000) 139–158.

[2] U. Köhler, C. Antonius, P. Bäuerlein, Advances in alkaline batteries, J. Power Sources. 127 (2004) 45–52.

[3] Source Book on Industrial Alloy and Engineering Data, 1st ed., American Society For Metals, ASM Metals Park, OH, 1978.

[4] K. Sawa, K. Yoshida, M. Watanabe, K. Suzuki, Arc Characteristics and Electrode Mass Change of AgNi Contacts for Electromagnetic Contactors, Proc. 56th IEEE Holm Conf. Electr. Contacts. (2010) 1–6.

[5] S. Iijima, Helical microtubules of graphitic carbon, Nature. 354 (1991) 56–58.

[6] A. Jorio, M.S. Dresselhaus, G. Dresselhaus, Carbon Nanotubes - Advanced topics in the synthesis, structure, properties and applications, Springer Verlag, Berlin-Heidelberg, 2008.

[7] M. Terrones, Science and Technology of the Twenty-First Century: Synthesis, Properties, and Applications of Carbon Nanotubes, Annu. Rev. Mater. Res. 33 (2003) 419–501.

[8] P. Kim, L. Shi, a. Majumdar, P. McEuen, Thermal Transport Measurements of Individual Multiwalled Nanotubes, Phys. Rev. Lett. 87 (2001) 19–22.

[9] S. Berber, Y. Kwon, D. Tomanek, Unusually high thermal conductivity of carbon nanotubes, Phys. Rev. Lett. 84 (2000) 4613–6.

[10] D. Vollath, Nanomaterials: An Introduction to Synthesis, Properties and Applications, Wiley-VCH, 2008.

[11] J. Robertson, G. Zhong, S. Hofmann, B.C. Bayer, C.S. Esconjauregui, H. Telg, et al., Use of carbon nanotubes for VLSI interconnects, Diam. Relat. Mater. 18 (2009) 957–962.

[12] D.B. Miracle, S.L. Donaldson, ASM Handbook, Vol. 21 Composites, ASM International, Metals Park, OH, USA, 2001.

[13] M. Meyers, K.K. Chawla, Mechanical Behavior of Materials, 2nd ed., Cambridge University Press, Cambridge, UK, 2009.

[14] T. Clyne, P. Withers, An introduction to metal matrix composites, 1st ed., Cambridge University Press, Cambridge, UK, 1995.

[15] J. Hale, Boeing 787 from the ground up, AERO Mag. (2006) 17–23.

[16] N. Jeanvoine, a. Velichko, C. Selzner, F. Mücklich, Nanotomography of electrical contacts – new insights by high resolution 3D analysis of local material degradation, Eur. Phys. J. Appl. Phys. 49 (2009) 22907.

[17] C. Selzner, N. Jeanvoine, a. Velichko, F. Mücklich, Untersuchung des Erosionsverhaltens von silberbasierten Kontaktwerkstoffen mittels FIB-Techniken, Materwiss. Werksttech. 39 (2008) 936–939.

[18] S. Kang, Sintering: densification, grain growth & microstructure, 1st ed., Elsevier Butterworth-Heinemann, Oxford, UK, 2005.

[19] F. Swinkels, D. Wilkinson, E. Arzt, Mechanisms of hot-isostatic pressing, Acta Metall. 31 (1983) 1829–1840.

[20] V. Mamedov, Spark plasma sintering as advanced PM sintering method, Powder Metall. 45 (2002) 322–328.

[21] M. Omori, Sintering, consolidation, reaction and crystal growth by the spark plasma system (SPS), Mater. Sci. Eng. A. 287 (2000) 183–188.

[22] H. Pierson, Handbook of carbon, graphite, diamond and fullerenes, 1st ed., Noyes Publications, Park Ridge, NJ, 1993.

[23] M.S. Dresselhaus, G. Dresselhaus, P. Avouris, Carbon Nanotubes, 1st ed., Springer Verlag, Berlin-Heidelberg, 2003.

[24] S. Reich, C. Thomsen, J. Maultzsch, Carbon Nanotubes: Basic Concepts and Physical Properties, 1st ed., Wiley-VCH, Weinheim, Germany, 2004.

[25] A. McNaught, A. Wilkinson, IUPAC Compendium of chemical terminology, 2012.

[26] E.T. Thostenson, Z. Ren, T.-W. Chou, Advances in the science and technology of carbon nanotubes and their composites: a review, Compos. Sci. Technol. 61 (2001) 1899–1912.

[27] Y. Gogotsi, Carbon Nanomaterials, Taylor & Francis Group, LLC, Boca Raton, FL., 2006.

[28] M.S. Dresselhaus, G. Dresselhaus, A. Jorio, Unusual Properties and Structure of Carbon Nanotubes, Annu. Rev. Mater. Res. 34 (2004) 247–278.

[29] M. Ahlskog, P. Hakonen, M. Paalanen, L. Roschier, R. Tarkiainen, Multiwalled carbon nanotubes as building blocks in nanoelectronics, J. Low Temp. Phys. 124 (2001) 335–352.

[30] J. Kim, K. Kang, J.-O. Lee, K.-H. Yoo, J.-R. Kim, J.W. Park, et al., Correlated Electrical Transport through Multiwall Carbon Nanotubes in a Crossed Geometry, J. Phys. Soc. Japan. 70 (2001) 1464–1467.

[31] S. Roche, F. Triozon, A. Rubio, D. Mayou, Electronic conduction in multi-walled carbon nanotubes: role of intershell coupling and incommensurability, Phys. Lett. A. 285 (2001) 94–100.

[32] M. Kida, T. Mihara, K. Miyamoto, S. Harada, T. Sasaki, N. Aoki, et al., Quantum Transport in Nano-Space at the Cross-Junction of Multi-Walled Carbon Nano-Tubes, Proc. 2nd Quantum Transp. Nano-Hana Int. Work. IPAP Conf. Ser. 5 (2004) 61–64.

[33] P. Delaney, M. Di Ventra, S.T. Pantelides, Quantized conductance of multiwalled carbon nanotubes, Appl. Phys. Lett. 75 (1999) 3787.

[34] L. Langer, V. Bayot, E. Grivei, J. Issi, J. Heremans, C. Olk, et al., Quantum transport in a multiwalled carbon nanotube., Phys. Rev. Lett. 76 (1996) 479–482.

[35] P. Poncharal, S. Frank, Z.L. Wang, W. a. de Heer, Conductance quantization in multiwalled carbon nanotubes, Eur. Phys. J. D. 9 (1999) 77–79.

[36] B.Q. Wei, R. Vajtai, P.M. Ajayan, Reliability and current carrying capacity of carbon nanotubes, Appl. Phys. Lett. 79 (2001) 1172.

[37] W. Zhu, E. Kaxiras, Schottky barrier formation at a carbon nanotube—metal junction, Appl. Phys. Lett. 89 (2006) 243107.

[38] F. Banhart, Interactions between metals and carbon nanotubes: at the interface between old and new materials., Nanoscale. 1 (2009) 201–13.

[39] Y. Lu, P.K. Liaw, The mechanical properties of nanostructured materials, JOM. 53 (2001) 31–35.

[40] M. Treacy, T. Ebbesen, Exceptionally high Young's modulus observed for individual carbon nanotubes, Nature. 381 (1996) 678–680.

[41] A. Krishnan, E. Dujardin, T. Ebbesen, P. Yianilos, M. Treacy, Young's modulus of single-walled nanotubes, Phys. Rev. B. 58 (1998) 14013–14019.

[42] B.. Demczyk, Y.. Wang, J. Cumings, M. Hetman, W. Han, a Zettl, et al., Direct mechanical measurement of the tensile strength and elastic modulus of multiwalled carbon nanotubes, Mater. Sci. Eng. A. 334 (2002) 173–178.

[43] F. Li, H.M. Cheng, S. Bai, G. Su, M.S. Dresselhaus, Tensile strength of single-walled carbon nanotubes directly measured from their macroscopic ropes, Appl. Phys. Lett. 77 (2000) 3161.

[44] M. Yu, B. Files, S. Arepalli, R. Ruoff, Tensile loading of ropes of single wall carbon nanotubes and their mechanical properties, Phys. Rev. Lett. 84 (2000) 5552–5.

[45] J. Che, T. Cagin, W. Goddard, Thermal conductivity of carbon nanotubes, Nanotechnology. 11 (2000) 65–69.

[46] J. Hone, M. Whitney, C. Piskoti, a. Zettl, Thermal conductivity of single-walled carbon nanotubes, Phys. Rev. B. 59 (1999) R2514–R2516.

[47] A.E. Aliev, C. Guthy, M. Zhang, S. Fang, A. a. Zakhidov, J.E. Fischer, et al., Thermal transport in MWCNT sheets and yarns, Carbon. 45 (2007) 2880–2888.

[48] J. Hilding, E. a. Grulke, Z. George Zhang, F. Lockwood, Dispersion of Carbon Nanotubes in Liquids, J. Dispers. Sci. Technol. 24 (2003) 1–41.

[49] N. Komatsu, F. Wang, A Comprehensive Review on Separation Methods and Techniques for Single-Walled Carbon Nanotubes, Materials (Basel). 3 (2010) 3818–3844.

[50] S.D. Bergin, Z. Sun, D. Rickard, P. V Streich, J.P. Hamilton, J.N. Coleman, Multicomponent solubility parameters for single-walled carbon nanotube-solvent mixtures., ACS Nano. 3 (2009) 2340–50.

[51] S.R. Bakshi, R.G. Batista, A. Agarwal, Quantification of carbon nanotube distribution and property correlation in nanocomposites, Compos. Part A Appl. Sci. Manuf. 40 (2009) 1311–1318.

[52] P. Buffat, Size effect on the melting temperature of gold particles, Phys. Rev. A. 13 (1976).

[53] A. Agarwal, S. Bakshi, D. Lahiri, Carbon nanotubes: reinforced metal matrix composites, CRC Press, Boca Raton, FL., 2011.

[54] E. Carreño-Morelli, J. Yang, E. Couteau, K. Hernadi, J.W. Seo, C. Bonjour, et al., Carbon nanotube/magnesium composites, Phys. Status Solidi. 201 (2004) R53–R55.

[55] A.M.K. Esawi, K. Morsi, A. Sayed, M. Taher, S. Lanka, Effect of carbon nanotube (CNT) content on the mechanical properties of CNT-reinforced aluminium composites, Compos. Sci. Technol. 70 (2010) 2237–2241.

[56] A.M.K. Esawi, K. Morsi, A. Sayed, M. Taher, S. Lanka, The influence of carbon nanotube (CNT) morphology and diameter on the processing and properties of CNT-

reinforced aluminium composites, Compos. Part A Appl. Sci. Manuf. 42 (2011) 234–243.

[57] M. Jafari, M.H. Abbasi, M.H. Enayati, F. Karimzadeh, Mechanical properties of nanostructured Al2024–MWCNT composite prepared by optimized mechanical milling and hot pressing methods, Adv. Powder Technol. 23 (2012) 205–210.

[58] J. Stein, B. Lenczowski, N. Fréty, E. Anglaret, Mechanical reinforcement of a high-performance aluminium alloy AA5083 with homogeneously dispersed multi-walled carbon nanotubes, Carbon. 50 (2012) 2264–2272.

[59] A.S. Bolokang, M.J. Phasha, Thermal analysis on the curie temperature of nanocrystalline Ni produced by ball milling, Adv. Powder Technol. 22 (2011) 518–521.

[60] S.I. Cha, K.T. Kim, S.N. Arshad, C.B. Mo, S.H. Hong, Extraordinary Strengthening Effect of Carbon Nanotubes in Metal-Matrix Nanocomposites Processed by Molecular-Level Mixing, Adv. Mater. 17 (2005) 1377–1381.

[61] X. Yang, C. Shi, C. He, E. Liu, J. Li, N. Zhao, Synthesis of uniformly dispersed carbon nanotube reinforcement in Al powder for preparing reinforced Al composites, Compos. Part A Appl. Sci. Manuf. 42 (2011) 1833–1839.

[62] J.Y. Hwang, B.K. Lim, J. Tiley, R. Banerjee, S.H. Hong, Interface analysis of ultra-high strength carbon nanotube/nickel composites processed by molecular level mixing, Carbon. 57 (2013) 282–287.

[63] K. Chu, H. Guo, C. Jia, F. Yin, X. Zhang, X. Liang, et al., Thermal properties of carbon nanotube-copper composites for thermal management applications., Nanoscale Res. Lett. 5 (2010) 868–74.

[64] S.I. Cha, K.T. Kim, K.H. Lee, C.B. Mo, S.H. Hong, Strengthening and toughening of carbon nanotube reinforced alumina nanocomposite fabricated by molecular level mixing process, Scr. Mater. 53 (2005) 793–797.

[65] A. Islam, B. Chowdhry, M. Snowden, Heteroaggregation in colloidal dispersions, Adv. Colloid Interface Sci. 62 (1995) 109–136.

[66] P. Kralchevsky, K. Danov, N. Denkov, Chemical physics of colloid systems and interfaces, in: K. Birdi (Ed.), Surf. Colloid Chem., CRC Press, 2008: pp. 197–377.

[67] A. Stone, D. Wales, Theoretical studies of icosahedral C60 and some related species, Chem. Phys. Lett. 128 (1986) 501–503.

[68] J. Ma, D. Alfè, A. Michaelides, E. Wang, Stone-Wales defects in graphene and other planar sp2-bonded materials, Phys. Rev. B. 80 (2009) 1–4.

[69] H.J. Choi, J.H. Shin, D.H. Bae, The effect of milling conditions on microstructures and mechanical properties of Al/MWCNT composites, Compos. Part A Appl. Sci. Manuf. 43 (2012) 1061–1072.

[70] L. Ci, Z. Ryu, N.Y. Jin-Phillipp, M. Rühle, Investigation of the interfacial reaction between multi-walled carbon nanotubes and aluminum, Acta Mater. 54 (2006) 5367–5375.

[71] H. Kwon, M. Estili, K. Takagi, T. Miyazaki, A. Kawasaki, Combination of hot extrusion and spark plasma sintering for producing carbon nanotube reinforced aluminum matrix composites, Carbon. 47 (2009) 570–577.

[72] H. Kwon, D.H. Park, J.F. Silvain, A. Kawasaki, Investigation of carbon nanotube reinforced aluminum matrix composite materials, Compos. Sci. Technol. 70 (2010) 546–550.

[73] X. Zhang, H. Wei, A. Li, Y. Fu, L. Geng, Effect of hot extrusion and heat treatment on CNTs–Al interfacial bond strength in hybrid aluminium composites, Compos. Interfaces. 20 (2013) 231–239.

[74] H.J. Choi, J.H. Shin, D.H. Bae, Grain size effect on the strengthening behavior of aluminum-based composites containing multi-walled carbon nanotubes, Compos. Sci. Technol. 71 (2011) 1699–1705.

[75] H.J. Choi, B.H. Min, J.H. Shin, D.H. Bae, Strengthening in nanostructured 2024 aluminum alloy and its composites containing carbon nanotubes, Compos. Part A Appl. Sci. Manuf. 42 (2011) 1438–1444.

[76] D. Lahiri, V. Singh, A.K. Keshri, S. Seal, A. Agarwal, Carbon nanotube toughened hydroxyapatite by spark plasma sintering: Microstructural evolution and multiscale tribological properties, Carbon. 48 (2010) 3103–3120.

[77] C. Edtmaier, T. Janhsen, R.C. Hula, L. Pambaguian, H.G. Wulz, S. Forero, et al., Carbon Nanotubes as Highly Conductive Nano-Fillers in Metallic Matrices, Adv. Mater. Res. 59 (2009) 131–137.

[78] S. Cho, K. Kikuchi, T. Miyazaki, K. Takagi, Multiwalled carbon nanotubes as a contributing reinforcement phase for the improvement of thermal conductivity in copper matrix composites, Scr. Mater. 63 (2010) 375–378.

[79] S. Cho, K. Kikuchi, A. Kawasaki, On the role of amorphous intergranular and interfacial layers in the thermal conductivity of a multi-walled carbon nanotube–copper matrix composite, Acta Mater. 60 (2012) 726–736.

[80] S. Arai, M. Endo, T. Sato, A. Koide, Fabrication of Nickel–Multiwalled Carbon Nanotube Composite Films with Excellent Thermal Conductivity by an Electrodeposition Technique, Electrochem. Solid-State Lett. 9 (2006) C131.

[81] J.Y. Hwang, A.R.P. Singh, R. Banerjee, J. Tiley, T.Y. Choi, Processing and Thermal Conductivity of Carbon Nanotube-Reinforced Nickel Matrix Composites, in: ASME Summer Heat Transf. Conf. 2009, ASME, 2009: pp. 627–630.

[82] S. Yamanaka, R. Gonda, A. Kawasaki, H. Sakamoto, Y. Mekuchi, M. Kuno, et al., Fabrication and Thermal Properties of Carbon Nanotube/Nickel Composite by Spark Plasma Sintering Method, Mater. Trans. 48 (2007) 2506–2512.

[83] O. Hjortstam, P. Isberg, S. Söderholm, H. Dai, Can we achieve ultra-low resistivity in carbon nanotube-based metal composites?, Appl. Phys. A Mater. Sci. Process. 78 (2004) 1175–1179.

[84] J. Kim, J.-R. Kim, J.-O. Lee, J. Park, H. So, N. Kim, et al., Fano Resonance in Crossed Carbon Nanotubes, Phys. Rev. Lett. 90 (2003) 1–4.

[85] H. Yang, J. Chen, L. Yang, J. Dong, Electronic transport and Fano resonance in crossed carbon nanotubes, Phys. Rev. B. 71 (2005) 2–5.

[86] S.K. Biswas, L.J. Schowalter, Y.J. Jung, A. Vijayaraghavan, P. Ajayan, R. Vajtai, Room-temperature resonant tunneling of electrons in carbon nanotube junction quantum wells, Appl. Phys. Lett. 86 (2005) 183101.

[87] J. Knoch, J. Appenzeller, Tunneling phenomena in carbon nanotube field-effect transistors, Phys. Status Solidi. 205 (2008) 679–694.

[88] J. Sun, L. Gao, W. Li, Colloidal processing of carbon nanotube/alumina composites, Chem. Mater. 14 (2002) 5169–5172.

[89] F. Inam, H. Yan, M.J. Reece, T. Peijs, Dimethylformamide: an effective dispersant for making ceramic-carbon nanotube composites., Nanotechnology. 19 (2008) 195710.

[90] F. Lasserre, Noble metal coatings of multiwalled carbon nanotubes, Saarland University, 2011.

[91] J. Decker, A.H. Walker, K. Bosnick, Sample preparation protocols for realization of reproducible characterization of single-wall carbon nanotubes, Metrologia. 46 (2009) 682–692.

[92] J. Stein, AA5083 Aluminium Alloys Reinforced with Multi-walled Carbon Nanotubes: Microstructure and Mechanical Properties, Universite Montpellier 2, 2012.

[93] S. Tjong, Carbon nanotube reinforced composites - Metal and ceramic matrices, Wiley-VCH, Weinheim, Germany, 2009.

[94] P.-C. Ma, N. a. Siddiqui, G. Marom, J.-K. Kim, Dispersion and functionalization of carbon nanotubes for polymer-based nanocomposites: A review, Compos. Part A Appl. Sci. Manuf. 41 (2010) 1345–1367.

[95] T.J. Simmons, D. Hashim, R. Vajtai, P. Ajayan, Large area-aligned arrays from direct deposition of single-wall carbon nanotube inks., J. Am. Chem. Soc. 129 (2007) 10088–9.

[96] J.Y. Hwang, A.R.P. Singh, M. Chaudhari, J. Tiley, Y. Zhu, J. Du, et al., Templated Growth of Hexagonal Nickel Carbide Nanocrystals on Vertically Aligned Carbon Nanotubes, J. Phys. Chem. C. 114 (2010) 10424–10429.

[97] L. Yue, R. Sabiryanov, E. Kirkpatrick, Magnetic properties of disordered Ni3C, Phys. Rev. B. 62 (2000) 8969–8975.

[98] J.-L. Tsai, T.-C. Lu, Investigating the load transfer efficiency in carbon nanotubes reinforced nanocomposites, Compos. Struct. 90 (2009) 172–179.

[99] M.M. Shokrieh, R. Rafiee, Investigation of nanotube length effect on the reinforcement efficiency in carbon nanotube based composites, Compos. Struct. 92 (2010) 2415–2420.

[100] R.A. DiLeo, B.J. Landi, R.P. Raffaelle, Purity assessment of multiwalled carbon nanotubes by Raman spectroscopy, J. Appl. Phys. 101 (2007) 064307.

[101] J.H. Lehman, M. Terrones, E. Mansfield, K.E. Hurst, V. Meunier, Evaluating the characteristics of multiwall carbon nanotubes, Carbon. 49 (2011) 2581–2602.

[102] M. a Pimenta, G. Dresselhaus, M.S. Dresselhaus, L.G. Cançado, A. Jorio, R. Saito, Studying disorder in graphite-based systems by Raman spectroscopy., Phys. Chem. Chem. Phys. 9 (2007) 1276–91.

[103] K.I. Tserpes, P. Papanikos, The effect of Stone–Wales defect on the tensile behavior and fracture of single-walled carbon nanotubes, Compos. Struct. 79 (2007) 581–589.

[104] X. Zhao, Y. Ando, L.L.-C. Qin, H. Kataura, Y. Maniwa, R. Saito, Multiple splitting of G-band modes from individual multiwalled carbon nanotubes, Appl. Phys. Lett. 81 (2002) 2550.

[105] M. Singleton, P. Nash, The C-Ni (Carbon-Nickel) system, Bull. Alloy Phase Diagrams. 10 (1989) 121–126.

[106] Thermo-Calc: Thermodynamic equilibrium calculations, ThermoCalc Softw. (2013).

[107] Thermo-Calc SSOL5 - SGTE Solution database, version 5.0, ThermoCalc Softw. (2013).

[108] D.A. Porter, K.E. Easterling, Phase Transformations in Metals and Alloys, 2nd ed., Chapman & Hall, London, UK, 1992.

[109] G. Gottstein, L.S. Shvindlerman, Grain Boundary Migration in Metals: Thermodynamics, Kinetics, Applications, Second Edition (Materials Science & Technology), CRC Press, 2009.

[110] G. Couturier, R. Doherty, C. Maurice, R. Fortunier, 3D finite element simulation of the inhibition of normal grain growth by particles, Acta Mater. 53 (2005) 977–989.

[111] R.D. Doherty, D.A. Hughes, F.J. Humphreys, J.J. Jonas, D.J. Jensen, M.E. Kassner, et al., Current issues in recrystallization: a review, Mater. Sci. Eng. A. 238 (1997) 219–274.

[112] P. Rios, G. Fonseca, Grain boundary pinning by Al 6 Mn precipitates in an Al–1wt% Mn alloy, Scr. Mater. 50 (2004) 71–75.

[113] F.J. Humphreys, M.G. Ardakani, Grain boundary migration and Zener pinning in particle-containing copper crystals, Acta Mater. 44 (1996) 2717–2727.

[114] G. Muralidharan, R.G. Thompson, Effect of second phase precipitation on limiting grain growth in alloy 718, Scr. Mater. 36 (1997) 755–761.

[115] C. Guiderdoni, C. Estournès, a. Peigney, a. Weibel, V. Turq, C. Laurent, The preparation of double-walled carbon nanotube/Cu composites by spark plasma sintering, and their hardness and friction properties, Carbon. 49 (2011) 4535–4543.

[116] H. Dieringa, Properties of magnesium alloys reinforced with nanoparticles and carbon nanotubes: a review, J. Mater. Sci. 46 (2010) 289–306.

[117] C.R. Carpenter, P.H. Shipway, Y. Zhu, The influence of CNT co-deposition on electrodeposit grain size and hardness, Surf. Coatings Technol. 205 (2011) 5059–5063.

[118] S.R. Bakshi, A. Agarwal, An analysis of the factors affecting strengthening in carbon nanotube reinforced aluminum composites, Carbon. 49 (2011) 533–544.

[119] P. Thompson, D. Cox, J. Hastings, Rietveld refinement of Debye-Scherrer synchrotron X-ray data from Al_2O_3, J. Appl. Crystallogr. 20 (1987) 79–83.

[120] Q. Huang, L. Gao, Y. Liu, J. Sun, Sintering and thermal properties of multiwalled carbon nanotube–$BaTiO_3$ composites, J. Mater. Chem. 15 (2005) 1995–2001.

[121] Y. Feng, H.L. Yuan, M. Zhang, Fabrication and properties of silver-matrix composites reinforced by carbon nanotubes, Mater. Charact. 55 (2005) 211–218.

[122] C. V Thompson, R. Carel, Stress and grain growth in thin films, J. Mech. Phys. Solids. 44 (1996) 657–673.

[123] C. Krill, R. Haberkorn, R. Birringer, Specification of microstructure and characterization by scattering techniques, in: H.S. Nalwa (Ed.), Handb. Nanostructured Mater. Nanotechnology. Vol. 2 Spectrosc. Theory, Academic Press, San Diego, USA, 2000: pp. 155–211.

[124] P. Manohar, M. Ferry, T. Chandra, Five decades of the Zener equation, ISIJ Int. 38 (1998) 913–924.

[125] V.T. Pham, H.T. Bui, B.T. Tran, V.T. Nguyen, D.Q. Le, X.T. Than, et al., The effect of sintering temperature on the mechanical properties of a Cu/CNT nanocomposite prepared via a powder metallurgy method, Adv. Nat. Sci. Nanosci. Nanotechnol. 2 (2011) 015006.

[126] Y. Maniwa, R. Fujiwara, H. Kira, H. Tou, H. Kataura, S. Suzuki, et al., Thermal expansion of single-walled carbon nanotube (SWNT) bundles: X-ray diffraction studies, Phys. Rev. B. 64 (2001) 241402.

[127] D. Tománek, Carbon-based nanotechnology on a supercomputer, J. Phys. Condens. Matter. 17 (2005) R413–R459.

[128] Y.-K. Kwon, S. Berber, D. Tománek, Thermal Contraction of Carbon Fullerenes and Nanotubes, Phys. Rev. Lett. 92 (2004) 1–4.

[129] G. Panneerselvam, S. Raju, R. Jose, K. Sivasubramanian, R. Divakar, E. Mohandas, et al., A study on the thermal expansion characteristics of Inconel-82® filler wire by high temperature X-ray diffraction, Mater. Lett. 58 (2003) 216–221.

[130] S. Raju, K. Sivasubramanian, R. Divakar, G. Panneerselvam, A. Banerjee, E. Mohandas, et al., Thermal expansion studies on Inconel-600® by high temperature X-ray diffraction, J. Nucl. Mater. 325 (2004) 18–25.

[131] M. Halvarsson, V. Langer, S. Vuorinen, Determination of the thermal expansion of κ-Al2O3 by high temperature XRD, Surf. Coatings Technol. 76-77 (1995) 358–362.

[132] H. Nassini, M. Moreno, C. Gonzalez Oliver, Thermal expansion behavior of aluminum alloys reinforced with alumina planar random short fibers, J. Mater. Sci. 36 (2001) 2759–2772.

[133] F.C. Nix, D. MacNair, The thermal expansion of pure metals: copper, gold, aluminum, nickel, and iron, Phys. Rev. 10 (1941) 597–605.

[134] E. Benavidez, C. Gonzalez Oliver, Sintering mechanisms in YBa2Cu3O7− x superconducting ceramics, J. Mater. Sci. 40 (2005) 3749–3758.

[135] E. Oliber, C. Cugno, M. Moreno, M. Esquivel, N. Haberkorn, J. Fiscina, et al., Sintering of Porous Silver Compacts at Controlled Heating Rates in Oxygen or Argon, Matéria. 8 (2003) 350–357.

[136] J.B. Nelson, D.P. Riley, An experimental investigation of extrapolation methods in the derivation of accurate unit-cell dimensions of crystals, Proc. Phys. Soc. 57 (1945) 160–177.

[137] Y. Waseda, E. Matsubara, K. Shinoda, X-ray diffraction crystallography: introduction, examples and solved problems, Springer-Verlag, Berlin Heidelberg, 2011.

[138] C. Kittel, Introduction to Solid State Physics, 7th ed., John Wiley & Sons, 1996.

[139] D.R. Lide, ed., CRC Handbook of Chemistry and Physics, 90th ed., CRC Press, 2009.

[140] S. Suarez, F. Soldera, C. González Oliver, D. Acevedo, F. Mücklich, Thermomechanical Behavior of Bulk Ni/MWNT Composites Produced via Powder Metallurgy, Adv. Eng. Mater. 14 (2012) 499–502.

[141] R. Roy, D.K. Agrawal, H.A. McKinstry, Very low thermal expansion coefficient materials, Annu. Rev. Mater. Sci. 19 (1989) 59–81.

[142] N. Ferrer-Anglada, V. Gomis, Z. El-Hachemi, U.D. Weglikovska, M. Kaempgen, S. Roth, Carbon nanotube based composites for electronic applications: CNT-conducting polymers, CNT-Cu, Phys. Status Solidi. 203 (2006) 1082–1087.

[143] S.M. Uddin, T. Mahmud, C. Wolf, C. Glanz, I. Kolaric, M. Hulman, et al., Thermal expansion co-efficient of nanotube-metal composites, Phys. Status Solidi. 246 (2009) 2836–2839.

[144] Y. Tang, H. Cong, R. Zhong, H.-M. Cheng, Thermal expansion of a composite of single-walled carbon nanotubes and nanocrystalline aluminum, Carbon. 42 (2004) 3260–3262.

[145] C.F. Deng, Y.X. Ma, P. Zhang, X.X. Zhang, D.Z. Wang, Thermal expansion behaviors of aluminum composite reinforced with carbon nanotubes, Mater. Lett. 62 (2008) 2301–2303.

[146] V. Datsyuk, I. Firkowska, K. Gharagozloo-Hubmann, M. Lisunova, A.-M. Vogt, A. Boden, et al., Carbon nanotubes based engineering materials for thermal management applications, in: 2011 27th Annu. IEEE Semicond. Therm. Meas. Manag. Symp., Ieee, 2011: pp. 325–332.

[147] S. Arai, M. Endo, N. Kaneko, Ni-deposited multi-walled carbon nanotubes by electrodeposition, Carbon. 42 (2004) 641–644.

[148] S. Arai, T. Saito, M. Endo, Low-internal-stress nickel multiwalled carbon nanotube composite electrodeposited from a sulfamate bath, J. Electrochem. Soc. 154 (2007) 530–533.

[149] C.S. Smith, Introduction to Grains, Phases, and Interfaces — an Interpretation of Microstructure, Trans. AIME. 175 (1948) 15–51.

[150] N. Sun, B. Patterson, J. Suni, H. Weiland, L. Allard, Characterization of particle pinning potential, Acta Mater. 54 (2006) 4091–4099.

[151] J. Pauluhn, Multi-walled carbon nanotubes (Baytubes): approach for derivation of occupational exposure limit., Regul. Toxicol. Pharmacol. 57 (2010) 78–89.

[152] Y. Liu, B.S. Senturk, J. V. Mantese, M. Aindow, S.P. Alpay, Electrical and tribological properties of a Ni–18%Ru alloy for contact applications, J. Mater. Sci. 46 (2011) 6563–6570.

[153] M. Braunovic, V. V Konchits, N.K. Myshkin, Electrical Contacts: Fundamentals, Applications and Technology, CRC Press, Boca Raton, FL, USA, 2007.

[154] Y. Liu, B. Patterson, Grain growth inhibition by porosity, Acta Metall. Mater. 41 (1993) 2651–2656.

[155] X. Chen, J. Peng, X. Li, F. Deng, J. Wang, W. Li, Tribological behavior of carbon nanotubes — reinforced nickel matrix composite coatings, J. Mater. Sci. Lett. 20 (2001) 2057–2060.

[156] T.W. Scharf, A. Neira, J.Y. Hwang, J. Tiley, R. Banerjee, Self-lubricating carbon nanotube reinforced nickel matrix composites, J. Appl. Phys. 106 (2009) 013508.

[157] M. Shafiei, A.T. Alpas, Friction and Wear Mechanisms of Nanocrystalline Nickel in Ambient and Inert Atmospheres, Metall. Mater. Trans. A. 38 (2007) 1621–1631.

[158] S.R. Dong, J.P. Tu, X.B. Zhang, An investigation of the sliding wear behavior of Cu-matrix composite reinforced by carbon nanotubes, Mater. Sci. Eng. A. 313 (2001) 83–87.

[159] N. Mironova-Ulmane, A. Kuzmin, I. Steins, J. Grabis, I. Sildos, M. Pärs, Raman scattering in nanosized nickel oxide NiO, J. Phys. Conf. Ser. 93 (2007) 012039.

[160] K.T. Kim, S. Il Cha, S.H. Hong, Hardness and wear resistance of carbon nanotube reinforced Cu matrix nanocomposites, Mater. Sci. Eng. A. 449-451 (2007) 46–50.

[161] R.K. Singh Raman, A.S. Khanna, R.K. Tiwari, J.B. Gnanamoorthy, Influence of Grain Size on the Oxidation Resistance of 2 1/4 Cr-1Mo steel, Oxid. Met. 37 (1992) 1–12.

[162] F. Stott, G. Wood, The influence of oxides on the friction and wear of alloys, Tribol. Int. 11 (1978) 211–218.

[163] F.H. Stott, The role of oxidation in the wear of alloys, Tribol. Int. 31 (1998) 61–71.

[164] W. Chen, J. Tu, L. Wang, H. Gan, Z. Xu, Tribological application of carbon nanotubes in a metal-based composite coating and composites, Carbon. 41 (2003) 215–222.

[165] Z.N. Farhat, Y. Ding, D.O. Northwood, a. T. Alpas, Effect of grain size on friction and wear of nanocrystalline aluminum, Mater. Sci. Eng. A. 206 (1996) 302–313.

[166] D. Rigney, Some thoughts on sliding wear, Wear. 152 (1992) 187–192.

[167] R. Vilar, R. Colaço, Laser-assisted combinatorial methods for rapid design of wear resistant iron alloys, Surf. Coatings Technol. 203 (2009) 2878–2885.

[168] B. Ni, S.B. Sinnott, Tribological properties of carbon nanotube bundles predicted from atomistic simulations, Surf. Sci. 487 (2001) 87–96.

[169] C. Dekker, Carbon nanotubes as molecular quantum wires, Phys. Today. (1999) 22–28.

[170] C. Xu, B. Wei, R. Ma, J. Liang, X. Ma, Fabrication of aluminum-carbon nanotube composites and their electrical properties, Carbon. 37 (1999) 855–858.

[171] J. Nie, C. Jia, N. Shi, Y. Zhang, Y. Li, X. Jia, Aluminum matrix composites reinforced by molybdenum-coated carbon nanotubes, Int. J. Miner. Metall. Mater. 18 (2011) 695–702.

[172] S.M. Uddin, T. Mahmud, C. Wolf, C. Glanz, I. Kolaric, C. Volkmer, et al., Effect of size and shape of metal particles to improve hardness and electrical properties of carbon nanotube reinforced copper and copper alloy composites, Compos. Sci. Technol. 70 (2010) 2253–2257.

[173] W.M. Daoush, Processing and characterization of CNT/Cu nanocomposites by powder technology, Powder Metall. Met. Ceram. 47 (2009) 531–537.

[174] P.R. Bandaru, Electrical Properties and Applications of Carbon Nanotube Structures, J. Nanosci. Nanotechnol. 7 (2007) 1239–1267.

[175] K. Tsukagoshi, E. Watanabe, I. Yagi, N. Yoneya, Y. Aoyagi, Multiple-layer conduction and scattering property in multi-walled carbon nanotubes, New J. Phys. 6 (2004) 3–3.

[176] J. Ohser, F. Mücklich, Statistical analysis of microstructures in materials science, 1st ed., John Wiley & Sons, Chichester (UK), 2000.

[177] M. Wang, N. Pan, Predictions of effective physical properties of complex multiphase materials, Mater. Sci. Eng. R Reports. 63 (2008) 1–30.

[178] T. Ramanan, Electrical Resistivity of Hot-Pressed Compacts, J. Am. Ceram. Soc. 58 (1975) 476–481.

[179] T. Ebbesen, H. Lezec, H. Hiura, J. Bennett, Electrical conductivity of individual carbon nanotubes, Nature. 382 (1996) 54.

[180] Q. Ngo, D. Petranovic, S. Krishnan, Electron transport through metal-multiwall carbon nanotube interfaces, IEEE Trans. Nanotechnol. 3 (2004) 311–317.

[181] P.J. de Pablo, E. Graugnard, B. Walsh, R.P. Andres, S. Datta, R. Reifenberger, A simple, reliable technique for making electrical contact to multiwalled carbon nanotubes, Appl. Phys. Lett. 74 (1999) 323.

[182] J. Li, L. Wang, T. He, W. Jiang, Transport properties of hot-pressed bulk carbon nanotubes compacted by spark plasma sintering, Carbon. 47 (2009) 1135–1140.

[183] K. Yang, J. He, Z. Su, J.B. Reppert, M.J. Skove, T.M. Tritt, et al., Inter-tube bonding, graphene formation and anisotropic transport properties in spark plasma sintered multi-wall carbon nanotube arrays, Carbon. 48 (2010) 756–762.

[184] C. a. Santini, A. Volodin, C. Van Haesendonck, S. De Gendt, G. Groeseneken, P.M. Vereecken, Carbon nanotube–carbon nanotube contacts as an alternative towards low resistance horizontal interconnects, Carbon. 49 (2011) 4004–4012.

[185] B. Corso, I. Perez, P. Collins, Electrode Characteristics of Individual, MnO_2 Coated Carbon Nanotubes, ECS Trans. 41 (2012) 27–33.

List of Figures

List of Tables

List of symbols

Symbol	Description
$\langle d \rangle_{Area}$	area-weighed mean grain size
A	interfacial area / cross section
a	lattice parameter
a_1, a_2	unit vectors
C	effective elastic modulus
C_h	chiral vector
C_p	specific heat capacity
d	Diameter / diagonal size
D	grain size (Scherrer)
dL/L_0	relative expansion
E	Energy / elastic constant
f	volume fraction (per unit)
f_{AB}	cutting efficiency
$\hbar$	reduced Planck's constant
H_0	single-crystal hardness
I_D	D band intensity
I_G	G band intensity
$I_{G'}$	G' band intensity
k	Zener constant
K	Archard constant
k'	modified Zener constant
k_B	Boltzmann constant
l	inter-wire distance
L	load
L_0	initial length
L_a	coherent length
n	Zener exponent
n, m	chiral indices
P	normal load
P_f	final pressure
P_i	initial pressure

R	electrical resistance
r	grain radius
R^2	coefficient of determination
S	sliding distance
S_v	specific surface area
T	temperature
t	time
T_m	melting temperature
W	wear volume/ wear rate
α	coefficient of thermal expansion
γ	interfacial energy
Γ	full width at half maximum
ΔG	Gibbs free energy
ΔH_f	enthalpy of fusion
θ	diffraction (Bragg) angle
λ	thermal conductivity / wavelength
μ	coefficient of friction
ν	Poisson ratio
ρ	Density / electrical resitivity
σ	electrical conductivity / tensile strength
σ_H	Hertz contact pressure

List of abbreviations

Abbreviation	**Description**
(HR)TEM	(high resolution) transmission electron microscopy
(HT)XRD	(high temperature) X-ray diffraction
(I)PF	(inverse) pole figure
CCVD	catalytic chemical vapour deposition
CI	confidence index
CNT	carbon nanotube

COF	coefficient of friction
CPS	cold pressing plus sintering/ pressureless sintering
CTE	coefficient of thermal expansion
DC	direct current
DLVO	Derjaguin, Landau, Verwey & Overbeek
DMF	N,N−dimethylformamide
EBSD	electron backscattered diffraction
EDS	energy dispersive X−ray spectroscopy
EG	ethylene glycol
fcc	face−centred cubic
FIB	focused ion beam
GB	grain boundary
hcp	hexagonal close-packed
H-P	Hall−Petch
HUP	hot uniaxial pressing
IQ	image quality
M-G	Maxwell-Garnett
MLM	molecular level mixing
MWCNT	multiwall carbon nanotube
NR	Nelson−Riley
rms	root mean square
S.D.	sliding direction
SAED	selected area electron diffraction
SEM	scanning electron microscopy
SPS	spark plasma sintering
SWCNT	singlewall carbon nanotube
TLD	through−the−lens detector
vol.%	volume percentage
wt.%	weight percentage

List of units

Unit	Description
°C	Celsius degree
A	Ampere
Å	Angstrom
bar	bar
eV	electron Volt
g	gram
h	hour
HV	Vickers hardness
J	Joule
K	Kelvin
Kgf	kilogram−force
m	metre
N	Newton
Pa	Pascal
V	Volt
W	Watt
Ω	Ohm